Machine learning based object classification from pulse induction metal detector data

Šimić, Marko

Doctoral thesis / Disertacija

2024

Degree Grantor / Ustanova koja je dodijelila akademski / stručni stupanj: **University of Zagreb, Faculty of Electrical Engineering and Computing / Sveučilište u Zagrebu, Fakultet elektrotehnike i računarstva**

Permanent link / Trajna poveznica: https://urn.nsk.hr/urn:nbn:hr:168:215654

Rights / Prava: In copyright /Zaštićeno autorskim pravom.

Download date / Datum preuzimanja: **2025-02-13**

University of Zagreb

FACULTY OF ELECTRICAL ENGINEERING AND COMPUTING

Marko Šimić

MACHINE LEARNING BASED OBJECT CLASSIFICATION FROM PULSE INDUCTION METAL DETECTOR DATA

DOCTORAL THESIS

Zagreb, 2024.

University of Zagreb

FACULTY OF ELECTRICAL ENGINEERING AND COMPUTING

Marko Šimić

MACHINE LEARNING BASED OBJECT CLASSIFICATION FROM PULSE INDUCTION METAL DETECTOR DATA

DOCTORAL THESIS

Supervisor: Professor Vedran Bilas, PhD

Zagreb, 2024.

Sveučilište u Zagrebu

FAKULTET ELEKTROTEHNIKE I RAČUNARSTVA

Marko Šimić

KLASIFIKACIJA OBJEKATA IZ PODATAKA IMPULSNOG DETEKTORA METALA METODAMA STROJNOG UČENJA

DOKTORSKI RAD

Mentor: Prof. dr. sc. Vedran Bilas

Zagreb, 2024.

About the supervisor

Vedran Bilas is professor of electrical engineering at the Department of Electronic Systems and Information Processing, Faculty of Electrical Engineering and Computing University of Zagreb. He leads the research group Laboratory for Intelligent Sensor Systems. His teaching, research, innovation, and professional work is in the field of electronic systems, networked sensors, and technological entrepreneurship.

He is the dean of the University of Zagreb, Faculty of Electrical Engineering and Computing for the academic years 2022/2023. and 2023/2024.

He was awarded with the "Ivan Filipović Award" for 2021 for significant achievements in the field of scientific and professional work, as well as the award of the Croatian section of the IEEE for outstanding contribution to engineering education in 2011.

He led national and international research and development projects financed with public funds and in cooperation with industry. He is a researcher at the Scientific Centre of Excellence for Data Science and Cooperative Systems. He was a member of the editorial board of the main journals IEEE TIM, IEEE SJ, IEEE IMM and the program committee of the most important conferences (IEEE SAS, IEEE SENSORS, IEEE I2MTC) in his field. He organized and chaired four international meetings in the field of sensors and their applications.

O mentoru

Vedran Bilas je redoviti profesor u trajnom izboru na Zavodu za elektroničke sustave i obradbu informacija Fakulteta elektrotehnike i računarstva Sveučilišta u Zagrebu. Vodi istraživačku grupu Laboratorij za inteligentne senzorske sustave. Njegov nastavni, istraživački, inovacijski i profesionalni rad je u području elektroničkih sustava, umreženih senzora i tehnološkog poduzetništva.

Obnaša dužnost dekana Sveučilišta u Zagrebu Fakulteta elektrotehnike i računarstva za mandatno razdoblje akademske godine 2022./2023. i 2023./2024.

Dobitnik je „Nagrade Ivan Filipović" za 2021. godinu za značajna ostvarenja u području znanstvenog i stručnog rada te nagrade Hrvatske sekcije IEEE za izniman doprinos u inženjerskom obrazovanju 2011. godine.

Vodio je nacionalne i međunarodne istraživačke i razvojne projekte financirane javnim sredstvima i u suradnji s industrijom. Istraživač je Znanstvenog centra izvrsnosti za znanost o podatcima i kooperativne sustave. Bio je član uredništva glavnih časopisa IEEE TIM, IEEE SJ, IEEE IMM i programskog odbora najznačajnijih konferencija (IEEE SAS, IEEE SENSORS, IEEE I2MTC) u svom području. Organizirao je i predsjedao četiri međunarodna skupa u području senzora i njihove primjene.

Acknowledgements

I would like to express my sincere gratitude to all those who have contributed directly or indirectly to the creation of this thesis.

To my thesis committee, Prof. Darko Vasić, Prof. Anthony Peyton, and Doc. Stjepan Begušić, for their constructive comments and valuable help in improving the quality of this thesis.

To my mentor, Prof. Vedran Bilas, whose exceptional organizational skills and professionalism have been a guiding force throughout my PhD journey, pushing me to keep things on track and (more or less) on time.

To my closest collaborator, Dr. Davorin Ambruš, who I had the privilege of working with. He has been a constant source of information and inspiration throughout all phases of my research. His role was much like that of a second mentor. The countless hours of brainstorming with him have shaped not only my academic work but also my overall perspective on research and life.

To my friends and colleagues from the Department of Electronic Systems and Information Processing for the intellectual exchange and stimulating environment that contributed significantly to the success of this thesis.

To my friends outside of work for the much-needed escapes from the pressures of research and for the balance they have brought to my life during this challenging period.

To my family - brothers Mate and Ante, parents Zlatko and Jagoda, grandparents Ljubica and Vinka, and the rest of the family for always being there with support and encouragement. I would like to take this opportunity to express my deepest gratitude to my mom, Jagoda, who has always been a role model for me. Her belief in me, her courage and her approach to life have always been my greatest inspiration and have shaped who I am today.

Finally, to my lovely wife, Antonija, her patience, love, and constant encouragement have been my pillars of strength. With her by my side, every step in life, including this PhD journey, becomes brighter and every challenge easier to face.

Contributions from each one of you are what made this success a reality. This degree is as much yours as it is mine.

Abstract

Despite the great efforts of the United Nations, governments, and humanitarian organizations to clear the world of landmines, they still pose a significant threat to local communities decades after the cessation of conflicts, killing or maiming thousands of victims every year. Dealing with the landmine problem requires a set of activities where humanitarian demining (HD) plays a crucial role.

The thesis begins with a brief discussion regarding the historical context that has led to the global landmine crisis. This is followed by a detailed description of procedures used in HD, focusing on the technological aspect. The inability of metal detectors (MDs) to discriminate between harmless metallic clutter and dangerous landmines remains a major technological limitation in HD. Next, a review of existing efforts to evolve from the traditional concept of metallic object detection to metallic object identification is given. The research presented in this thesis aims to build upon these efforts, ultimately leading to safer, cheaper, and faster HD.

The conducted research is separated into three parts. The first part discusses a novel approach for measuring the time-domain magnetic polarizability tensor (MPT) using a pulse induction MD and electromagnetic tracking system. An accuracy evaluation was done using frequency-domain MPT simulations. For comparison, the novel methodology based on the discrete spectrum of relaxation frequencies for the transformation of MPTs from frequency- to time domain is established. The second part introduces a method based on machine learning for rapid metallic object depth estimation from line-scan electromagnetic induction data. The third and last part presents a novel machine learning method for the classification of small metallic objects of practical interest in HD.

Keywords: humanitarian demining, metal detector, magnetic polarizability tensor, discrete spectrum of relaxation frequencies, electromagnetic induction, convolutional neural network.

Sažetak

Klasifikacija objekata iz podataka impulsnog detektora metala metodama strojnog učenja

Protupješačke mine ubijaju ili osakaćuju tisuće žrtava svake godine. Jednom postavljene, mogu predstavljati opasnost desetljećima lokalnom stanovništvu i neinformiranim prolaznicima. To čini velika područja zemlje neupotrebljivima, sprječavajući ljude da koriste minirano zemljište za poljoprivredu, društvene i gospodarske aktivnosti ili stanovanje. Rješavanje ovog problema zahtijeva niz aktivnosti u kojima humanitarno razminiranje igra ključnu ulogu. Humanitarno razminiranje ima cilj potpuno ukloniti eksplozivne naprave s minski zagađenih područja i učiniti ih sigurnima za civilnu uporabu. Ovaj doktorski rad bavi se glavnim tehnološkim izazovima u humanitarnom razminiranju i istražuje napredne metode za poboljšanje njegove učinkovitosti i sigurnosti.

Kontekst, motivacija i hipoteze istraživanja

Još od svoje prve uporabe u Drugom svjetskom ratu do danas, ručni detektor metala čiji se rad temelji na principu elektromagnetske indukcije (engl. *electromagnetic induction*, EMI) je primarni alat koji se koristi u humanitarnom razminiranju. Detektori metala moraju imati vrlo veliku osjetljivost kako bi se ostvarila potrebna razina pouzdanosti detekcije suvremenih mina s vrlo malom količinom metala. Velika osjetljivost se plaća cijenom niske specifičnosti jer konvencionalni detektori metala ne mogu razlikovati metalne dijelove mine od metalnog otpada (npr. metalni čepovi, šrapneli, novčići i sl.). U praksi se pirotehničar može susresti s više od 99% lažnih alarma. Svaki alarm je potrebno pažljivo provjeriti (npr. koristeći šiljasti štap od nehrđajućeg čelika), što značajno usporava postupak razminiranja. Većina nesreća tijekom razminiranja se događa za vrijeme iskopavanja (kada je meta već otkrivena) kao posljedica umora i pada koncentracije pirotehničara opterećenog iskopavanjem prekomjerne količine metalnog otpada.

Kada bi pirotehničar imao informaciju (npr. u obliku vjerojatnosti) o tome je li predmet koji se iskopava nagazna mina ili metalni otpad, to bi omogućilo nekoliko značajnih prednosti u odnosu na postojeću tehnologiju. Prvo, time bi se ubrzao postupak razminiranja jer bi se bezopasni predmeti mogli znatno brže iskopati. Nadalje, ubrzanje postupka razminiranja uštedjelo bi veliki dio vremena, čime bi cijeli postupak bio jeftiniji. Konačno, pirotehničar bi posvetio više pažnje u situacijama kad su predmeti procijenjeni kao potencijalno opasni, čime

bi se smanjila mogućnost nesreća.

Ovaj doktorski rad se temelji na dvije hipoteze. Prva hipoteza jest da je dipolni model dobra aproksimacija mina s minimalnom količinom metala i tipičnog metalnog otpada na koji pirotehničari nailaze za vrijeme razminiranja. Dodatno, koristeći dipolni model, metalni objekt je moguće jedinstveno parametrizirati elementima tenzora magnetske polarizabilnosti (engl. *magnetic polarizability tensor*, MPT). Druga hipoteza jest da se parametri dipolnog modela mogu estimirati iz odziva impulsnog detektora metala snimljenih na različitim lokacijama senzora u odnosu na metalni predmet. Očekuje se da je točnost estimiranih parametara dovoljno dobra za klasifikaciju objekata.

Znanstveni doprinosi

Cilj ovog istraživanja je dati nove uvide u praktične mogućnosti EMI sustava koji se primjenjuju u humanitarnom razminiranju. U nastavku je popis izvornih znanstvenih doprinosa:

1: Metoda mjerenja tenzora magnetske polarizabilnosti korištenjem impulsnog detektora metala.

2: Metoda vrednovanja zna čajki izvedenih iz tenzora magnetske polarizabilnosti u vremenskoj domeni s primjenom na klasifikaciju metalnih objekata.

3: Metoda za klasifikaciju metalnih objekata u humanitarnom razminiranju zasnovana na strojnom učenju.

Struktura doktorskog rada

Doktorski rad sadrži šest poglavlja. Prvo i drugo poglavlje rada daju uvid u širu perspektivu problema protupješačkih mina i aktualne trendove u razvoju tehnologije koja se koristi u humanitarnom razminiranju. Cilj prva dva poglavlja je motivirati čitatelja i dati mu uvod u rezultate istraživanja razrađene u nastavku rada.

Drugo poglavlje je strukturno podijeljeno u tri dijela. U prvom dijelu se navode povijesni razlozi za korištenje protupješačkih mina kao oružja u raznim sukobima, što na kraju dovodi do globalna krize. Također, opisuje se razvoj različitih inicijativa koje su nastale s ciljem (humanitarnog) protuminskog djelovanja. U drugom dijelu dan je kratak uvid u postupak humanitarnog razminiranja i njegova glavna ograničenja s naglaskom na tehnološki aspekt. Kraj drugog poglavlja opisuje postojeće pristupe za klasifikaciju skrivenih metalnih objekata iz EMI podataka i identificira područja za moguća poboljšanja.

Prvi dio trećeg poglavlja daje detaljan uvid u izvod dipolnog modela i teoretsku pozadinu koja opravdava njegovu upotrebu za opisivanje poremećaja vremenski promjenjivog magnetskog polja u prisutnosti malih metalnih objekata. Korištenjem dipolnog modela definira se analitički izraz koji uspostavlja vezu između induciranih napona na detektoru metala i parametara modela (lokacija mete i MPT) u frekvencijskoj i vremenskoj domeni. Svojstvene vrijed-

nosti MPT-a su povezane s intrinzičnim značajkama mete i u radu se koriste za konstrukciju primjera za učenje klasifikacijskih modela. U drugom dijelu trećeg poglavlja se opisuje sustav za mjerenje dipolnih parametara u vremenskoj domeni. Estimacija parametara zasniva se na upotrebi nelinearne metode najmanjih kvadrata (engl. *nonlinear least squares*, NLS) uz *trust-region-reflective* algoritam. Točnost estimiranih svojstvenih vrijednosti MPT-a se ocjenjuje korištenjem simulacija izračunatih u frekvencijskoj domeni. Kako bi se omogućila usporedba mjerenja u vremenskoj domeni sa simulacijama u frekvencijskoj domeni, predložena je nova metoda za transformaciju svojstvenih vrijednosti MPT-a iz frekvencijske u vremensku domenu.

U četvrtom poglavlju dan je kratak pregled postojećih metoda za određivanje dubine metalnog objekta iz EMI odziva senzora ističući njihova glavna ograničenja. Nakon toga je predložena metoda za procjenu dubine metalnog objekta iz EMI podataka linijskog odziva temeljena na upotrebi jednodimenzionalne konvolucijske neuronske mreže (engl. *one-dimensional convolutional neural network*, 1D-CNN). Za ocjenu rezultata, točnost estimacije dubine predloženim postupkom je uspoređena s estimacijama dobivenim korištenjem NLS postupka.

U petom poglavlju se opisuje daljnji razvoj sustava predstavljenog u trećem poglavlju. Konkretno, predlaže se klasifikacijski algoritam temeljen na upotrebi CNN-a za identifikaciju malih metalnih objekata, kao što su mine s minimumom metala. Na kraju petog poglavlja se analiziraju performanse predloženog modela u usporedbi s pet često korištenih pristupa strojnog učenja za klasifikaciju skrivenih metalnih predmeta.

U devetom poglavlju sažeti su ključni rezultati istraživanja i doprinosi, analizirani su nedostatci te predloženi budući smjerovi za razvoj.

Zaključci

Dostupna literatura sugerira da MPT sadrži potrebnu količinu informacija potrebnih za razlikovanje malih metalnih objekata. Međutim, provedena istraživanja ukazuju na nekoliko poteškoća vezanih za estimaciju MPT parametara iz mjerenja. Snažno izražene korelacije između MPT-a i lokacije (tj. dubine) objekta mogu rezultirati velikim rasponom nesigurnosti estimiranih MPT parametara. Nadalje, na estimaciju parametara veliki utjecaj imaju nesigurnosti u podacima senzora, osobito podaci položaja senzorske glave detektora metala za vrijeme mjerenja. Iz tih je razloga teško povezati MPT parametre dobivene simulacijama i one estimirane iz mjerenja. Posljedično, moderni EMI sustavi s mogućnošću klasifikacije metalnih objekata obično se oslanjaju na baze podataka MPT parametara estimiranih iz mjerenja. Dodatno, mjerne nesigurnosti su specifične za sustav s kojim su mjerenja napravljena. Stoga se baze podataka moraju kreirati za svaki sustav pojedinačno, što je dugotrajan proces i predstavlja jedno od glavnih ograničenja za korištenje takvih sustava u praksi.

Doprinos 1. U trećem poglavlju se opisuje novi pristup za estimaciju parametara dipola korištenjem impulsnog detektora metala s kružnom odašiljačkom zavojnicom i magnetskog sus-

tava za praćenje položaja i orijentacije senzorske glave za vrijeme mjerenja. Sustav za praćenje omogućuje prikupljanje velikog broja mjerenja (podaci položaja senzorske glave sinkronizirani s EMI odzivom detektora) u relativno kratkom vremenu iz kojih se NLS postupkom estimiraju parametri dipolnog modela. Ovakav sustav se pokazao prikladan za pouzdanu procjenu parametara koristeći standardnu trajektoriju skeniranja metalnih predmeta koja se koristi u razminiranju. U radu je po prvi put pokazano da se dipolni parametri objekata proizvoljnog oblika mogu estimirati iz mjerenja. Za razliku od postojećih sustava, koji obično uključuju složene laboratorijske postave i rade u frekvencijskoj domeni, razvijeni sustav radi u vremenskoj domeni i lako je prenosiv. Kao takav je prikladan za rad na vanjskom terenu.

Procjena točnosti estimiranih svojstvenih vrijednosti MPT-a napravljena je korištenjem simulacija koje su dostupne u frekvencijskoj domeni. Kako bi se omogućila usporedba mjerenja i simulacija, razvijena je nova metodologija za transformaciju svojstvenih vrijednosti iz frekvencijske u vremensku domenu koja se temelji na upotrebi diskretnog spektra relaksacijskih frekvencija (engl. *discrete spectrum of relaxation frequencies*, DSRF). Predložena metoda nudi nekoliko prednosti u odnosu na standardne tehnike obrade signala temeljene na primjeni inverzne Fourierove transformacije za transformaciju signala iz frekvencijske u vremensku domenu. Predstavljanje svojstvenih vrijednosti u DSRF domeni omogućuje jednostavnu tabličnu transformaciju. Nadalje, korekcija amplituda svojstvenih vrijednosti zbog konačne širine impulsa signala pobude detektora metala zahtijeva samo operaciju množenja. Konačno, svojstvene vrijednosti u vremenskoj domeni mogu se izračunati u proizvoljnim vremenskim trenutcima što je bitno za uspostavljanje odnosa između simulacija i mjerenja.

Doprinos 2. Na dubinama većim od 10 cm (u uvjetima slabijeg odnosa signal-šum), snažno izražene korelacije između MPT parametara i dubine objekta dolaze do izražaja. Posljedično, NLS postupak ima veću vjerojatnost pronalaženja suboptimalnog rješenja. U četvrtom poglavlju se opisuje nova metoda temeljena na strojnom učenju za procjenu dubine iz EMI podataka linijskog odziva detektora. Predloženi pristup iskorištava činjenicu da obrasci matrice osjetljivosti linijskog odziva ovise samo o geometriji zavojnice i lokaciji objekta bez obzira na njegovu orijentaciju, oblik i materijal. Pokazano je da 1D-CNN model može učinkovito ekstrahirati prostorne značajke sadržane u matricama osjetljivosti. Predloženi pristup nudi nekoliko prednosti u odnosu na postojeće metode. Procjena dubine može se dobiti u relativno kratkom vremenu, tipično unutar 10 sekundi. Druga prednost proizlazi iz činjenice da se model trenira isključivo na simulacijama što omogućuje konstrukciju proizvoljno velikog skupa podataka potrebnih za učenje CNN modela.

Procjena performansi napravljena je u odnosu na NLS metodu. Dok na manjim dubinama oba algoritma rade dobro, CNN ostvaruje značajno poboljšanje na dubinama većim od 10 cm. Predložena metoda može se koristiti za ocjenu valjanosti estimiranih dipolnih parametara (tj. MPT-a) dobivenih NLS pristupom, posebno na većim dubinama. Ako se dubine estimirane NLS

postupkom i CNN modelom podudaraju, to ukazuje na veću vjerojatnost da procjena dubine točno odražava pravu dubinu objekta. Posljedično, ovo povećava vjerojatnost da estimirani MPT predstavlja stvarnu metu.

Doprinos 3. Metoda zasnovana na upotrebi 1D-CNN modela za klasifikacije malih metalnih objekata od praktičnog interesa u humanitarnom razminiranju opisana je u petom poglavlju. Po prvi put je pokazano da se modeli strojnog učenja trenirani isključivo na simulacijama mogu koristiti za identifikaciju mina s minimumom metala (PMA-1 i PMA-2) iz mjerenja u vremenskoj domeni. Klasifikacija objekata oslanja se na vremenski ovisne informacije sadržane u svojstvenim vrijednostima MPT-a, kao i relativne omjere između svojstvenih vrijednosti. CNN koristi konvolucijske slojeve za učinkovitu ekstrakciju vremenskih ovisnosti sadržanih unutar vektora značajki. Za razliku od tradicionalnih modela strojnog učenja, CNN se bolje skalira s povećanjem skupa podataka za učenje. Predložena metoda klasifikacije ostvaruje odlične performanse generalizacije na velikom skupu mjerenja opasnih i bezopasnih meta nadmašujući pet tradicionalnih modela strojnog učenja koji su se dosad pokazali uspješni u sličnim klasifikacijskim problemima.

Ključne riječi: humanitarno razminiranje, detektor metala, tenzor magnetske polarizabilnosti, nelinearna metoda najmanjih kvadrata, konvolucijska neuronska mreža, diskretni spektar relaksacijskih frekvencija, elektromagnetska indukcija.

Contents

Chapter 1

Introduction

Anti-personnel (AP) landmines remain a significant threat worldwide, killing or maiming thousands of victims every year. They can lie dormant for decades under, on, or near the ground until a victim triggers their detonation mechanism [1]. This renders large areas of land unusable, preventing people from using contaminated land for agriculture, social and economic activity, or housing [1]. Addressing the problem posed by landmines requires a set of activities where humanitarian demining (HD) plays a crucial role. HD aims to free contaminated areas of explosive hazards and make them safe for civilian use. This thesis addresses the main technological challenges in HD and explores advanced methods to improve its effectiveness and safety.

A fundamental technology employed in HD is electromagnetic induction (EMI) sensing. The main limitation of existing EMI sensing methods is their reliance on metallic object detection, which makes landmine removal a dangerous, slow, and expensive process. This thesis seeks to improve existing methods by evolving from the concept of metallic object detection to metallic object identification. More specifically, the thesis discusses the novel classification strategies based on analytical modelling of EMI phenomena and machine learning for identification of small metallic objects, such as those found in low-metallic content (LMC) landmines.

The upcoming section presents the context and motivation behind the research. Next, the research's main hypotheses, objectives, and major contributions are detailed. The last part of this chapter outlines the thesis structure, providing a short description of the remaining chapters.

1.1 Background and motivation of the research

From its first use in World War II to the present, the EMI-based handheld metal detector (MD) has been an essential tool in HD [2]. Originally, landmines were constructed with metallic casings, making them easily detected by MD. However, during the second half of the 20th century, metallic casing was replaced by plastic, resulting in landmines with a minimal amount of metal (e.g., the firing pin and detonator shell). Modern MDs feature high sensitivity to

extremely low quantities of metal to detect these newer designs, also known as LMC landmines. This comes with a price of low specificity as MDs also become increasingly sensitive to metallic clutter present in the environment (e.g., shrapnel, coin, bullet casing). In a typical demining operation, a deminer may encounter more than 99% of false alarms from metallic clutter [2]. The deminer must carefully examine the source of each alarm, making landmine clearance a slow process. Overwhelmed by frequent false alarms, deminers may become careless, which can lead to accidents. Data in the database of demining accidents reports that most accidents occur during the excavation phase (i.e., when the target is already detected) [3], often caused by deminer fatigue or a false sense of security.

If the deminer can get information (e.g., in the form of likelihood) on whether the object under inspection is a landmine, it would have several significant advantages over the current technology. First, this would accelerate the demining procedure, as the harmless objects could be excavated quickly. Furthermore, speeding up the demining procedure would save much of the time required for landmine clearance, making the procedure less expensive. Finally, if a detected object was believed to be a mine, the deminer would proceed more cautiously to excavation, reducing the chance of accidents.

In recent decades, progress has been made in understanding the challenges that need to be overcome to develop discrimination-enabled MDs suitable for the needs of HD. These challenges are discussed in Chapter II. Recent advances in the field have mainly targeted theoretical aspects related to understanding the perturbation of the magnetic field of EMI sensors in the presence of metallic objects, with little progress regarding practical application. Therefore, this thesis focuses on the latter, with the ultimate goal to close the gap between theoretical knowledge and practical implementation.

1.2   Hypotheses, research objectives and contributions

This thesis aims to improve algorithmic approaches for the classification of small metallic objects (e.g., LMC landmines) buried at shallow depths as required per humanitarian mine action (HMA) standards. The research is established on the following hypotheses:

H1: Low-metallic content landmines could be represented by point magnetic dipoles, whose magnetic moment is induced by the sensor's primary magnetic field at dipole location. Using the induced dipole model, an object can be uniquely parameterized by the elements of its corresponding magnetic polarizability tensor (i.e., directional magnetic polarizabilities) and the dipole location.

H2: Robust discriminative features could be estimated from pulse induction metal detector data and sensor positional data obtained during a manual scan over a buried object. It is expected that the accuracy of feature estimation may be sufficient for object

classification purposes.

Given the above hypothesis, the general research objective is to provide new insights into the practical abilities of EMI-based systems employed in HD. Below is a list of the main scientific contributions:

C1: Method for measurement of the magnetic polarizability tensor using pulse induction metal detector.

C2: Method for evaluation of features derived from the time-domain magnetic polarizability tensor for metallic object classification.

C3: Machine learning-based method for classification of metallic objects in humanitarian demining.

1.3 Structure of the thesis

This thesis consists of six chapters. The first two chapters of the thesis provide insight into a broader perspective of the AP landmine problem and current trends regarding the development of the technology employed in HD. These chapters are aimed to motivate the reader and give a gentle introduction to the research findings elaborated upon in the rest of the thesis.

Chapter 2 is structurally divided into three parts. The first part describes the historical reasons behind using AP landmines as a weapon in various conflicts, which eventually led to a global landmine crisis. It also describes the development of different initiatives which have evolved to address the landmine problem. The second part provides a brief insight into the HD procedure and its main limitations, focusing on the technological aspect. Finally, the third part gives a comprehensive overview of the existing approaches to discrimination of hidden metallic objects and identifies areas for improvement.

Chapter 3 gives a detailed insight into induced dipole model derivation and a theoretical background that justifies its use to describe the perturbation of a time-varying magnetic field in the presence of metallic objects. This is followed by a description of an inversion-based algorithm developed to estimate magnetic polarizability tensor (MPT) parameters in the time-domain (TD). The performance of the proposed approach is evaluated in reference to simulations calculated in the frequency-domain (FD). Finally, a novel methodology for FD-TD transformation based on a discrete spectrum of relaxation frequencies (DSRF) is established to enable the comparison between FD simulations and TD measurements.

Chapter 4 gives a brief overview of existing approaches for the estimation of metallic object depth from EMI data, highlighting their main limitations. This is followed by a description of a method based on machine learning (ML) for rapid estimation of metallic object depth from line-scan EMI data. To contextualize the results, the performance of the proposed approach is compared with the depth estimates obtained using the nonlinear least squares (NLS) inversion

method.

Chapter 5 builds upon developments in Chapter III. Specifically, it describes the development of a simulation-based ML model for the identification of small metallic objects, such as LMC landmines, based on MPT parameters. This is followed by a thorough analysis of the model's performance compared with five commonly employed machine learning (ML) approaches for classifying hidden metallic objects.

Chapter 6 provides an overview of research findings, highlights the benefits of introduced methods, and suggests future research directions.

Chapter 2

Identification of landmines in humanitarian demining

2.1 Magnitude of the antipersonnel landmine problem

2.1.1 Weapon of a mass destruction in slow motion

The origins of AP landmines can be traced back to the 19th century, with their use in conflicts such as the Crimean War or the American Civil War [4]. During the First World War, AP landmines were primarily used to protect the more valuable antitank landmines by preventing enemy troops from easily removing and redeploying them. Their widespread use escalated during the Second World War and has continued in numerous conflicts. Several factors have led to the excess of AP landmines across the globe. Their low cost and ease of transport have made them a preferred weapon among groups like guerrillas, terrorists, and insurgents [5]. These devices are strategically employed to block critical resources and slow enemy advances, not necessarily designed to kill but to injure victims in order to force the enemy troops to activate additional support.

In the 1990s, the landmine crisis became evident in several alarming statistics. Between 85 and 110 million active landmines were scattered across more than 60 countries worldwide, with another 100 million stockpiled and ready for use [6]. In 1994, the United Nations (UN) estimated a global landmine-disabled population of approximately 250,000 [7]. One striking example of the landmine crisis was in Afghanistan, where between 20 and 25 landmine victims were reported daily [8]. Annually, this amounted to approximately 8,000 victims, resulting in a rehabilitation cost of $20 million [8]. The three countries with the highest landmine casualties were Afghanistan, Angola, and Cambodia, which accounted for 85% of the world's landmine victims. [8]. Europe also faced a rapidly growing problem, with more than three million landmines deployed during the fighting in the former Yugoslavia [8]. Given the rate of

mine clearance at that time, it was estimated that it would have taken approximately 1,100 years to eliminate landmines from the world, assuming no additional ones were laid.

Even from a military perspective, the effectiveness of landmines in achieving strategic objectives is questionable. A 1990s study endorsed by high-ranking military officials from various countries examined 26 conflicts since 1940 and found no case in which landmines had significantly influenced the outcome [9]. Yet, they continue to pose harm decades after they are placed, mostly to civilians unfamiliar with the terrain. Due to these reasons, AP landmines have acquired the label of "weapons of mass destruction in slow motion" [5]. This highlighted the urgent need for comprehensive strategies in mine clearance and international cooperation to remove the remnants of these hidden killers.

2.1.2 Worlds response to the landmine crisis

In the second half of the 20th century, various initiatives were taken to address the landmine problem. In the 1970s, the US Department of Defense transitioned to self-destructing and self-deactivating (or non-persistent) landmines [10]. The purpose of this transition was twofold: to prevent enemy use of US landmines against US forces and to reduce the risk to civilians. A growing number of international organizations, including the International Committee of the Red Cross (ICRC), have been actively working for a ban on the use of AP landmines. The ICRC's initiatives in the 1970s, driven by the direct experience of its field surgeons, contributed significantly to the emergence of the UN Convention on Certain Conventional Weapons, which was concluded in Geneva in 1980 and entered into force in 1983, imposing restrictions on the use of AP landmines [9].

Parallel to these developments, in the early 1990s, there was a growing consensus among non-governmental organizations on the need for a coordinated approach to banning AP landmines. As an expression of this consensus, Handicap International, Human Rights Watch, Medico International, Mines Advisory Group, Physicians for Human Rights, and the Vietnam Veterans of America Foundation joined forces in October 1992 and founded the International Campaign to Ban Landmines (ICBL) [11]. The ICBL made a significant contribution to the Convention in 1997 on the Prohibition of AP Landmines, better known as the Ottawa Treaty or the Mine Ban Treaty, signed by 122 countries (typically referred to as State Parties) [11]. This treaty represents a remarkable accomplishment, as it marks the first time nations have collectively agreed under international humanitarian law to prohibit entirely a weapon already in widespread use.

Ottawa Treaty establishes a comprehensive legal framework that requires State Parties to stop the use, production, stockpiling, and transfer of AP landmines while also mandating the clearance of mined territories within ten years following their treaty ratification. Other significant initiatives for HMA have emerged from the Ottawa Treaty, such as the UN Mine Action
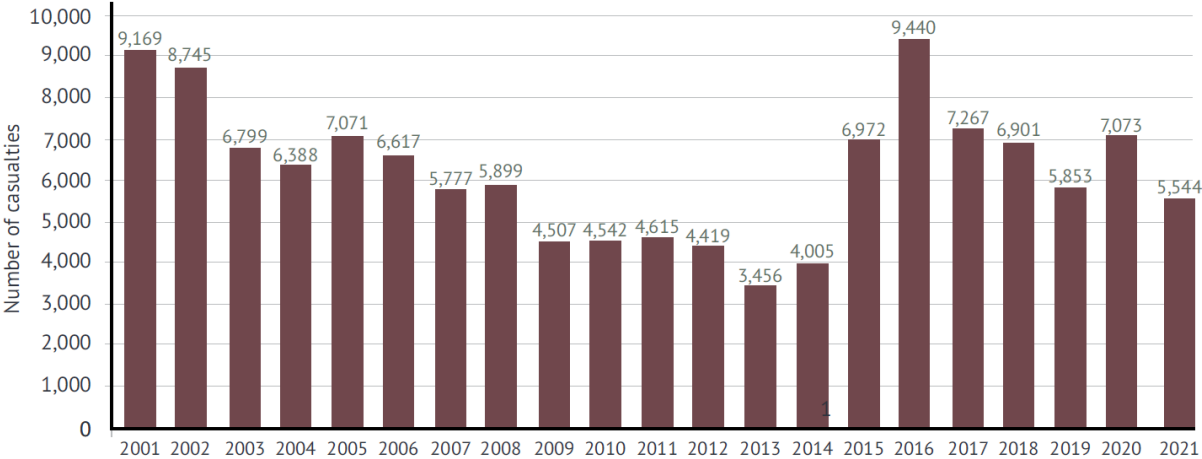
Figure 2.1: Annual landmine (and explosive remnants of war) casualties (2001–2021) [13].

Service (UNMAS) and the Geneva International Centre for Humanitarian Demining (GICHD). UNMAS and GICHD, in collaboration with representatives from the mine action sector, developed International Mine Action Standards (IMAS). IMAS provide comprehensive guidelines and standards for five key aspects (often called five "pillars") of HMA: mine risk education, survey and demining, stockpile reduction, victim assistance and advocacy. These pillars encompass the full spectrum of activities required to protect civilians from the effects of mines [12].

Over twenty-five years after entering into force, the Ottawa Treaty has demonstrated undeniable success. There are 164 state parties bound by and working towards implementing the treaty's obligations, encompassing over 80% of the nations worldwide. Most of the 33 countries that are not yet parties, nonetheless abiding by its key provisions. More than 3,300 km^2 has been demined globally, with over 5 million landmines neutralized. In addition, 55 million landmines in State Paries stockpiles have been destroyed.

However, despite these encouraging facts, the problem is far from solved, which is evident from the increased number of casualties in recent years, Fig. 2.1. At least 5,544 people were killed or injured by landmines and explosive remnants of war globally in 2021. This represents a significant decrease from the 7,073 casualties recorded in 2020 but remains high compared to 2013 when the fewest reported casualties occurred. The notable rise in annual casualties since then is primarily due to intensive armed conflicts involving the use of improvised mines (acting as AP landmines). As of October 2022, a total of 67 states and other areas were either known or suspected to be contaminated with AP landmines, Fig. 2.2. Furthermore, since the Ottawa Treaty came into force in 1999, only 30 States Parties have reported clearing all AP landmines from their territory. One of the biggest limiting factors in that context is technology employed in demining, which has seen little progress since the Second World War. Recent advancements focus mainly on multimodality sensing and data fusion, with the most successful being MDs combined with ground penetrating radar.
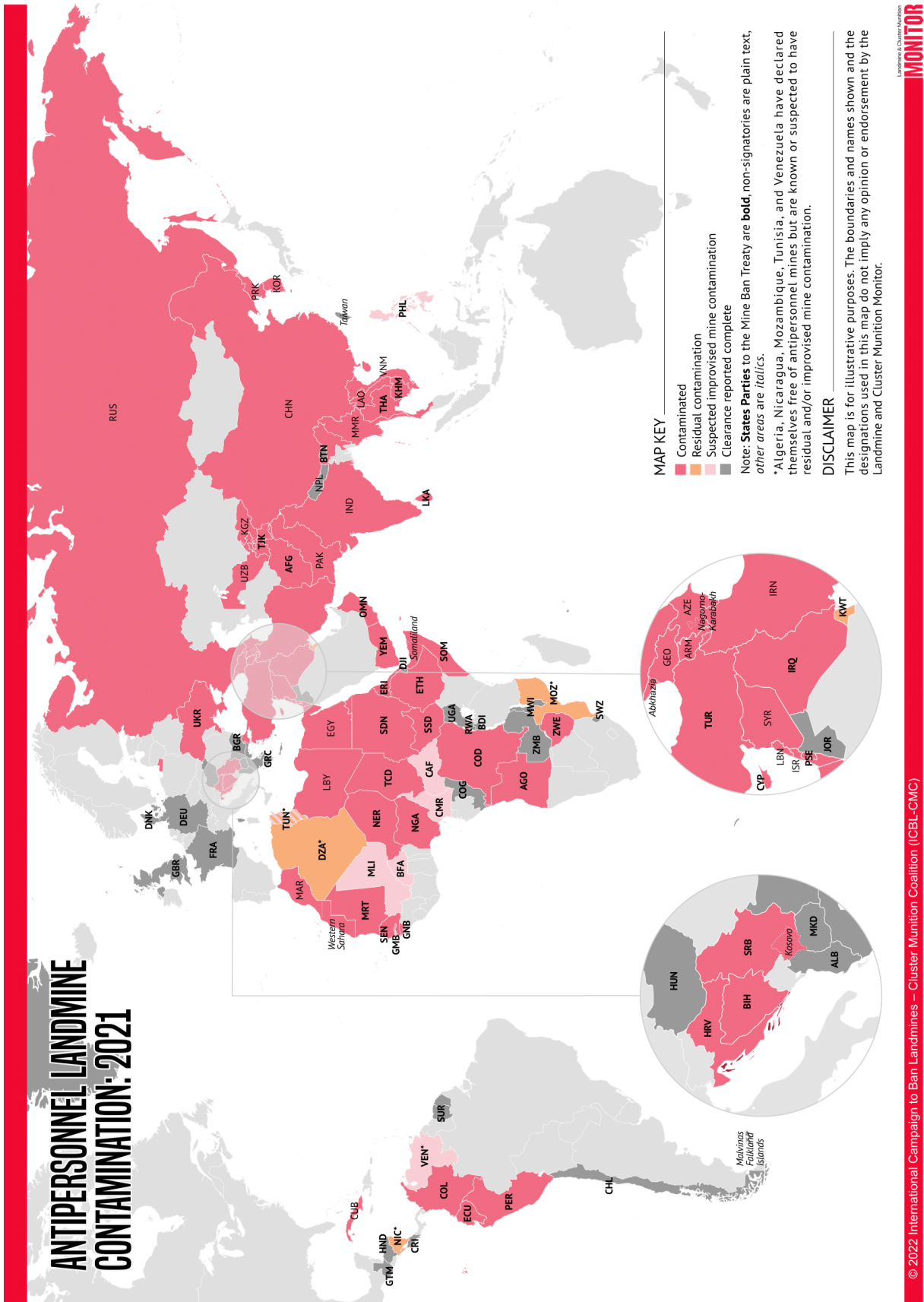
Figure 2.2: Antipersonnel landmine contamination [13].

2.1.3   Antipersonnel landmines

Landmines can be categorized into two types: antitank and AP landmines [14]. Antitank land-mines are designed to counteract enemy vehicles such as tanks or armored personnel carriers, while AP landmines are intended to be detonated by a human. AP landmines can be further divided into fragmentation and blast landmines [15].

Fragmentation landmines disperse lethal fragments over a large area, often causing death up to 25 meters and injuries up to 200 meters [16]. These landmines are relatively easy to detect by MDs due to their substantial ferrous metal content. However, they often incorporate tripwires as a remote triggering mechanism, complicating their detection and neutralization.

Blast landmines are pressure-activated and usually buried just below the ground surface. Al-though, over time, factors like soil erosion and sediment deposits can make them more deeply concealed. They are typically cylindrical, with diameters ranging from 50 to 100 mm and heights of 30 to 80 mm [16]. Activation weights vary between 20 to 100 N, meaning even a small child's weight can trigger them [16]. Their detonation can cause severe foot and leg injuries, often leading to amputations due to secondary infections [16]. Early designs featured a substantial amount of metal in the firing mechanism and used large quantities of explosives, typically TNT ranging from 100 to 300 grams [17]. However, demand for mass production of smaller, cheaper, and harder to detect landmines led to decreased metal and explosive content. These compact, plastic-encased mines, often called LMC landmines, pose a significant chal-lenge in HD. Depending on the region, specific types of LMC landmines are more prevalent. For instance, in Croatian minefields, the Yugoslavian PMA-2 landmine is commonly found, Fig. 2.3. Its only metallic parts, including a thin detonator cap casing and two small aluminium alloy gaskets, make this mine extremely hard to detect using conventional MDs. Typically, the PMA-2 is deployed so that only the star-shaped plunger is visible above the ground. Alterna-
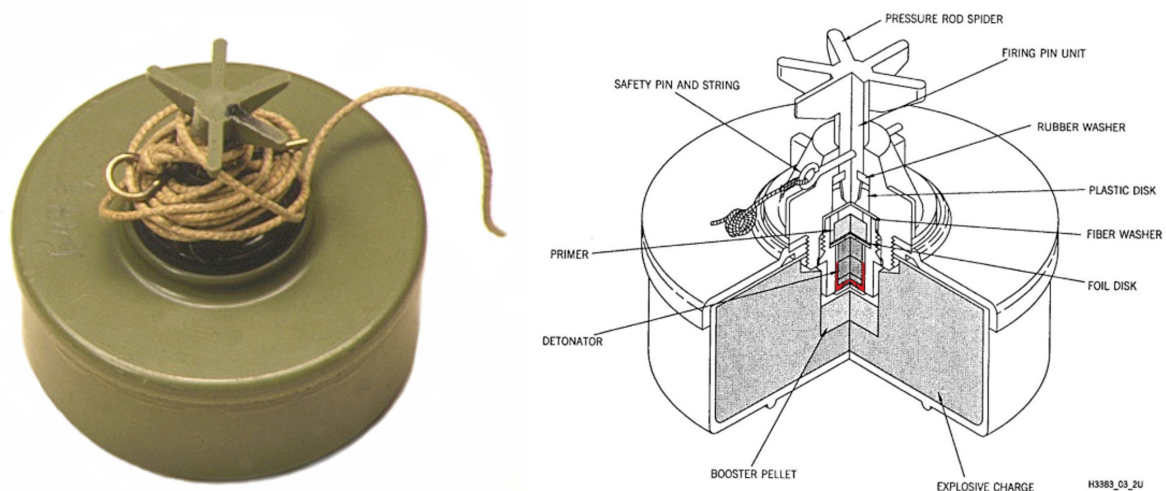

Figure 2.3: PMA-2 - Yugoslavian blast antipersonnel mine [17].

tively, this mine can be emplaced in other ways (e.g., upside down or diagonal to the ground surface) to complicate visual detection and neutralization. Other examples of LMC landmines include a Yugoslavian PMA-3, a Belgian M409, an Italian TS-50, Type-72A Chinese, etc. [18].

2.2 Humanitarian demining and limitations of the conventional metal detection methods

While mine clearance has been part of military procedures for over a century, HD emerged in the late 1980s, initiated by civilian organisations in Afghanistan and Cambodia [19]. The term "humanitarian demining" refers to demining operations under three key criteria [12]: first, the objective is the complete removal of all explosive remnants of war (ERW), ensuring the land is safe for civilian use; second, loses among deminers or civilians who will use the land later are not acceptable, and the highest level of safety standards must be maintained; and third, the only beneficiaries must be civilians, and under no circumstances can HD be used for military purpose. On the contrary, military demining operations typically involve clearing only a pathway through the minefield to facilitate movement. In these operations, casualties are often considered necessary to achieve a military or tactical advantage. Therefore, such "cleaned" land is unsafe for civilians.

Initially, HD was performed by non-governmental organisations funded by charities. This was followed by UN supported programs, predominantly staffed by seconded military personnel. Before long, commercial demining companies emerged, offering cost-efficient clearance options to funding bodies. These developments resulted in considerable variations in demining speeds and methods, leading to concerns about the quality and safety of operations. In July 1996, during an international technical meeting in Denmark, several working groups initially proposed the concept of international standards for humanitarian mine clearance programs. By the late 1996, the concept from Denmark was further developed by a UN-led working groups into the International Standards for Humanitarian Mine Clearance Operations, issued by UN-MAS in March 1997. These standards were later expanded and reissued as IMAS in 2001. Since its establishment, the IMAS framework has been globally acknowledged as the most important set of standards and guidelines in HMA. Using IMAS's guidelines, every nation must establish its own National Mine Action Standards (NMAS). Per these standards, every organisation participating in any aspect of HMA must establish its own standard operating procedures (SOPs).
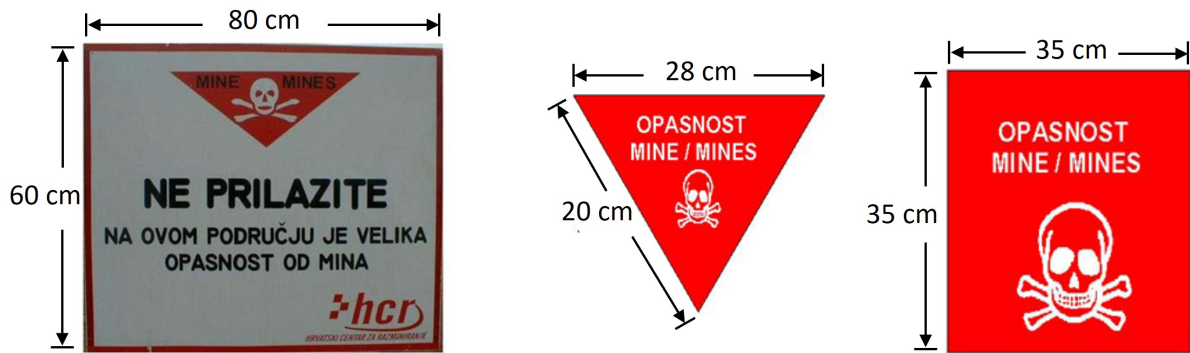
Figure 2.4: Markings of mine suspected area in Croatia [22].

2.2.1 Standard operating procedures

As mentioned, there is no globally accepted way of performing operating procedures in HD, so each country has created its own regulatory and legal structure. While some countries apply IMAS guidelines with minimal adaptation, others, like Croatia, have established a comprehensive legal framework covering different technical aspects of HD [20]. In Croatia, HD activities are supervised by the Croatian Mine Action Centre (CROMAC) [17]. These activities include conducting surveys in the mine-suspected area (MSA), planning and developing demining projects, accreditation of legal entities for demining operations, and conducting quality assurance /quality control of demining operations [17]. In general, operating procedures in HD can be divided into three stages: pre-clearance operations or survey, mine clearance or demining, and post-clearance operations or quality control. The following briefly describes each stage, focusing on HD in Croatia.

Survey

A survey of a MSA is performed in two stages, specifically, general and technical surveys [20]. During the general survey, CROMAC continuously collects data on MSA and maintains its marking by placing mine danger signs, Fig. 2.4. The collection of information is gathered through interviews with relevant personnel familiar with the overall condition of the MSA, as well as by observing the terrain and analyzing documents on previously conducted surveys or demining operations [21]. Based on all available data, the documentation on MSA is updated and community is informed about the current state.

The areas for technical survey represent those defined during a general survey for which there is no original data on mine contamination, as well as other direct evidence of landmines or ERW. However, they cannot be excluded from the MSA due to other indicators that suggest mine contamination, such as fortification facilities built as part of the operational deployment of combat units or evidence of mine contamination in the border areas [21]. CROMAC conducts a technical survey independently or with authorized legal entities (demining organizations) using

(a) Demining in progress.

(b) Safety access roads.

Figure 2.5: Area marking during demining in Croatia.

methods similar to those used during demining [21]. If a technical survey reveals mine or ERW contamination and their indicators (e.g., mine containers, trip wires, holes in the ground), then CROMAC must determine the boundaries of the contaminated area and create a conceptual demining plan. If this is not the case, the area will be excluded from the MSA.

Mine clearance

Before the demining operations start, the authorized legal entity must adequately mark the terrain. This involves placing warning signs to inform that demining is in progress and access is prohibited, marking safety access roads, areas for vehicles and equipment, and areas for testing MD's operation, Fig. 2.5. In Croatia, demining can be carried out by the following methods [22]:

- Manual mine detection as an independent method.
- A surface preparation machine followed by manual mine detection.
- A Surface preparation machine followed by manual mine detection or mine detection dogs.
- A mine detection dogs followed by manual mine detection.

Mine detection dogs can be particularly effective when low concentrations of mines or ERW are anticipated, as they can cover large areas much faster than manual deminers. Therefore, they are considered most useful during technical surveys or in combination with demining machines. On the other hand, in highly contaminated areas, they are less reliable as numerous concentrations of explosive material can make it difficult for the dogs to isolate and identify individual mines. In Croatia, a demining procedure usually starts with a surface preparation machine when the terrain allows. This approach may significantly reduce the risk to deminers by removing vegetation and undergrowth, cutting tripwires, and exposing or deactivating hidden threats. However, a practical issue with machines stems from the fact that they can sometimes bury

mines deeper into the ground, making them even more challenging to find. Due to limitations associated with demining machines and dogs, manual detection with MD and prodders remains the primal method employed in HD, with the highest confidence to meet required clearance standards. As long as they are in accordance with NMAS and safety is not compromised, some details of the manual clearance procedure may vary depending on the contractor performing the task. The standard search techniques used by deminers include search lanes, spot task search, and lateral search [23]. Spot task search is conducted over a small area, such as when investigating an indication from a mine detection dog, while lateral search is efficient for searching the verges of roads or waterways. Most manual demining is conducted in search lanes; therefore, its procedure is described below. The procedure is based on the global SOPs detailed in [23].

Before the manual clearance starts, there must always be absolute confidence in the MD's ability to locate the most challenging target (i.e., threat object) expected in the field at the required depth. This must be checked (on designated MD calibration and test areas) at the start of each working session and every time after the deminer returns from a break. A suspected hazardous area (SHA) is typically divided into 1 m wide lanes. Including a safety overlap of 10 cm on each side of the lane, the cleared area is 1.2 m wide. An overlap eliminates the possibility of any missed gaps between adjacent lanes. If demining machines are not used in advance, progress through the lane (covered by vegetation) requires manual preparation of the SHA in front of the deminer. A deminer always stands behind the base-stick, which separates SHA from the safe area, Fig. 2.6. The manual preparation process involves a visual inspection to identify tripwires, surface landmines, and other suspicious objects. Next, a tripwire feeler, typically made of light-gauge wire, is used to detect both loose and tight wires. Finally, hand tools such as small pruning tools or garden shears are used to cut any vegetation.

Once the area is prepared, the deminer proceeds with the scanning using MD. Scanning is done by horizontal, sideways motion of the MD search head following the typical pattern, Fig. 2.6b, and keeping the search head close to the ground without applying pressure. After each line sweep, the search head is moved forward (or backwards), not more than 1/3 of its search head length, to secure a safe overlap. Sometimes, a guide-stick marked along its length and placed perpendicular to the base-stick is used to guide the search-head pattern during the scan, Fig. 2.6a.

When the MD alarm occurs, sweeps are not interrupted, but rather, the deminer remembers the approximate position and continues with the search, Fig. 2.6b. This is important as there might be more than one alarm (e.g., indicating the presence of more targets within the search area) or some known pattern (e.g., the linear pattern may indicate the presence of tripwires). Upon scan, the deminer should first take a closer look and remove any visible metal parts by hand. If the alarm still persists, it is important to accurately pinpoint its location closest to the base stick and place a marker there. The deminer proceeds with the excavation using the

blast-resistant mechanical prodders, Fig. 2.6c. The excavation starts by prodding the ground surface 20 cm (or at least half the diameter of the largest anticipated target at the task) away from the marker, Fig. 2.6c. To reduce the risk of accidentally activating the mine by vertical pressure, prodding is done from a lateral direction, keeping the prodder at an angle of around 30° to the ground surface. The deminer must expose any obstruction with extreme caution by lightly tapping it from a side. In HD, quality assurance protocols typically mandate the complete removal of all metallic objects, as it is better to spend more time digging out harmless metallic objects (i.e., clutter) than risk an injury [17]. When the object is removed, the deminer moves the base-stick forward, typically 1 m, and repeats the whole procedure.

Quality control

Quality control involves reviewing quality assurance documentation made during demining, as well as manual detection on sampled areas after the clearance is completed. In Croatia, quality

(b) Scan pattern.

(a) Search in standing pose.
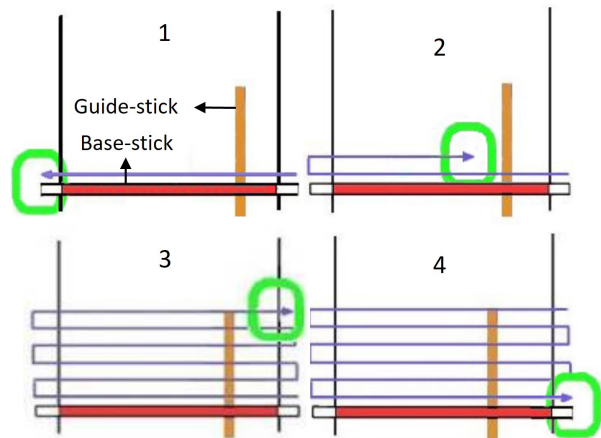
(c) Excavation procedure.

Figure 2.6: Demining in progress [23].

control is carried out on at least 1% of the cleared areas [20]. If mines, ERW, or unexcavated metallic objects are found during the quality control, the demining of the area must be repeated. Otherwise, the area will be excluded from the MSA.

2.2.2 Metal detectors in humanitarian demining

As mentioned, the handheld MD is the main tool employed for mine clearance in HD, Fig. 2.7. This section explains its operating principles, testing procedure, standard designs, and main limitations.

Operating principle

MD is also called an EMI sensor as it operates on the principle of EMI. The terms MD and EMI sensor are used interchangeably throughout this thesis. A time-varying excitation current running through the transmitter coil generates a time-varying (primary) magnetic field that reacts with metallic objects, Fig. 2.8. Induced eddy currents and magnetization in the object generate a secondary field that is detected by the receiver coil. The detected secondary field represents the response of an object, which depends on its shape, size, and material properties (i.e., electric conductivity and magnetic permeability). As a result, in the presence of a metallic object, an MD produces an alarm (i.e., audio, visual, or vibration). In HD, an audible alarm is the pri-
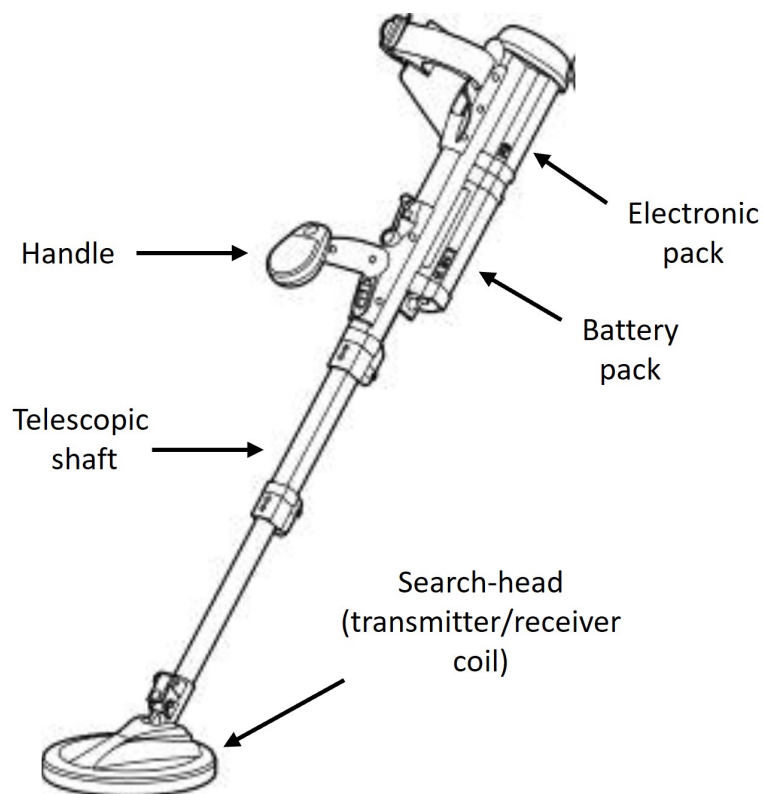
Handle

Electronic pack

Battery pack

Telescopic shaft

Search-head (transmitter/receiver coil)

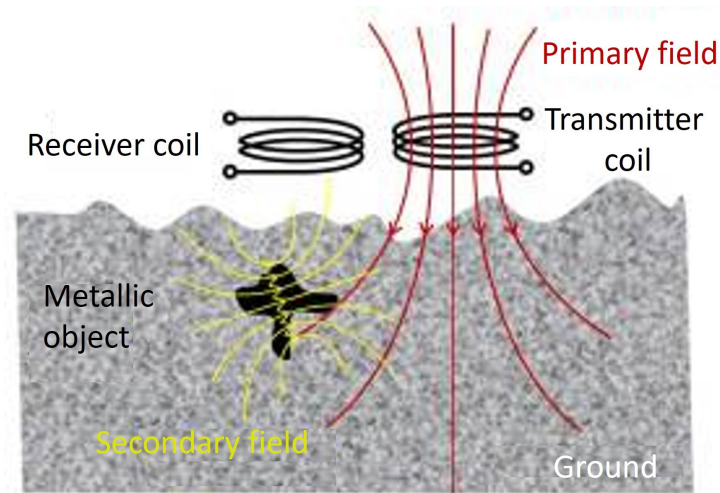**Figure 2.7:** Handheld metal detector (MineLab F3 model) [24].

Figure 2.8: Operating principle of metal detection [25].

mary interface between a deminer and a detector. While a vibrating handle may sometimes be used as an auxiliary interface, displays (especially large ones) are generally avoided to prevent distraction during the search [17].

CWA standard

Until the early 2000s, handheld MDs used in HD were primarily made by military standards [19]. These standards include requirements of military needs, many of which were of no relevance in HD. For example, one such requirement states that MD should have a probability of detecting mines greater than 92%, which is unacceptable in HD [19]. On the other hand, some critical aspects, such as ground compensation (further elaborated later in this section), were not addressed at all [17]. A need for an MD standard that is relevant in HD was recognized in the HD community during the 1990s. As a response, the European Center for Standardization (CEN) set up a Working Group CEN BT/WG 126 to make recommendations and initiate standardization within HMA. With the support from the European Commission's Joint Research Centre, the International Test and Evaluation Program, UNMAS, and GICHD, the CEN BT/WG 126 launched CEN Workshop 7, "Humanitarian Mine Action - Test and Evaluation-Metal Detectors" (CWO7). In 2003, the efforts of CW07 resulted in the release of the CEN Workshop Agreement (CWA) 14747:2003, which gives principles, guidelines, and testing procedures for the evaluation of MD performance in HD. A brief description of key tests is given below:

- **Measurements in-air:**
  Sensitivity - the detector shall be swept over a range of targets - at least eight balls shall be used, covering the diameter range from 4 mm to 15 mm. The variation of maximum detection height with target size is therefore determined, Fig. 2.9. The experiment should be performed for varied detector sweep speeds from 0.1 m/s to 1 m/s.
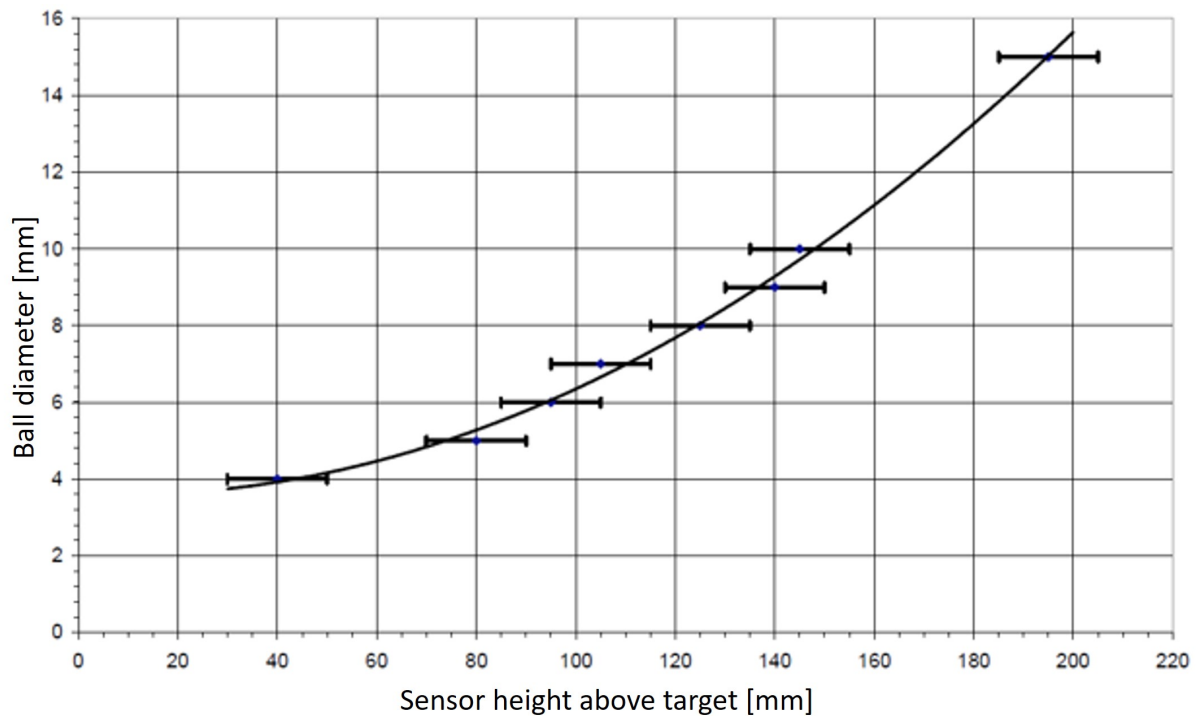
Figure 2.9: Detection capabilities for targets in air [26].

Detection sensitivity for specific targets - such objects may include standard realistic targets of interest, mine simulants, surrogates or real mines. In a given setting, this allows ranking the targets in order of ease of detection for MD in use.

Sensitivity profile (footprint) - the sensitivity variation with location in a plane parallel to the search head. This data can be used to define the overlap needed between consecutive scans to ensure complete coverage at the required sensitivity.

Additional tests include repeatability of sensitivity for five successive detector set-up cycles and variation of sensitivity due to detector drift over three hours.

- **Detection capability for targets buried in soil:**

Minimum detectable target as a function of depth - comparing in-air and in-soil detection curves, characterizes the effect of that particular soil on the detector sensitivity. For MDs affected by the soil, the sensitivity curve is shifted upwards compared to that obtained in the air, Fig. 2.10.

Detection capability for specific targets in soil - the objective of this test is to measure the maximum detection depth of a specific target. In order to measure the effect of the soil on the detection capability for that target, the results may be compared with the measurements in the air.

Fixed-depth detection test - the objective of this test is to determine the detection capability of the MD for buried test targets at fixed depths in a given soil. The detection capability is, therefore, expressed as the target detected or not detected at the test depth.
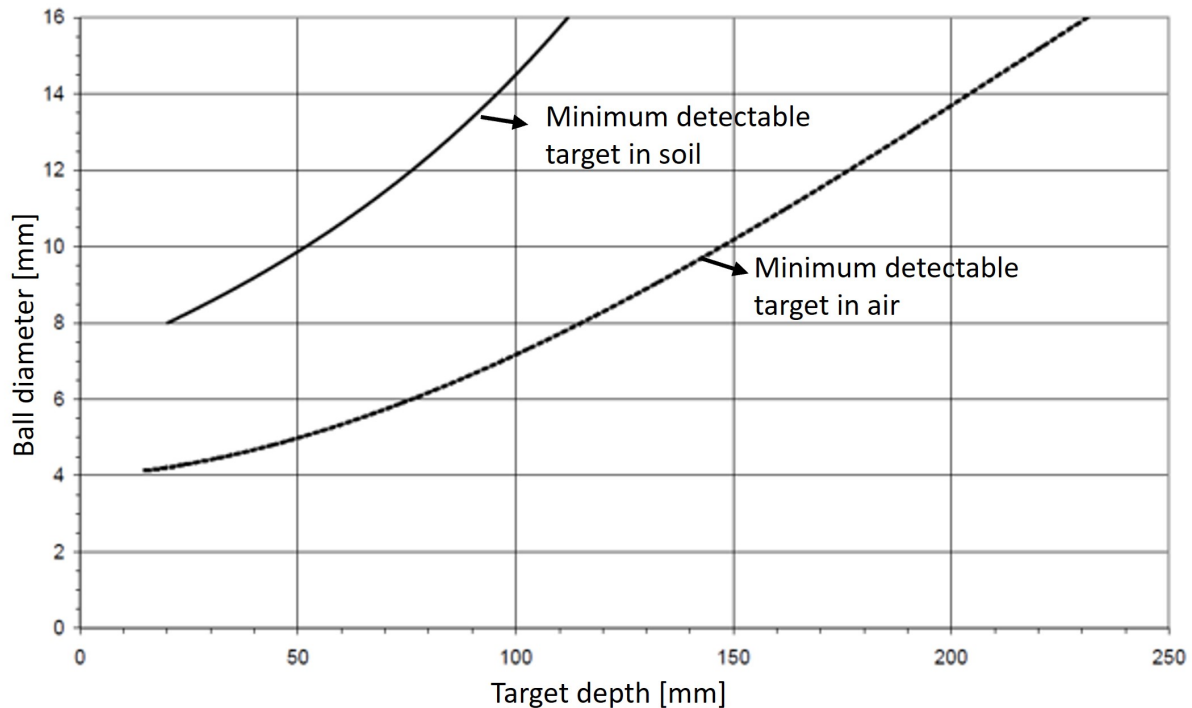
Figure 2.10: Detection capabilities for targets buried in soil [26].

Detection reliability tests - the objective is to evaluate how environmental and human factors affect the results of the previous test. Targets are buried in the soil at specified depths, like in the last test. However, the operator does not know the target's location in this test. So, the goal is to evaluate the detection reliability of MD by adding the environmental and human factors.

- **Operational performance characteristics:**

  Target location accuracy - the objective of this test is to measure the accuracy with which the detector can locate the position of the buried target. This procedure is often called "pinpointing" and is used to compare the performance of different detectors for the same object.

  Resolution of adjacent targets - the objective of this test is to determine the capability of the MD to discriminate between targets buried close to each other. The minimum target separation distance at which the targets can be resolved is measured.

The reader is referred to [26] for more details on test and evaluation procedures. Following the CWA release, it has been extensively used in the upcoming MD test and evaluation trials performed by the International Test and Evaluation Program for Humanitarian Demining (ITEP) members. These trials helped improve CWA standards and gave manufacturers important information on what is expected from their products, allowing them to respond to the needs of HD.

For example, the soil was recognized as the main influencing factor on detector perfor-

mance. In extreme cases, the influence of the soil can be so significant that some MDs may fail to detect landmines at the desired depth, which is life-threatening to deminers.

Frequency-domain versus time-domain

There are two types of MDs based on their excitation waveform: continuous wave and pulse induction.

The continuous excitation waveform consists of a discrete number of sinusoids. In the early stages of MD development, they were often tuned to a single discrete frequency [27]. While these detectors are simpler in design and operation, they exhibit a rather limited performance compared to multi-frequency models, particularly regarding soil compensation and target discrimination [27, 28]. Signal processing of continuous wave MDs is done in the FD, so they are also known as FD MDs [29]. Information about the metallic object is obtained by examining the amplitude and phase of the response at each frequency [27]. Amplitude and phase can be expressed as real (in-phase) and imaginary (quadrature) components of the response, Fig. 2.11a. Some of the established models used in HD are CEIA MIL D1 [30], [31], Schiebel ATMID [17],
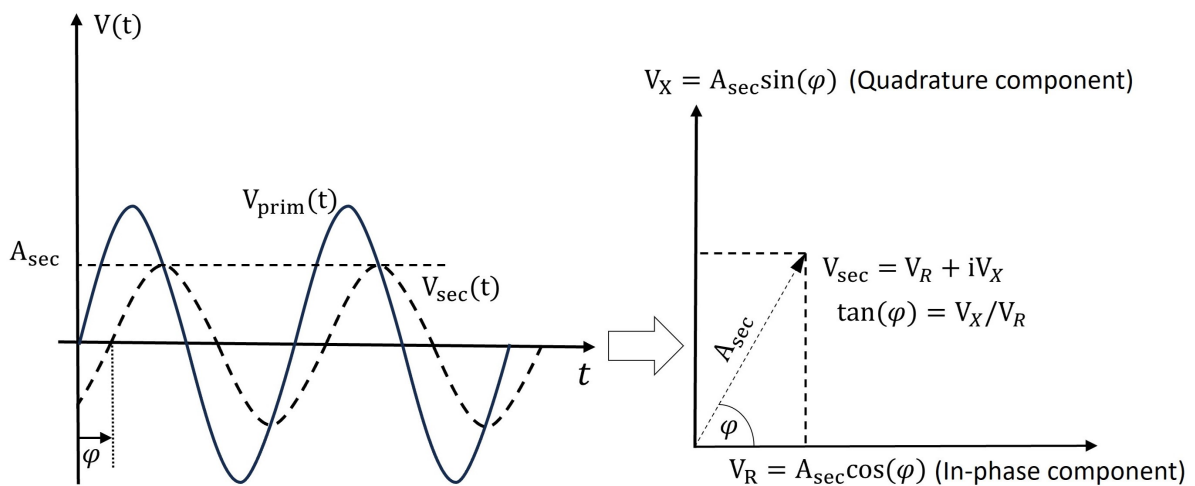
(a) Frequency domain.
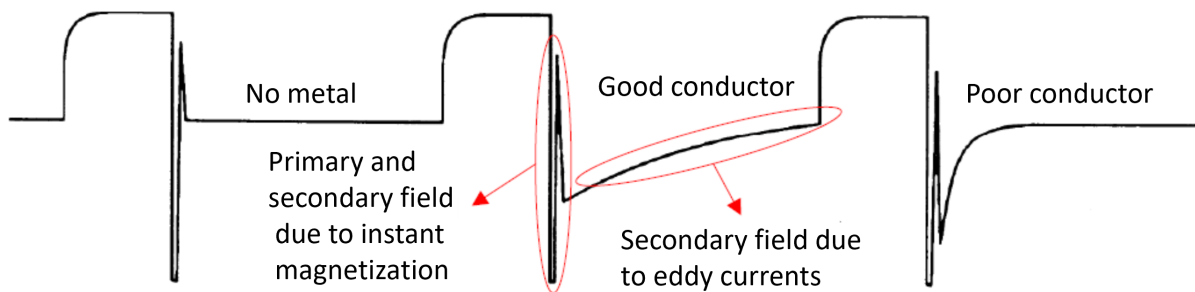
(b) Time domain (Fig. adapted from [17]).

Figure 2.11: Metal detector response waveforms.

and Foerster Minex 2FD [23].

Pulse induction MDs operate with a pulse waveform excitation, typically of the order of 1 kHz. Signal analysis is performed in TD; hence, they are also known as TD MDs. After the excitation switch-off, the response is sampled at different time gates (TGs) during the predefined time window. The typical response waveforms of different types of objects are shown in Fig. 2.11b. Note that the shape of the response obeys exponential decay laws $Ae^{(-\frac{t}{\tau})}$. A decay constant τ in the TD response is an equivalent parameter to a phase shift in the FD response [17]. Some of the TD detector models available on the market are Vallon VMP3 and VMF4 models [32], Minelab F3 [24], and Ebinger 420C [17, 27, 33].

Each type of MD offers some advantages, depending on the specific use case. TD detectors can work with larger powers of the transmitting coil (i.e., greater inspection depths), and the temporal separation of primary and secondary fields allows simpler coil configurations [34]. On the other hand, one of the main challenges in the FD MD designs is to eliminate the inductive coupling of the transmitter and receiver coils since it directly affects the sensor's sensitivity. Soil compensation is also somewhat simpler using TD detectors [17].

The main advantage of FD designs is that they allow wideband operation (less than 100 Hz up to 100 kHz). On the other hand, TD models feature a somewhat limited excitation spectrum, usually 1-10 kHz [17]. Lower frequencies are limited by the finite duration of the time window during which the response is sampled, while higher frequencies are limited by the current switch-off time, Fig. 2.11b. Despite a limited excitation spectrum, TD MD often has more frequencies involved in the response, so the detector picks up more noise. Consequently, FD MDs achieve a much higher signal-to-noise ratio [29].

Adverse soil effects on metal detector performance

The influence of soil on MD performance is not the focus of this thesis; however, ignoring this aspect would not provide a complete picture of the challenges involved in the development of discrimination-enabled MD. Therefore, this section gives brief details related to unfavourable soil effects on MD functionality and standard approaches employed to address the soil problem.

Although the adverse effects of certain soil types on MDs were recognized back in the 1940s, the problem kept a low profile in the demining community until the early 2000s, when it was identified as a major obstacle for MD operation in the field [35, 36]. For example, in case of LMC landmines buried in heavily mineralized soil, the response of soil at depths of interest can be several orders of magnitude greater than that of a landmine [2]. In general, the magnetic susceptibility of soil originating from ferrimagnetic minerals (e.g., magnetite, maghaemite, and titanomagnetite) has a much greater influence on the MD performance than its electrical conductivity [37, 38]. Fortunately, the soil response does not interfere with the target response; in other words, the total response can be represented as the sum of soil and target response [17].

Different approaches to ground (or soil) compensation have been proposed for both FD and TD detectors. Ground compensation refers to the technique of cancelling the soil response from MD measurements.

When it comes to TD detectors, soil compensation is based on different temporal features of the soil and object response. The characteristic decay function A/t has been used by many authors to model the soil response in archaeological prospecting, mineral exploration, and unexploded ordnance (UXO) surveys [39, 40]. The modification of the characteristic decay model (2.1) has been proposed in [39].

$$soil(t) = A \left(\frac{1}{t} - \frac{1}{t + \Delta t} \right) \tag{2.1}$$

In (2.1), Δt is transmitter "on time". Regardless of the model in use, soil compensation is always done by removing the best fit of the model from the response. Besides the model-based approach, soil compensation in TD can also be done using the pulse excitation waveforms of different durations [41].

For FD operation, a straightforward way of implementing soil compensation is based on the assumption that the phase response of the soil is the same within the scanning area around the target [27]. The soil response is measured in the first step when no metallic object is present. Each measurement in the proximity of a metallic object is then rotated so that the soil response is completely in phase and can be easily suppressed. Another approach, which requires multi-frequency designs, is the frequency differencing method [27, 42, 43]. The assumption is that the differential response (i.e., subtraction of detector responses at different frequencies) will remain the same within the scanning area. This requires the ground over the scanning area to be uniform. The soil response can then be removed similarly to the previous approach by subtracting no-object from the object response. Some manufacturers (Minelab Electronics) use search head designs almost exclusively in "*DD*" configuration, which inherently suppresses the static component of the soil response [17]. Others ignore the in-phase component entirely and use only the quadrature component of the response for detection [44]. This relies on the fact that the real component of soil susceptibility is by an order of magnitude or larger than the imaginary component [17, 43].

In general, the existing compensation techniques inevitably lead to some loss of sensitivity and distortion of the object's response, which usually limits their applicability to object detection rather than discrimination.

Limitations of conventional metal detection process

Recent technology advancements mainly targeted improvements in MD detection performance by increasing the efficiency of soil compensation to allow the detection of LMC landmines in
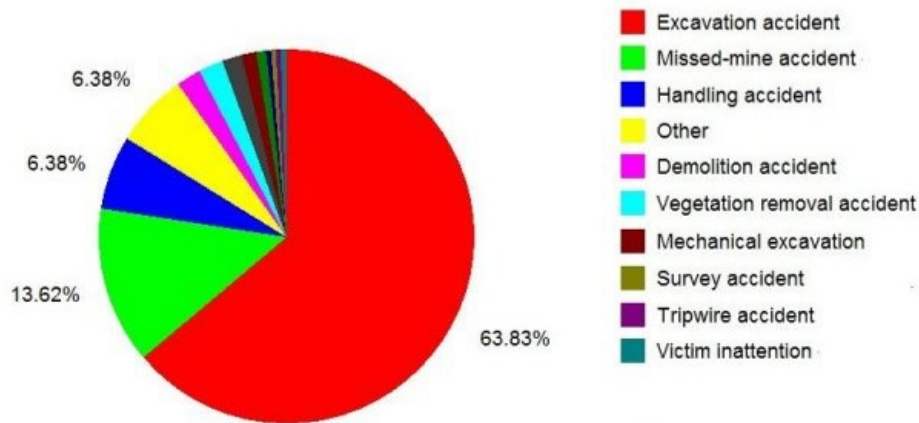
Figure 2.12: Demining accident and incident records (2005-2010) [3].

challenging soil conditions. This is witnessed by the decrease in the number of accidents due to missed mines [3]. However, these improvements do not address the problem of the false alarm rate associated with the detector's inability to discriminate between mine and clutter. It is important to highlight that slow demining speed due to a high false alarm rate is not a major concern in the HD community, as it does not directly affect safety. Nonetheless, the time spent investigating false alarms can lead to deminer fatigue and carelessness, and eventually to accidents. According to data in the database of demining accidents, almost two-thirds of accidents happen during prodding and excavation, which is often a consequence of deminer exhaustion from handling a large number of detections [3], Fig. 2.12. On the other hand, if the deminer thought there was a high likelihood that a detected object was a mine, he/she would be more careful during the excavation phase, which would reduce the number of accidents.

The discussion above brings us to the concept of discrimination-enabled MDs, which has received much attention in the last decade. The shift from metallic object detection to discrimination requires enhanced sensor capabilities enabling the extraction of the object's intrinsic EMI signatures (i.e., features), as well as the integration of machine learning techniques for decision-making (e.g., threat or non-threat). The forthcoming section discusses the necessary advancements (focusing on the latter) to make this shift possible and highlights major limitations of the existing attempts.

2.3 A review of the existing approaches to buried metallic object discrimination

In the previous chapter, a brief overview of HD procedure and its main challenges are discussed, focusing on the technological aspect. Specifically, the inability of MDs to discriminate between harmless metallic clutter and dangerous landmines remains a major technological limitation in HD. The only commercially available handheld MDs with some level of object discrimination are those designed for UXO/clutter problem [45, 46]. The discrimination is based on simple object properties like size or material, assuming that UXOs are relatively large and ferromagnetic objects, as opposed to smaller, non-magnetic clutter. This approach is not applicable in HD since AP landmines and clutter items are often similar in size, and both can be magnetic or non-magnetic. The scaling down of the object size makes the development of discrimination-enabled MD a complex engineering challenge. In general, improvements are required on three different levels: raw data level, feature extraction level, and decision-making level, Fig. 2.13.

At the raw data level, the main challenge is to remove background interferences from EMI data, where the most problematic part is the suppression of soil response. However, this thesis focuses on the feature extraction and decision-making levels, where the assumption is that the EMI data are not corrupted by the soil response. This assumption can be used without the loss of generality, as soil compensation is usually performed in the pre-processing stage.

The following gives a brief overview of the existing feature extraction and classification techniques. In general, the development of the classification algorithm can be seen as a three-stage process: extraction (and selection) of features, model selection, and model evaluation. Therefore, this section follows the same structure.
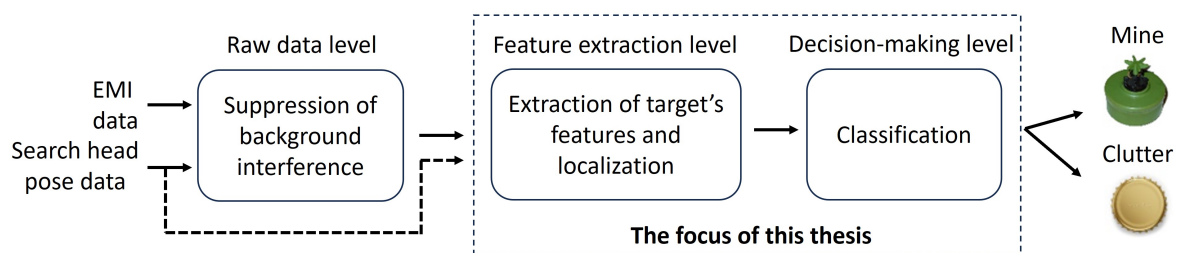

Figure 2.13: Discrimination of buried metallic objects from EMI data.

2.3.1 Extraction of metallic object features from metal detector data

Early approach to feature extraction

Early feature extraction techniques were usually based on a single MD response, typically the maximum response measured during the scan over the object.

When it comes to FD MDs, a simple classification of an object's size may be done by utilizing the phase shift between primary and secondary magnetic fields as a discriminative feature. This approach assumes that the phase shift is a continuous, monotonically decreasing function of the object size [27]. However, the assumption is justified if other object parameters remain the same. Ferromagnetic and non-ferromagnetic objects can also be distinguished by analyzing the phase shift. Specifically, a positive phase indicates that the object is ferromagnetic. Nevertheless, a negative phase does not imply that the object is non-ferromagnetic - due to phase frequency dependence [17]. Multi-frequency MD designs can utilize EMI spectroscopy (EMIS) technology to improve the discrimination possibilities significantly. The main idea is that each object is uniquely characterized by its spectral signatures. Besides EMI spectral shape, some important features include the peak frequency of the quadrature component, phase angle, and zero-crossing frequency of the in-phase component [28]. A widely recognized empirical model used to capture the basic phenomenology of EMI spectral signatures is a four-parameter model (2.2). Although this approach was initially developed for modelling the wideband response of UXOs [47], it has later been used by many authors for feature extraction in landmine/clutter discrimination [48, 49].

$$X(\omega) + jY(\omega) = q\left(s + \frac{(j\omega\tau)^c - 2}{(j\omega\tau)^c + 1}\right) \tag{2.2}$$

In (2.2), the parameter q represents the amplitude, τ is a time constant, s controls the asymptotes at low and high frequencies, while parameter c controls the width of the transition zone [48]. These parameters can be estimated by solving non-linear optimization problem or by using a fast lookup table [49]. Another interesting approach to feature extraction that recently received much attention is to represent the wideband EMI response as the sum of the DSRF [50]. While this approach offers a lot of benefits (elaborated in Chapter III), parameter estimation is not straightforward [50, 51].

In TD, due to the decaying nature of the response, a popular early approach to feature extraction was to represent the response with a single decaying exponential, assuming that the lowest mode dominates the response [29, 52, 53, 54, 55, 56]. A generalization of the aforementioned approach is to use the sum of exponential decays [57]. This is the TD equivalent of the DSRF approach. Different techniques have been used to estimate exponential decay parameters, including Prony's method or computationally more efficient Matrix Pencil method [34, 58, 59].

The most notable empirical model used by many authors to capture the basic phenomenology of object EMI response in TD is the Passion-Oldenburg model [60, 61, 62, 63],

$$u(t) = k(t + \alpha)^{-\beta} e^{-t/\gamma}. \tag{2.3}$$

The parameter k refers to the magnitude of the response, while α is proportional to the duration of the flat early time stage of the time decay curve. The intermediate time stage is modelled by $t^{-\beta}$ and the late time stage is represented by the exponential decay, parametrized by γ [60].

The main drawback of the above methods is the ambiguity of the extracted features, which are not only related to the object's properties but also to search head coil design, as well as the location and orientation of the object relative to the coil. To decouple the object's intrinsic features from sensor-object system geometry, a physics-based model describing the perturbation in the magnetic field caused by the presence of a metallic object is required.

Feature extraction including forward modelling

Various analytical models and parameter estimation procedures, which allow the separation of object intrinsic features from sensor-object system geometry, have been proposed. Forward modelling requires position-referenced MD data, which can be obtained manually using the grid [62, 64] or using a separate positioning system such as cameras with markers [30], a robot with GPS [33], or sophisticated multi-receiver sensor designs [65]. Most of the proposed methods are based on the magnetic dipole approximation, which enables efficient parameter computation suitable for real-time applications. For larger heterogeneous objects (e.g., UXO), the response can be calculated using, for example, a set of elementary dipole sources [66, 67] or a metal shell model [68]. On the other hand, if the metallic object is small enough compared to the size of a receiver coil or is far enough from the coil, the induced dipole model is a well-established approach [34, 69, 70, 71]. A detailed derivation of the induced dipole model is given in Chapter III. Dipole model parameters, object location, and orientation are estimated as part of the nonlinear inverse problem. A comparative study of algorithmic techniques for the dipole inverse problem can be found in [42]. In general, all reported algorithms face difficulties due to the nonlinear nature of the inverse problem, which may become surprisingly difficult and potentially ill-posed due to strong correlations between the dipole model parameters and object location (especially the object's depth [72]). A machine learning-based approach for depth estimation, which significantly simplifies the decoupling of the localization and parameter estimation problems, is discussed in Chapter IV. Furthermore, optimization performance is susceptible to measurement uncertainties, such as sensor noise and positional errors. For the UXO/clutter discrimination problem, a search head tracking accuracy of 2 cm has been suggested [73]. In the case of smaller targets, such as LMC landmines, sub-centimetre accuracy is required [74]. For a long

time, this requirement has been a significant bottleneck in feature extraction methods that rely on position-referenced EMI data, such as the induced dipole model. However, recent advancements related to search head tracking problem are encouraging. Specifically, in [75], authors presented a portable EM tracking system featuring mean absolute tracking accuracy in the order of millimetres. The most recent results of dipole model parameter estimation obtained utilizing the novel EM tracking system are presented in Chapter III.

2.3.2   Approaches to metallic object classification

Classification of buried (or hidden) metallic objects from MD data belongs to the group of supervised classification problems. In a supervised framework, a labeled training dataset (i.e., feature-label pairs) is used to build a ML model that maps new features to expected labels of threat or non-threat objects. Most published research has targeted the UXO/clutter discrimination problem, which has different requirements for classifier performance. In UXO clearance operations, the reduction of false positives is prioritized. On the other hand, when it comes to landmines, a classifier should be designed to minimize the number of false negatives (i.e., threat classified as non-threat) as it represents the most dangerous scenario for the deminer's safety. In both cases, the classifier makes a decision based on features obtained from EMI data. Therefore, most methods initially developed for UXO/clutter discrimination can be easily adapted to landmine/clutter discrimination problems. In the following, a brief overview of the different classification strategies proposed for landmine (or UXO)/clutter discrimination is given.

Library based approach

Sometimes, when clutter is highly variable, it may not be practical to define a clutter class because there is a substantial overlap with target classes. In such cases, classification can be based only on the feature vectors of targets without making any assumption about the data distribution of the clutter [61].

Analysing the spectral signatures of different types of landmines for the measurements in the air, Won *et al.* suggest using a library of known landmine signatures to discriminate between landmines and clutter [28]. In [71], the authors presented a "learn-as-you-go" approach to identify landmines using normalized EMIS. The EMIS spectrum is normalized to be independent of target orientation or depth; therefore, classification is based on EMIS spectral shapes. In the first phase of demining, the operator excavates all detected objects in the minefield, and when a mine is encountered, the library is updated. Similar mines with different spectra are treated differently. If all mine types expected in the field are excavated and a large misfit (2.4) occurs between the object under test and the targets from the library, then the object under test should

be declared clutter [71].

$$\chi = min \left\{ \frac{\sum_{i=1}^{M} \left(|X_i - \hat{X}_i^j| + |Y_i - \hat{Y}_i^j| \right)}{\sum_{i=1}^{M} \left(|\hat{X}_i^j| + |\hat{Y}_i^j| \right)} \right\}, \tag{2.4}$$

In (2.4), χ is the misfit in per cent, X_i and Y_i are the measured normalized in-phase and quadrature responses at ith frequency, $\hat{X}_i^j$ and $\hat{Y}_i^j$ are the normalized in-phase and quadrature response in the library for ith frequency and jth landmine type, M is the number of frequencies, and L is the number of landmine types stored in the library [71].

Pasion *et al.* suggest building a library based on features obtained by fitting the Passion-Oldenburg model (without parameter α as suggested by J.D. McNeill [60]) to dipole model parameters obtained through the inversion process [40]. The library was developed based on hazardous targets expected during a survey. When an unknown target is detected, the inversion problem is solved for the position and orientation that minimizes the least-squares difference between the unknown object and the data predicted by each target [40]. The soil compensation is done by removing the best fit of the A/t term from the response. The algorithm predicts the object by selecting a target from the library with the smallest misfit.

Sower *et al.* employed the E-pulse technique to discriminate between landmines and innocuous metallic clutter [76]. Each target in the library is represented by its corresponding E-pulse, $E(t)$, constructed to annihilate the response of the target,

$$E(t) \circledast R(t) = 0. \tag{2.5}$$

In (2.5), $R(t)$ refers to the target response, and $\circledast$ is the convolution operator.

Statistical classification

Statistical classification is a supervised learning method that uses training data to formulate a decision rule for discrimination, which is then used to classify new unlabeled data. Based on the formulation of the decision rule, two different approaches can be identified: generative and discriminative [61].

Generative classifiers attempt to learn the joint probability $P(\mathbf{x}, y)$ over the input data $\mathbf{x}$ and label y, and then compute the conditional probability distribution $P(y|\mathbf{x})$ based on Bayes rule (2.6) as a predictive model [61, 77].

$$P(y|\mathbf{x}) \propto P(\mathbf{x}|y)P(y). \tag{2.6}$$

The *posterior* probability $P(y)$ quantifies how likely class y is to be observed, and the *likelihood* $P(\mathbf{x}|y)$ is the probability of observing feature vector $\mathbf{x}$ for the given class $P(y)$. Based on the

form of the *likelihood* function, classifiers can also be divided into parametric and nonparametric [61]. In parametric classifiers, the input data (feature vectors) are assumed to obey a certain theoretical distribution (e.g., Gaussian) and the number of model parameters is fixed. In contrast, for nonparametric classifiers, the number of model parameters is not fixed and depends on the number of data in the training set.

Different parametric classifiers based on the likelihood ratio test were reported [54, 55]. In these studies, the discriminative decision was based on different exponential decay rates of targets (i.e., UXO and landmines) and clutter. In [78], two algorithms were analysed, namely, support vector machine (SVM, discussed later in this section) and the gaussian likelihood ratio (GLR) (2.7), in the context of UXO/clutter discrimination problem.

$$(\mathbf{v} - \mathbf{v}_0)^T \Delta^{-1} (\mathbf{v} - \mathbf{v}_0) - (\mathbf{v} - \mathbf{v}_1)^T \Delta^{-1} (\mathbf{v} - \mathbf{v}_1) \underset{H_0}{\overset{H_1}{\gtrless}} \lambda \qquad (2.7)$$

Parameter λ represents the threshold, $\mathbf{v}$ is the feature vector, while $\mathbf{v}_0$ and $\mathbf{v}_1$ are the mean feature vectors under hypotheses H_0 (clutter) and H_1 (UXO), respectively. In the GLR approach, the data was assumed to obey a multivariate Gaussian distribution. Dipole model parameters estimated using gradient descent search were used to build a feature vector $\mathbf{v}$. Authors found that 930 Hz and 2790 Hz were particularly useful for classification.

Sower *et al.* [79] proposed a 6-D "Pole" approach to identify different types of landmines and clutter. The amplitudes and time constants of the exponential decays were extracted from responses by applying the singular expansion method. The means and standard deviations were obtained for each class to provide a basis for target classification. Unknown objects are predicted by calculating the 6-D "Pole" score (2.8) for each class using a super-Gaussian function

$$score(t) = exp\left(-\sum_{i=1}^{6}\left(\frac{Pole_i - Mean_i(t)}{m \cdot Sdev_i(t)}\right)^N\right). \qquad (2.8)$$

The parameter m is the scaling factor that controls the width over which the fit gets a high score, t refers to the target, and N is the power of the super-Gaussian [79].

A representative example of nonparametric classifiers used for buried object discrimination is the probabilistic neural network (PNN) [66, 80]. The PNN models the underlying statistical distribution as superpositions of Gaussian kernel functions centred on each training vector [61]. It consists of four layers: input layer, hidden layer, summation layer and output layer (decision layer). During the training phase, the vectors from the training set are simply copied to the hidden layer. Each neuron in the hidden layer (2.9) models the Gaussian distribution, where the value of the vector represents the mean, and sigma (σ) is the only adjustable parameter. At the prediction stage, the parameter d is typically calculated as the Euclidean distance between the

mean and the unknown input vector

$$hidden\_neuron = exp\left(\frac{-d}{\sigma^2}\right).$$

(2.9)

The number of neurons in the summation layer is equal to the number of classes; each neuron collects the outputs from all the hidden neurons of its corresponding class. The output layer computes the probability that a new vector belongs to each class. Although the algorithm has a fast training process, it has disadvantages such as large data storage requirements and slow execution time.

In [80], PNN is applied to the UXO/clutter discrimination problem. The features were extracted in two steps. In the first step, dipole model parameters were estimated using the inversion procedure. Final features were obtained by fitting the Passion-Oldenburg model (2.3) to the estimated parameters. Specifically, feature vectors were the size feature $\log_{10}k$ and the ratio of the dipole parameters at late and early times. A similar approach using PNN, also for the UXO discrimination problem, was presented in [66].

Discriminative classifiers, instead of learning a joint probability (like generative classifiers), directly define a decision boundary to classify test data. The process of finding a decision boundary is the constraint optimization problem [61]. A representative discriminative classifier used by many authors for buried object identification is SVM [62, 78, 81, 82]. The SVM achieved better classification performance than GLR (2.7) for the UXO/clutter discrimination problem analysed in [78]. The GLR approach is optimal if the assumed underlying distributions are correct. However, assumptions are often not based on prior knowledge but rather on simplicity [78]. On the other hand, SVM does not require prior knowledge about the procedure that generated the data. SVM is based on a theoretical framework of statistical learning theory that allows the design of an optimal classifier [81]. The basic concept is shown in Fig. 2.14. During optimization, the classifier strives to find the hyperplane separating two classes. Therefore, the distance (denoted as the margin) between the support plane and the decision boundary is maximized. Only a few vectors that lie on the support plane, referred to as support vectors, contribute to a prediction (i.e., the model is sparse), which means that a SVM has reasonable memory requirements, unlike PNN [81]. The real strength of a SVM lies in its dual formulation, which enables the classifier to search for a linear separation between classes by mapping the original space to a higher dimension using kernel functions. This allows SVM to generate a nonlinear decision boundary in the original space. The sparsity of the model allows this dimension to be very large [81]. The SVM makes predictions using the following function

$$f(x) = sgn\left(\sum_{i=1}^{L} y_i \alpha_i \langle \phi(\mathbf{v}), \phi(\mathbf{v}_i) \rangle + b\right).$$
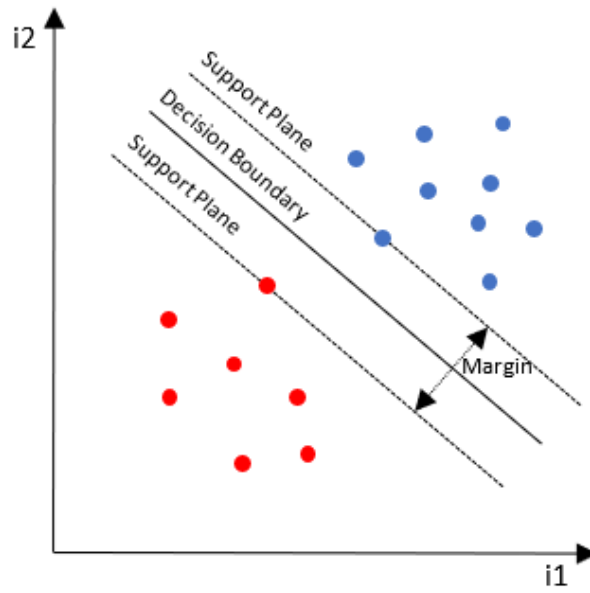
(2.10)

Figure 2.14: SVM formulation for linearly separable 2-D feature space belonging to two classes represented by red and blue circles.

In (2.10), b is the bias term, while support vectors are those $\mathbf{v}_i$ for which $\alpha_i > 0$. The function $\langle \phi(\mathbf{v}), \phi(\mathbf{v}_i) \rangle$ is a nonlinear measure of the similarity between the new input vector $\mathbf{v}$ and the support vector $\mathbf{v}_i$, called the kernel function.

In [82], the authors recently showed that a fully-connected artificial neural network (ANN) can outperform the SVM approach when dealing with landmines/clutter discrimination problem. The algorithms were tested on a large dataset of 1669 sweeps over 14 objects buried in different soil types and depths. A block of 60 measurements was extracted from each sweep when the detector was near the object. The phase spectrum of the soil response is estimated from the measurement in the absence of the object. Each measurement from the block was then rotated so that the soil response is fully in-phase and can be easily suppressed. The proposed ANN contains five layers with a 50/25/20/10/3 configuration. The algorithms (i.e., SVM and ANN) were trained to classify each object into one of three classes: no metal, harmless metal, and threat. Threat objects were LCM landmines PMA-2 and PMA-3. The authors reported a true positive rate of 100% at a FAR of 45%, allowing rejection of up to 55% of false alarms compared to the conventional approach using MD without discrimination abilities.

Fails *et al.* proposed k-nearest neighbors (kNN) for landmine discrimination [48]. A kNN is a nonparametric discriminative classifier in which the decision statistic is determined by comparing the average distance of the test vector to the k nearest clutter vectors and its average distance to the k nearest mine vectors. The only hyperparameter for tuning is the number of neighbours k. For feature extraction, the authors employed the four-parameter model (2.2). The response used as an input to the feature extraction was obtained by subtracting the soil response at the beginning of each grid square (i.e., in the absence of the object) from the response mea-

sured at the centre of the grid near the object. Beside four-parameter model parameters, authors suggest using an additional feature as an input to the kNN classifier, specifically, the energy of the quadrature response.

In a recent study [83], the performance of six discriminative classifiers, namely SVM, decision tree, random forest (RF), logistic regression, multi-layer perceptron, and gradient boost, was analyzed. The objective was to classify metallic objects, such as coins, guns, and knives, based on simulated dipole model parameters in FD. The authors highlighted the advantages of using a broader range of frequencies and larger training datasets. Overall, best performing classifier was gradient boost algorithm.

To conclude, discriminative models usually perform better than generative models when tested on the same dataset. This is not surprising as discriminative models focus directly on the optimization of classification boundary. In contrast, generative models are trained to predict the joint distribution of input vectors (i.e., features) and labels. The generative paradigm introduces unnecessary complexity into model construction since the main goal is to discriminate between different classes rather than generating new instances. Nevertheless, selecting the optimal model is not the prime concern when it comes to practical application. With a sufficiently large training dataset, both generative and discriminative models would perform well. However, generating such datasets is usually time-consuming since most reported classification strategies require data from measurements for model training. Therefore, slow data collection in combination with large datasets needed for training is one of the main limitations of such classification strategies in practice. Section V further elaborates on this topic, where the novel classification strategy, which aims to overcome this limitation, is introduced.

2.3.3 Performance evaluation techniques

The most common visualisation technique used to evaluate the performance of the classifier when dealing with binary classification problem (e.g., target/clutter) is receiver operating characteristic (ROC) (2.15) [48, 61, 82, 84, 85]. The probability of a false alarm (P_{fa}) is calculated by dividing the number of target predictions that are not true targets by the total number of possibilities for a false alarm. The probability of detection (P_d) is calculated by dividing the number of target predictions that are true targets by the number of possibilities for target detection. A set of different thresholds describes the relationship between P_d and P_{fa}. The scores for increasing thresholds are plotted to create a ROC curve. For example, increasing threshold λ in equation (2.7) lowers the chance that the object will be interpreted as a target, resulting in an increased number of missed targets. Another way to generate a ROC curve is to sort the test data outputs from highest to lowest rank and label them according to the rank. The proportion of targets found as a function of clutter is then used to create a ROC curve. Outputs sorted this way are sometimes called "dig list" [86], representing the order proposed by classifier in which
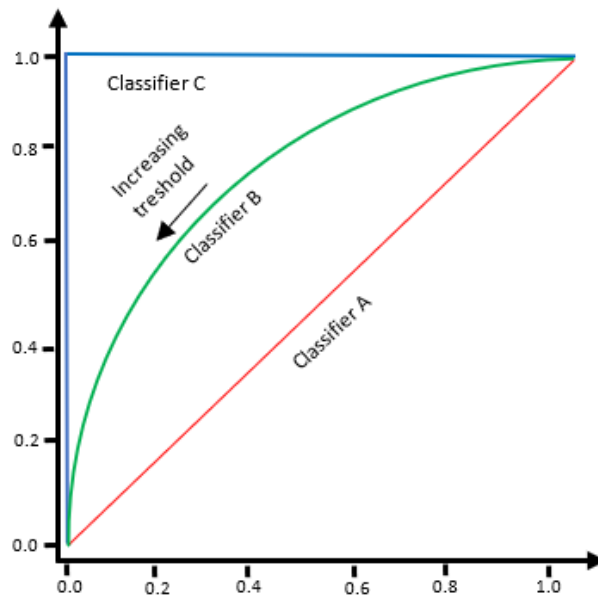
Figure 2.15: ROC curves of classifiers: Classifier A - random guessing; Classifier B - real classifier; Classifier C - ideal classifier.

the objects should be excavated.

Another popular metric derived from the ROC curve by integrating P_d with respect to the P_{fa} is the area under the curve (AUC).

AUC ranges from 0 to 1 and can be described as the probability that the classifier will correctly classify a randomly selected pair of target and clutter [61].

As mentioned, in HD, the most critical constraint imposed on classifiers is keeping the number of false negatives (FNs) close to zero. In this regard, an informative metric to evaluate discrimination performance is the false alarm rate (FAR), which measures the amount of clutter that needs to be dug out to find all the targets [61]. Graphically, it defines a point where (P_d) first reaches 1 (see Fig. 2.15). Another straightforward way to assess discrimination performance is using a confusion matrix [82]. For binary classification problems, the confusion matrix categorizes predictions into four groups: true positives - number of correctly classified targets; true negatives - number of correctly classified clutter items; false positives - number of incorrectly classified clutters; FNs - number of incorrectly classified targets.

2.3.4   Discussion

In general, the feature extraction stage is considered the critical step in the discrimination of metallic objects using EMI sensing. At present, there is no portable EMI-based system that can reliably obtain intrinsic features of metallic objects from measurements. This limitation has several consequences:

- It is not possible to use simulated features for (decision-making) model training; instead, slow dataset collection through measurements is required.

•Features obtained with one MD design are typically not transferable to train models of another MD design.

•Measurement uncertainties can cause significant variation in extracted features, negatively affecting discrimination performance.

Due to these reasons, translating discrimination-enabled MD into practical use has been challenging.

As already mentioned, the response of an EMI sensor does not only depend on object features but also on sensor design and its the relative pose in relation to the object. Therefore, feature extraction requires using an analytical model which gives the relationship of these effects to the response. In this context, the induced dipole model has proven to be effective in terms of capacity (i.e., model parameters provide a good basis for discrimination of metallic objects) and computation efficiency required for real-time application. However, difficulties arise due to the ill-posedness of the inverse procedure used for dipole parameter estimation. Two main factors contribute to the poorly constrained inverse procedure: measurement uncertainties associated with the search head tracking errors and strong correlations between the dipole model parameters and the object's depth.

To deal with the ill-posedness of the inverse problem, Chapter III presents a novel approach to dipole parameter estimation, which takes advantage of a recently developed high-precision EM tracking system used to acquire search head pose information during the scan. Moreover, a novel machine learning-based approach for depth estimation is discussed in Chapter IV, which may significantly facilitate the feature extraction compared to the standard full parameter inversion process. Chapter V discusses the further development of the system presented in Chapter III. This involves the development of a simulation-based machine learning model, as well as a demonstration of its performance when tested on realistic targets (i.e., LMC landmines).

Chapter 3

Inversion-based magnetic polarizability tensor measurement from time domain EMI data

This chapter is based on the following publication:

In the previous chapter, the dipole model approximation was identified as the main approach to feature extraction from EMI data when it comes to small metallic objects. Major technological challenges that need to be addressed to apply this approach in practice are also discussed. This chapter gives a detailed insight into induced dipole model derivation and a theoretical background that justifies its use to describe the perturbation of a time-varying magnetic field in the presence of metallic objects. Next, the chapter describes an inversion-based method developed to estimate dipole parameters in the TD. Finally, as a part of the performance evaluation, a methodology for FD-TD transformation is established to enable the comparison between FD simulations and TD measurements.

3.1 The solution to magnetic vector potential using a quasi-magnetostatic approximation

3.1.1 Magnetic and electric fields in matter

When it comes to EMI sensing, interaction of the materials with the magnetic field is of greater importance than interaction with the electric field. Therefore, this section focuses on the materials' magnetic properties.

When the magnetic field is present in a material, the magnetic dipole moments within the atoms and molecules tend to align with the applied field. The magnetic moments originate from the motion of electrons around the nucleus, the spin of the electrons around their axis, and electron interactions with one another. Depending on the material type, dipole moments will align in the same or opposite direction as the applied field. In both cases, the magnetic field will change. To account for this change, the magnetic flux density $\mathbf{B}$ is given by

$$\mathbf{B} = \mu_0 \mathbf{H} + \mathbf{M}(\mathbf{H}), \tag{3.1}$$

where μ_0 is permeability of vacuum, $\mathbf{H}$ is the magnetic field strength, and $\mathbf{M}$ is magnetic polarization. The $\mathbf{M}$ vector field represents the induced magnetic dipole moments per unit volume. In most MD and discrimination applications involving portable EMI devices, polarization effects have an approximately linear relationship with the applied field [17]; therefore,

$$\mathbf{M}(\mathbf{H}) = \mu_0 \chi_m \mathbf{H}, \tag{3.2}$$

where χ_m is the magnetic susceptibility of the material. The χ_m refers to the degree to which a material becomes magnetized due to the applied magnetic field. Depending on how they respond to the applied field, the magnetic behaviour of materials can be classified into five groups: diamagnetic, paramagnetic, ferromagnetic, ferrimagnetic, and antiferromagnetic. Ferromag-

netic (e.g., iron, nickel) and ferrimagnetic (e.g., magnetite) materials have strong responses to the magnetic field (i.e., $\chi_m \gg 0$), so they are considered as being "magnetic". Diamagnetic (e.g., copper, gold), paramagnetic (e.g., aluminium), and antiferromagnetic (e.g., chromium) materials feature weak magnetic responses (i.e., $\chi_m \approx 0$), so they are often thought of as "non-magnetic". Combining equations (3.1) and (3.2), we can write

$$\mathbf{B} = \mu_0\mathbf{H} + \mu_0\chi_m\mathbf{H} = \mu_0(1+\chi_m)\mathbf{H} = \mu_0\mu_r\mathbf{H}. \tag{3.3}$$

In (3.3), μ_r is relative magnetic permeability. The equation which describes effects in a matter due to an electric field is given by

$$\mathbf{D} = \varepsilon_0\mathbf{E} + \mathbf{P}(\mathbf{E}). \tag{3.4}$$

Here, ε_0 is the permittivity of vacuum, $\mathbf{P}$ is an electric polarization, and $\mathbf{D}$ is a displacement field. In homogenous, linear, and isotropic material, the polarization is assumed to be directly proportional to the external field [17], i.e., $\mathbf{P}(\mathbf{E}) = \varepsilon_0\chi_e\mathbf{E}$. Now, equation (3.4) becomes

$$\mathbf{D} = \varepsilon_0\mathbf{E} + \varepsilon_0\chi_e\mathbf{E} = \varepsilon_0(1+\chi_e)\mathbf{E} = \varepsilon_o\varepsilon_r\mathbf{E}. \tag{3.5}$$

where χ_e is electric susceptibility, and ε_r is relative electric permittivity.

3.1.2 Maxwell's equations

In general, the production and interrelation of magnetic end electric fields are completely described by four fundamental laws known as Maxwell's equations. Although they can be expressed in differential and integral form, for derivation of the induced dipole model, we utilize Maxwell's equations (in vacuum) in differential form (3.6)-(3.9) [87].

$$\nabla \cdot \mathbf{E} = \frac{\rho}{\varepsilon_0} \qquad \text{(Gauss's law)} \tag{3.6}$$

$$\nabla \cdot \mathbf{B} = 0 \qquad \text{(Gauss's law for magnetism)} \tag{3.7}$$

$$\nabla \times \mathbf{E} = -\frac{\partial \mathbf{B}}{\partial t} \qquad \text{(Faraday's Law of Induction)} \tag{3.8}$$

$$\nabla \times \mathbf{B} = \mu_0\mathbf{J} + \mu_0\varepsilon_0\frac{\partial \mathbf{E}}{\partial t} \qquad \text{(Ampère's Law with Maxwell's correction)} \tag{3.9}$$

Gauss's law (3.6) establishes a relationship between electric field $\mathbf{E}$ and the electric charges. It says that the divergence of the $\mathbf{E}$ is proportional to the charge density ρ at that point. According to Gauss's law for magnetism (3.7) the magnetic flux density $\mathbf{B}$ is a divergence-free (i.e., solenoidal) vector field. This law states that lines of $\mathbf{B}$ form closed loops, or in other words,

isolated magnetic poles do not exist. Faraday's law of induction (3.8) is fundamental to understanding EMI phenomena. It says that the time-varying $\mathbf{B}$ give rise to $\mathbf{E}$ circulating around it. The equation (3.9) was first introduced by Ampere, establishing a connection between the rotation of $\mathbf{B}$ and the total current density $\mathbf{J}$. Later, Maxwell completed the law by adding the displacement current term $\varepsilon_0 \frac{\partial \mathbf{E}}{\partial t}$. Maxwell's addition complements Faraday's law, i.e., the time-varying $\mathbf{E}$ give rise to $\mathbf{B}$ circulating around it. The symmetry between the effects of changing electric and magnetic fields is fundamental in explaining the nature of EM waves.

3.1.3 A general solution to magnetic vector potential

To simplify calculations of Maxwell's equations (3.6)-(3.9), a common approach is to express them in terms of electrodynamic potentials. To do so, we utilize the following identities

$$\nabla \cdot (\nabla \times \mathbf{V}) = 0 \tag{3.10}$$

and

$$\nabla \times (\nabla \mathbf{U}) = 0, \tag{3.11}$$

where $\mathbf{V}$ and $\mathbf{U}$ are arbitrary vector field and scalar field, respectively. The definition of magnetic vector potential $\mathbf{A}$ follows from Gauss's low for magnetism (3.7) and vector identity (3.10),

$$\nabla \cdot \mathbf{B} = 0 \rightarrow \nabla \cdot (\nabla \times \mathbf{A}) = 0 \rightarrow \mathbf{B} = \nabla \times \mathbf{A}. \tag{3.12}$$

Inserting (3.12) into (3.8) we get

$$\nabla \times \mathbf{E} = -\frac{\partial}{\partial t}(\nabla \times \mathbf{A}) \rightarrow \nabla \times (\mathbf{E} + \frac{\partial \mathbf{A}}{\partial t}) = 0. \tag{3.13}$$

Equation (3.13) has the same form as (3.11), which allows us to introduce an electric scalar potential φ, such as

$$-\nabla \varphi = \mathbf{E} + \frac{\partial \mathbf{A}}{\partial t} \rightarrow \mathbf{E} = -\nabla \varphi - \frac{\partial \mathbf{A}}{\partial t}. \tag{3.14}$$

Now, by substituting (3.12) and (3.14) to (3.6)-(3.9), the set of four first-order field equations is reduced to two second-order potential equations

$$-\nabla^2 \varphi - \frac{\partial}{\partial t}(\nabla \cdot \mathbf{A}) = \frac{\rho}{\varepsilon_0} \tag{3.15}$$

and

$$(-\nabla^2 + \frac{1}{c^2}\frac{\partial^2}{\partial t^2})\mathbf{A} + \nabla(\nabla \cdot \mathbf{A} + \frac{1}{c^2}\frac{\partial \varphi}{\partial t}) = \mu_0 \mathbf{J}. \tag{3.16}$$

In (3.16), scalar $c = 1/\sqrt{\mu_0 \varepsilon_0}$ denotes the velocity of light in a vacuum [34]. Arbitrariness inherent in the definitions (3.12) and (3.14) for electrodynamic potentials can be utilized to further simplify two coupled differential equations. Specifically, we are allowed to change potentials (by applying some gauge transformation) as long as $\mathbf{B}$ and $\mathbf{E}$ remain the same. For example, the $\mathbf{A}$ field can be transformed by

$$\mathbf{A} \to \mathbf{A}' = \mathbf{A} - \nabla \psi, \tag{3.17}$$

where ψ is a scalar field. According to identity (3.11), $\nabla \times \mathbf{A}' = \nabla \times \mathbf{A}$, so the $\mathbf{B}$ field is unchanged. There are two commonly employed gauges: the Coulomb gauge and the Lorentz gauge [88]. When it comes to quasi-stationary problems, the Coulomb gauge is preferred [88]. In this gauge, the vector potential $\mathbf{A}$ is required to be solenoidal, i.e., $\nabla \cdot \mathbf{A} = 0$. If the $\mathbf{A}$ does not satisfy the gauge condition, we need to perform transformation $\mathbf{A} \to \mathbf{A}'$, (3.17), using the scalar field ψ obtained by solving Poisson's equation

$$\nabla^2 \psi = \nabla \cdot \mathbf{A}. \tag{3.18}$$

By applying the Coulomb gauge to (3.16), we get an inhomogeneous wave equation for the magnetic vector potential

$$(\nabla^2 - \frac{1}{c^2} \frac{\partial^2}{\partial t^2})\mathbf{A} = -\mu_0 \mathbf{J} + \frac{1}{c^2} \frac{\partial \nabla \varphi}{\partial t}. \tag{3.19}$$

The equation (3.19) is called wave equation as its solutions represent waves propagating at the speed c. In the following, the frequency spectrum analysis plays an important role; therefore, it is appropriate to transform the equation (3.19) to FD. The standard approach assumes time-harmonic sources with a frequency $\omega = 2\pi f$. Then, the resulting fields will also be time-harmonic. For $\mathbf{J}(\mathbf{r},t) = \Re\{\mathbf{J}(\mathbf{r},\omega)e^{-j\omega t}\}$, $\mathbf{A}(\mathbf{r},t) = \Re\{\mathbf{A}(\mathbf{r},\omega)e^{-j\omega t}\}$, and $\varphi(\mathbf{r},t) = \Re\{\Phi(\mathbf{r},\omega)e^{-j\omega t}\}$, equation (3.19) becomes inhomogeneous Helmholtz equation in frequency domain, i.e.,

$$\nabla^2 \mathbf{A} + k^2 \mathbf{A} = -\mu_0 \mathbf{J} + j\omega\mu_0\varepsilon_0 \nabla\Phi, \tag{3.20}$$

where $k^2 = \omega^2 \mu_0 \varepsilon_0$ is wavenumber. One way to solve (3.20) is to build an appropriate Green's function and write the solution in the integral form. In particular, a required Green's function $G(\mathbf{r}, \mathbf{r}')$ for Helmholtz equation should satisfy

$$(\nabla^2 + k^2)G(\mathbf{r}, \mathbf{r}') = -4\pi\delta(\mathbf{r} - \mathbf{r}'), \tag{3.21}$$

where $\mathbf{r}'$ and $\mathbf{r}$ are the source and observation points, respectively [89]. We need to specify boundary conditions on fields $\mathbf{A}$ and Φ to find the unique solution. It makes physical sense

to restrict them to be non-zero only within a finite domain; therefore, both potentials vanish asymptotically at infinity [88]. With such conditions, a Green's function (3.21) takes the form [89]

$$G(\mathbf{r}, \mathbf{r}') = \frac{e^{jk|\mathbf{r}-\mathbf{r}'|}}{4\pi|\mathbf{r}-\mathbf{r}'|}. \tag{3.22}$$

Finally, the solution to the initial problem (3.20) is found by convolving the Green's function (3.22) with the source terms, hence,

$$\mathbf{A}(\mathbf{r}, \omega) = \int_V \frac{e^{jk|\mathbf{r}-\mathbf{r}'|}}{4\pi|\mathbf{r}-\mathbf{r}'|} \left(-\mu_0 \mathbf{J}(\mathbf{r}', \omega) + j\omega\mu_0\varepsilon_0 \nabla\Phi(\mathbf{r}', \omega)\right) dv'. \tag{3.23}$$

In (3.23), integration is done over domain $V \in \mathbb{R}^3$, for all source points $r' \in V$.

3.1.4 Quasi-magnetostatic approximation

Further simplification of equation (3.23) can be done by considering some practical aspects of the targeted EMI application. Note that solution (3.23) for magnetic vector potential contains exponential term $e^{jk|\mathbf{r}-\mathbf{r}'|}$ under the integral. This term, which is commonly called retardation, incorporates the time delay of the wave propagation. Given the typical frequency range of EMI devices employed for landmine clearance (i.e., < 100 kHz) and interrogation distances $|\mathbf{r} - \mathbf{r}'|$ on the order of tens of centimetres, propagation effects of EM waves can be neglected, i.e.,

$$k|\mathbf{r} - \mathbf{r}'| = \frac{\omega|\mathbf{r} - \mathbf{r}'|}{c} = \frac{2\pi|\mathbf{r} - \mathbf{r}'|}{\lambda} \ll 1 \rightarrow e^{jk|\mathbf{r}-\mathbf{r}'|} \approx 1. \tag{3.24}$$

Next, by imposing a Coulomb gauge condition $\nabla \cdot \mathbf{A} = 0$, an electric field (3.14) is divided into irrotational component $-\nabla\varphi$ due to electric charges and solenoidal component $-\partial\mathbf{A}/\partial t$ due to the time-varying magnetic field. In EMI systems for MD, it is typically assumed that there is no accumulation of electric charges within the object volume [90]. This means that the term $\nabla\Phi$ in (3.23) can also be neglected. Therefore, the only source of magnetic vector potential is current density. In general, total current density $\mathbf{J}$ can be expressed as

$$\mathbf{J} = \mathbf{J}_f + \mathbf{J}_M + \mathbf{J}_P = \sigma\mathbf{E} + \nabla \times \mathbf{M} + j\omega\mathbf{P} = \sigma\mathbf{E} + \nabla \times \mu\mathbf{H} + j\omega\varepsilon_0(\varepsilon_r - 1)\mathbf{E} \tag{3.25}$$

where $\mathbf{J}_f$ is free current, $\mathbf{J}_M$ is magnetisation current, and $\mathbf{J}_P$ is electric polarisation current. A free current induced by a solenoidal component of $\mathbf{E}$ is called an eddy current. For slowly-varying current density (i.e., $\sigma \gg \omega\varepsilon_0\varepsilon_r$), the eddy current term $\sigma\mathbf{E}$ is assumed to dominate the displacement currents $j\omega\varepsilon_0\varepsilon_r\mathbf{E}$ (more details are available in [17], page 63). Hence, we can remove $\mathbf{J}_P$ from (3.25). Taking into account the above approximations, equation (3.23) becomes

$$\mathbf{A}(\mathbf{r}, \omega) = \frac{\mu_0}{4\pi} \int_V \frac{\mathbf{J}_{\text{f}}(\mathbf{r}', \omega) + \mathbf{J}_{\text{M}}(\mathbf{r}', \omega)}{|\mathbf{r} - \mathbf{r}'|} \, dv'. \tag{3.26}$$

The derivation of (3.26) from (3.23) to simplify the solution for magnetic vector potential $\mathbf{A}$ is called quasi-magnetostatic approximation [91].

3.2 Forward modelling of EMI phenomena

This section utilizes the expression (3.26) to derive an approximate forward model, known as the induced dipole model, which relates EMI sensor measurements with the object's intrinsic features.

3.2.1 Approximation of the expression for magnetic vector potential

In electromagnetism, magnetic moment describes the strength and orientation of a magnet or any object that produces a magnetic field. Magnetic moment originates from remnant and induced object magnetization $\mathbf{M}$, free current distribution $\mathbf{J}_{\text{f}}$, or the combination of both [92], Fig. 3.1. As discussed earlier, a metallic object placed in a time-varying magnetic field produces a secondary field due to magnetization ($\mathbf{M}$) and eddy currents ($\mathbf{J}_{\text{f}}$). The secondary field can be represented by induced magnetic moment, as shown below.

To simplify the analysis, let us rewrite (3.26) by introducing an effective current distribution $\mathbf{J}_{\text{ef}} = \mathbf{J}_{\text{f}} + \mathbf{J}_{\text{M}}$; therefore,

$$\mathbf{A}(\mathbf{r}) = \frac{\mu_0}{4\pi} \int_V \frac{\mathbf{J}_{\text{ef}}(\mathbf{r}')}{|\mathbf{r} - \mathbf{r}'|} \, dv'. \tag{3.27}$$

Domain notation is dropped as the following analysis is valid in both TD and FD. For small objects or those sufficiently far from the sensor (i.e., $|\mathbf{r}| \gg |\mathbf{r}'|$), we can apply Taylor expansion of the $1/|\mathbf{r} - \mathbf{r}'|$, which yields

$$\frac{1}{|\mathbf{r} - \mathbf{r}'|} = \frac{1}{|\mathbf{r}|} + \frac{\mathbf{r} \cdot \mathbf{r}'}{|\mathbf{r}|^3} + \cdots. \tag{3.28}$$

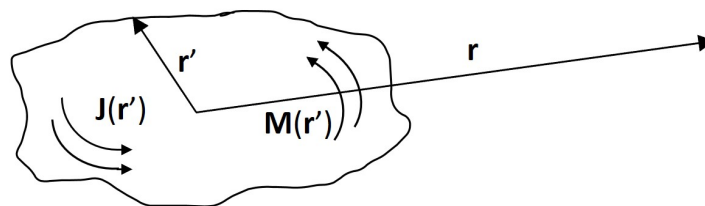Now, the (3.27) can be expressed as

Figure 3.1: Current distribution within the object volume. The observation point $\mathbf{r}$ lies outside the object.

$$\mathbf{A}(\mathbf{r}) = \frac{\mu_0}{4\pi} \left(\int_V \frac{\mathbf{J}_{\text{ef}}(\mathbf{r}')}{|\mathbf{r}|} \, dv' + \int_V \frac{\mathbf{r} \cdot \mathbf{r}'}{|\mathbf{r}|^3} \mathbf{J}_{\text{ef}}(\mathbf{r}') \, dv' + \cdots \right). \tag{3.29}$$

The magnitude of each subsequent term of $\mathbf{A}$ decreases rapidly by factor $\mathbf{r}'/\mathbf{r}$, so the first non-zero term will dominate the response (detailed derivation is available in [87], page 185). The first non-zero term is the second one, i.e., the magnetic dipole term. Therefore, this is called the magnetic dipole approximation and is a widely used approach to simplify the expression for $\mathbf{A}$ when it comes to detection and characterization of small metallic objects using EMI sensing [17, 34, 69]. Consequently, the expression (3.29) reduces to

$$\mathbf{A}(\mathbf{r}) \approx \frac{\mu_0}{4\pi} \cdot \frac{\mathbf{m} \times \hat{\mathbf{r}}}{|\mathbf{r}|^2}, \tag{3.30}$$

where $\hat{\mathbf{r}}$ is a unit vector pointing towards the observation point, and $\mathbf{m}$ is the magnetic dipole moment, which can be expressed as a linear combination of the eddy current term $\mathbf{m}_{\text{j}}$ and magnetization term $\mathbf{m}_{\text{M}}$ [93], i.e.,

$$\mathbf{m} = \underbrace{\frac{1}{2} \int_V \mathbf{r}' \times \mathbf{J}_{\text{f}}(\mathbf{r}') \, dv'}_{\mathbf{m}_{\text{j}}} + \underbrace{\int_V \mathbf{M}(\mathbf{r}') \, dv'}_{\mathbf{m}_{\text{M}}} = \frac{\sigma}{2} \int_V \mathbf{r}' \times \mathbf{E}(\mathbf{r}') \, dv' + (\mu_r - 1) \int_V \mathbf{H}(\mathbf{r}) \, dv'. \tag{3.31}$$

3.2.2 Metallic object response due to induced magnetic dipole moment

According to Faraday's law of induction, the time-varying (secondary) magnetic field generated by the induced magnetic dipole creates the electric field (i.e., voltage) in the receiver coil of the EMI sensor. An equation which describes this phenomenon is given by

$$u_{\text{ind}}(t) = \oint_C \mathbf{E} \, d\mathbf{l}, \tag{3.32}$$

where $d\mathbf{l}$ is the infinitesimal segment of a path length through the wire of a closed contour C, which is a current loop of the receiver coil. An integral form of Faraday's law of induction followed by Stoke's theorem gives the relationship between electric field $\mathbf{E}$ and magnetic vector potential $\mathbf{A}$,

$$\oint_C \mathbf{E} \, d\mathbf{l} = -\oint_C \frac{\partial \mathbf{A}}{\partial t} \, d\mathbf{l}. \tag{3.33}$$

Using (3.33) and (3.30), the expression for u_{ind}, (3.32), can be rewritten in the form

$$u_{\text{ind}}(t) = -\frac{\mu_0}{4\pi} \frac{\partial}{\partial t} \oint_C \frac{\mathbf{m}(t) \times \hat{\mathbf{r}}}{|\mathbf{r}|^2} \, d\mathbf{l} = -\frac{\mu_0}{4\pi} \frac{\partial \mathbf{m}(t)}{\partial t} \oint_C \frac{d\mathbf{l} \times \hat{\mathbf{r}}}{|\mathbf{r}|^2}. \tag{3.34}$$

Further simplification is possible by applying the Biot-Savart law, which provides means to

calculate the flux **B** radiated by a current loop, i.e.,

$$\mathbf{B} = \nabla \times \mathbf{A} = \frac{\mu_0 I}{4\pi} \oint_C \frac{\mathrm{d}\mathbf{l} \times \hat{\mathbf{r}}}{|\mathbf{r}|^2}, \tag{3.35}$$

where I is the current running through the loop. Applying (3.35) to (3.34), we get the expression for u_{ind} due to induced magnetic dipole **m**,

$$u_{ind}(t) = -\mu_0 \frac{\partial \mathbf{m}(t)}{\partial t} \frac{\mathbf{H}_{\mathrm{RX}}}{i_{\mathrm{RX}}}. \tag{3.36}$$

In (3.36), $\mathbf{H}_{\mathrm{RX}}/i_{\mathrm{RX}}$ is a geometrical term depending on receiver coil geometry and the distance/orientation between the coil and the magnetic dipole. An equivalent expression in FD is given by

$$U_{\mathrm{ind}}(\omega) = -\mathrm{j}\omega\mu_0 \mathbf{m}(\omega) \frac{\mathbf{H}_{\mathrm{RX}}}{I_{\mathrm{RX}}}. \tag{3.37}$$

Equations (3.36) and (3.37) still provide a rather complex relationship between measurements (i.e., u_{ind}, U_{ind}) and object size, shape, and material (σ, μ_r) properties, due to expression for magnetic dipole moment (3.31). In general, the calculation of **m** requires the use of computationally demanding numerical methods (e.g., Finite Element Method). However, the same assumptions required by dipole model approximation allow the use of a significantly simplified form for **m**, which is further discussed below.

Frequency domain operation

If the transmitted field $\mathbf{H}_{\mathrm{TX}}$ is homogenous within the object volume, the **m** can be represented as the product of magnetic polarizability tensor (MPT) **M** and the transmitted magnetic field $\mathbf{H}_{TX}$ [17, 94], thus

$$\mathbf{m}(\omega) = \mathbf{M}(\omega) \cdot \mathbf{H}_{TX}(\omega), \tag{3.38}$$

where

$$\mathbf{M}(\omega) = \begin{bmatrix} M_{xx}(\omega) & M_{xy}(\omega) & M_{xz}(\omega) \\ M_{yx}(\omega) & M_{yy}(\omega) & M_{yz}(\omega) \\ M_{zx}(\omega) & M_{zy}(\omega) & M_{zz}(\omega) \end{bmatrix}. \tag{3.39}$$

M is a symmetric 3×3 matrix containing six independent complex elements (i.e., $M_{xy} = M_{yx}$, $M_{xz} = M_{zx}$, $M_{yz} = M_{zy}$) that depend on the excitation frequency, as well as on the orientation and intrinsic features of the object under inspection [95]. Reduction from nine to six

elements results from Lorentz reciprocity theorem, which states that the response remains the same if the sources (i.e., receiver and transmitter coils) are interchanged [93]. The equation (3.38) was first proposed by Landau and Lifshitz in 1960 [96]. Later, Baum elaborated that it holds for arbitrarily shaped objects [34]. In general, the field within the object volume will be homogenous for small objects or sufficiently far from the sensor. Authors in [97] state that "the approximation expressed by (3.38) is expected to be reasonable at target ranges three or four times the target size or greater".

Including (3.38) into (3.37), we get the final expression for the response of the FD EMI sensor to the induced magnetic dipole, i.e.,

$$\mathbf{U}_{ind}(\omega) = -\mathrm{j}\omega\mu_0 I_{TX_0} \frac{\mathbf{H}_{TX}^T}{I_{TX}} \mathbf{M}(\omega) \frac{\mathbf{H}_{RX}}{I_{TX}}, \tag{3.40}$$

where I_{TX_0} is the magnitude of the transmitter current.

Time domain operation

The multiplication in FD transforms to convolution in TD [69]; therefore, the dipole moment can be represented as the convolution of $\mathbf{M}(t)$ and $\mathbf{H}_{TX}(t)$,

$$\mathbf{m}(t) = \mathbf{M}(t) * \mathbf{H}_{TX}(t). \tag{3.41}$$

Symmetric real non-negative matrix $\mathbf{M}$ is the TD representation of MPT. In the case of TD EMI sensors, a step-off field is usually utilized to illuminate the object under inspection. Thus, $\mathbf{H}_{TX}(t)$ can be modelled by the unit step-off function $S(-t)$ for $t \geq 0$,

$$\mathbf{H}_{TX}(t) \approx \mathbf{I}_0 \frac{\mathbf{H}_{TX}}{I_{TX}} S(-t), \tag{3.42}$$

where $\mathbf{I}_0$ is the current running through the coil during transmitter on-time. Inserting (3.42) into (3.41) and considering the differentiation property of the convolution yields

$$\frac{\partial \mathbf{m}(t)}{\partial t} = \mathbf{M}(t) * \frac{\partial \mathbf{H}_{TX}(t)}{\partial t} \approx -\mathbf{I}_0 \frac{\mathbf{H}_{TX}}{i_{TX}} \mathbf{M}(t). \tag{3.43}$$

Combining (3.43) and (3.36), we get final expression for u_{ind} in TD,

$$\mathbf{u}_{ind}(t) \approx \mu_0 I_0 \frac{\mathbf{H}_{TX}^T}{i_{TX}} \mathbf{M}(t) \frac{\mathbf{H}_{RX}}{i_{TX}}. \tag{3.44}$$

The separation of object orientation and intrinsic features can be done by eigenvalue decomposition or diagonalization of the matrix $\mathbf{M}$,

$$\mathbf{M}(t) \approx \mathbf{D}^T \begin{bmatrix} \lambda_{11}(t) & 0 & 0 \\ 0 & \lambda_{22}(t) & 0 \\ 0 & 0 & \lambda_{33}(t) \end{bmatrix} \mathbf{D}. \tag{3.45}$$

In FD, decomposition is done separately for the real and imaginary parts. The eigenvalues $(\lambda_{11}\text{-}\lambda_{33})$ are time dependent coefficients that convert the three components of the transmitted field into the three components of the magnetic dipole moment induced at the object centre [34]. They provide orientation-independent information on an object's size, shape and material properties and are, therefore, an essential tool for metallic object characterization using EMI sensing. The eigenvectors of $\mathbf{M}$ are columns of the matrix $\mathbf{D}$ and contain the spatial orientation of the object's principal axes. In practice, it is commonly assumed that eigenvectors are time (or frequency) independent, as this allows the separation of an object's orientation and its intrinsic features (approximate eigenvalues) [69, 98]. The assumption above was used throughout this thesis.

In a system where measurements are obtained over multiple locations N, equation (3.44) can be rewritten into a matrix form, leading to an expression for the forward model

$$\mathbf{u}_{ind}(t) = \mathbf{S} \cdot \mathbf{M}_v(t) \cdot k = \mathbf{f}_{FWD}(\mathbf{r}_{object}, \mathbf{M}_v(t)), \tag{3.46}$$

$$\mathbf{S} = \begin{bmatrix} \mathbf{H}_{x\_TX} \circ \mathbf{H}_{x\_RX} \\ \mathbf{H}_{x\_TX} \circ \mathbf{H}_{y\_RX} + \mathbf{H}_{y\_TX} \circ \mathbf{H}_{x\_RX} \\ \mathbf{H}_{x\_TX} \circ \mathbf{H}_{z\_RX} + \mathbf{H}_{z\_TX} \circ \mathbf{H}_{x\_RX} \\ \mathbf{H}_{y\_TX} \circ \mathbf{H}_{y\_RX} \\ \mathbf{H}_{y\_TX} \circ \mathbf{H}_{z\_RX} + \mathbf{H}_{z\_TX} \circ \mathbf{H}_{y\_RX} \\ \mathbf{H}_{z\_TX} \circ \mathbf{H}_{z\_RX} \end{bmatrix}^T = \begin{bmatrix} \mathbf{S}_{xx} \\ \mathbf{S}_{xy} \\ \mathbf{S}_{xz} \\ \mathbf{S}_{yy} \\ \mathbf{S}_{yz} \\ \mathbf{S}_{zz} \end{bmatrix}^T \tag{3.47}$$

$$\mathbf{M}_v = \begin{bmatrix} \mathbf{M}_{xx} & \mathbf{M}_{xy} & \mathbf{M}_{xz} & \mathbf{M}_{yy} & \mathbf{M}_{yz} & \mathbf{M}_{zz} \end{bmatrix}^T, \tag{3.48}$$

where $\mathbf{S}$ is the $N \times 6$ sensitivity matrix that depends on the object's location $\mathbf{r}_{object}$ relative to the EMI sensor transmitter (TX)/receiver (RX) coils, $\mathbf{M}_v$ is a 6×1 vector containing six independent elements of directional magnetic polarizabilities, and k is a calibration constant that depends on the excitation current and coil design [70]. $\mathbf{S}$ contains cross-coupled contributions of the $x-$, $y-$ and $z-$components of magnetic filed $\mathbf{H}$ calculated for TX and RX coil at different object positions $\mathbf{r}_{object}$.

Equation 3.46 can be further rearranged in the form

$$\mathbf{u}_{ind}(t) = \mathbf{F} \cdot \lambda(t) \cdot k = \mathbf{f}_{FWD}(\mathbf{r}_{obj}, \varphi, \theta, \psi, \lambda(t)). \tag{3.49}$$

$\mathbf{F}$ is the $N \times 3$ forward matrix containing field contributions to eigenvalues λ_{11}-λ_{33} depending on the object's location $\mathbf{r}_{object}$ and orientation (yaw ψ, pitch θ, and roll φ angles) while λ is time dependant vector of the object's eigenvalues.

This concludes the forward modelling of EMI phenomena. The forward models in the form of (3.46) or (3.49) linking measurements with the object's features, location, and orientation are used in each subsequent study presented in this thesis.

3.3 Magnetic polarizability tensor measurement

Recently, Ledger and Lionheart have provided new insights into the properties of MPT and the rigorous mathematical justification of the conditions required for the magnetic dipole approximation to be valid [93, 99, 100]. Based on the work of Ammari *et al.* [101], Ledger and Lionheart derived an explicit formula for the calculation of symmetric rank 2 MPT in the case of arbitrarily shaped objects [93]. Following this, an MPT-Calculator software for rapid simulations of MPT in FD was developed [102]. The MPT-Calculator allows the construction of large dictionaries of MPTs for various conductive and permeable objects in a relatively short time [103].

In recent decades, the MPT has been used as a tool for hidden object detection by various researchers [60, 81, 104, 105, 106, 107, 108, 109]. When MPT coefficients need to be obtained from EMI sensor measurements, the standard engineering approach employs (3.40) or (3.44) in FD and TD, respectively. The main problem with this approach is that the MPT is not measured directly, but rather, a nonlinear inverse problem must be solved to obtain both the MPT and the object's location. As discussed, this requires EMI data with high diversity obtained by complex multi-receiver sensor designs [65, 110, 111] or by EMI sensors systems in combination with separate tracking systems [112]. The inverse problem may become ill-posed due to strong correlations between the MPT parameters and the object location [72, 112]. Moreover, complexities increase due to external interferences (e.g. soil effects) [106], uncertainties in sensor data (e.g., EMI sensor noise, positional errors) [113], as well as unfavourable combinations of object type and interrogation geometry [114]. Given the above challenges, linking MPTs derived numerically and those acquired through measurements is difficult. Consequently, modern systems featuring metallic object discrimination usually rely on libraries of measured MPTs [105, 106, 109]. These libraries are susceptible to error due to uncertainties in the sensor data, which are system-specific. Therefore, libraries must be created for each system individually, which is time-consuming and poses one of their main limitations in practice.
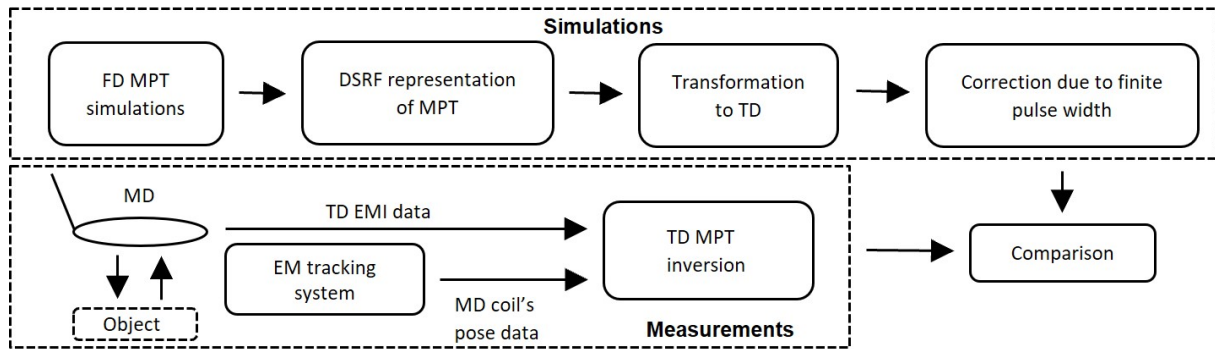
Figure 3.2: Flow chart of the proposed approach for validation of MPT measurement in TD [119].

The above discussion brings us to the ultimate goal: the development of a system leveraging libraries created from MPT simulations instead of measurements to improve metallic object discrimination capabilities. To accomplish this, we first need to establish a relationship between MPT measurements and simulations. Several laboratory systems for MPT measurements in a controlled environment have been proposed to relate MPTs obtained from measurements to MPT simulations (or analytical solutions if they exist). Experiments involve automated and manual manipulation of the object's pose to record responses from different object angles. The system that takes advantage of a laboratory positioner with five degrees of freedom for MPT measurements (in the form of discrete relaxations) was proposed in [115]. Later, the authors developed another system that is more compact and requires less time for measurement [116]. Researchers at the University of Manchester developed a static system with multiple coil arrays for FD MPT measurement of symmetrical objects with diameters up to 130 mm [117, 118].

An important challenge remains whether portable EMI systems can measure MPT reliably rather than relying on complex laboratory setups. The established MPT theory and the state-of-the-art MPT measurement systems rely mainly on the FD representation of the MPT and its spectral signatures. However, many modern EMI systems for hidden object detection operate in TD. Therefore, there is a clear need to provide a better understanding of how the theory and measurements can be mapped between the two domains.

The remainder of this chapter presents an inversion-based measurement of MPT using a monocoil pulse induction MD in combination with an EM tracking system. The flow chart of the proposed approach is given in Fig. 3.2. First, the simulations and methodology used to compare FD and TD MPT are described. This is followed by a description of the algorithm used for MPT estimation. Next, the experimental setup used to evaluate the performance is presented. Finally, this chapter concludes with results and discussion.

3.3.1 Simulations

MPT simulator

FD MPTs are calculated using MPT-Calculator software [120], which implements the procedure proposed in [102]. This simulator enables efficient computation of MPTs since it requires the calculation of only a small number of snapshots, i.e., full-order model solutions obtained with NGSolve software [121]. Full-order model solutions are approximate solutions to a transmission problem (equations (6) and (7) in [102]), from which the MPT coefficients are computed in the post-processing with explicit expressions (equation (5) in [102]). To increase computational efficiency, snapshots are used to obtain solutions for all other frequencies by applying a reduced-order model based on a proper orthogonal decomposition (see Section 4 in [102] for more details). Once the MPT of an object is obtained, it is possible to calculate MPTs of other objects with the same shape but different sizes and/or electrical conductivity simply by scaling the results, which allows additional time savings (see Section 5 in [102] for more details). The use of the MPT-Calculator software for the generation of the MPT library is readily available elsewhere [83, 103], so details related to the MPT simulation procedure are omitted here for brevity.

DSRF represenation

In his study of EMI phenomena, Baum has provided a theoretical basis to represent the EMI response as a discrete sum of damped real exponentials [122]. In [50], the authors suggest an equivalent approach in FD, i.e., FD EMI response can be represented as the sum of relaxation frequencies. As the EMI response is proportional to the projection of the object's MPT eigenvalues (3.40), we can write

$$\lambda(\omega) = c_0 + \sum_{k=1}^{K} \frac{c_k}{1 + \mathrm{j}\omega/\zeta_k}, \tag{3.50}$$

where (c_k, ζ_k) represents each pair of relaxation frequency ζ_k and its corresponding spectral amplitude c_k, K is the model order, and c_0 is the DC offset [50]. All pairs of relaxation frequencies make set $S = \{(c_k, \zeta_k) : k = 1, ...K\}$, often referred to as a discrete spectrum of relaxation frequencies (DSRF) [50]. As the DSRF provides a very intuitive way of understanding the object's intrinsic signatures, it has attracted considerable attention in the context of object identification [50, 123, 124]. In this study, we take advantage of the DSRF form of MPTs, as it allows a straightforward conversion of FD MPT to its equivalent in TD. For DSRF estimation, a method similar to that proposed in [50] is employed, which does not require a priori knowledge of the model order K and always returns real parameters. With MPT eigenvalues simulated at N logarithmically spaced frequencies, (3.50) can be rewritten in a matrix form

$$\lambda = \mathbf{Z}\mathbf{c}, \tag{3.51}$$

$$\lambda = \begin{bmatrix} \lambda(\omega_1) & \lambda(\omega_2) & \dots & \lambda(\omega_N) \end{bmatrix}^T, \tag{3.52}$$

$$\mathbf{Z} = \begin{bmatrix} 1 & \frac{1}{1+j\omega_1/\zeta_1} & \frac{1}{1+j\omega_1/\zeta_2} & \cdots & \frac{1}{1+j\omega_1/\zeta_K} \\ 1 & \frac{1}{1+j\omega_2/\zeta_1} & \frac{1}{1+j\omega_2/\zeta_2} & \cdots & \frac{1}{1+j\omega_2/\zeta_K} \\ \vdots & \vdots & \vdots & \ddots & \vdots \\ 1 & \frac{1}{1+j\omega_N/\zeta_1} & \frac{1}{1+j\omega_N/\zeta_2} & \cdots & \frac{1}{1+j\omega_N/\zeta_K} \end{bmatrix}, \tag{3.53}$$

$$\mathbf{c} = \begin{bmatrix} c_0 & c_1 & c_2 & \dots & c_K \end{bmatrix}^T, \tag{3.54}$$

where $\mathbf{Z}$ is $N \times (K+1)$ matrix containing K relaxation frequencies, $\mathbf{c}$ is $(K+1) \times 1$ vector with corresponding spectral amplitudes and shift c_0. DSRF is estimated by finding the solution to

$$\underset{\mathbf{c}}{\arg\min} \left(||\mathbf{Z}'\mathbf{c} - \lambda'|| \right), \mathbf{c} \geq 0, \tag{3.55}$$

where

$$\mathbf{Z}' = \begin{bmatrix} \Re(\mathbf{Z}) \\ \Im(\mathbf{Z}) \end{bmatrix} \text{ and } \lambda' = \begin{bmatrix} \Re(\lambda) \\ \Im(\lambda) \end{bmatrix}. \tag{3.56}$$

Here, the system of real equations is obtained by separating the real and imaginary parts of $\mathbf{Z}$. A real value is added to frequency response λ to ensure that c_0 is positive. The solution to (3.55) is obtained using a non-negative least square solver *nnls* available in Python (SciPy library).

MPT transformation to the time domain

Once DSRF pairs are estimated, the transformation of the MPT eigenvalues from FD to TD is done using inverse Fourier transform

$$\lambda(t) = \mathscr{F}^{-1}(\lambda(\omega)) = \sum_{k=1}^{K} c_k \zeta_k e^{-t\zeta_k}, t > 0. \tag{3.57}$$

The shift term c_0 in (3.50), which becomes $c_0\delta(t)$ in TD, is neglected as it vanishes for $t > 0$.

The method utilized in this thesis presumes non-negative model parameters $\mathbf{c} \geq 0$, which
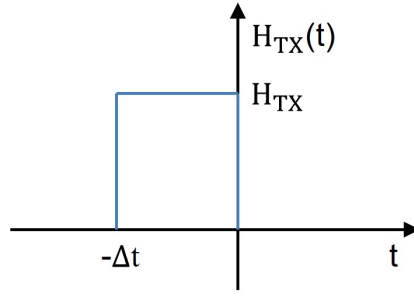
Figure 3.3: Waveform of transmitted pulse [119].

is valid for most of the objects [50]. For a more general approach, which allows negative relaxations, one may employ the method proposed in [125].

Correction due to finite pulse width

Equation (3.44) does not take into account the finite width of the transmitter pulse of the TD MD, Fig. (3.3). A change in the width of the transmitted pulse will affect the induced dipole moment, which will then be reflected in estimated eigenvalues [39]. As each eigenvalue is affected in the same manner, it is enough to analyze one of them. Further, let's assume an eigenvalue having a single relaxation ζ (e.g., thin wire loop [50]), thus

$$\lambda_{step}(t) = A\zeta e^{-t\zeta}, \tag{3.58}$$

where A is the relaxation amplitude. Now, we can write expression for the uniaxial magnetic moment

$$m_{meas}(t) = \lambda_{step}(t) * H_{TX}(t) = \int_{-\infty}^{\infty} H_{TX}(\tau)A\zeta e^{-(t-\tau)\zeta}\,d\tau. \tag{3.59}$$

$H_{TX}(t)$ is a transmitted field in the direction of the λ_{step}'s principal axis. Considering that $H_{TX}(t)$ starts at $-\Delta t$ and collapses to zero at $t = 0$, (3.59) can be rewritten as

$$m_{meas}(t) = \int_{-\Delta t}^{0} H_{TX}A\zeta e^{-(t-\tau)\zeta}\,d\tau. \tag{3.60}$$

Taking the time derivative, we arive to the final expression

$$\frac{\partial m_{meas}(t)}{\partial t} = -H_{TX}\underbrace{(1 - e^{-\Delta t\zeta})A\zeta e^{-t\zeta}}_{\lambda_{pulse}}. \tag{3.61}$$

Comparing λ_{pulse} and λ_{step} (3.58), the reduction of exponential decay is proportional to factor $1 - e^{-\Delta t\zeta}$. Having this in mind, we can write a general expression for estimated eigenvalues represented with a sum of damped exponentials

$$\lambda_{pulse}(t) = \sum_{k=1}^{K} c_k(1 - e^{-\Delta t \zeta_k}) \zeta_k e^{-t \zeta_k}, t > 0. \tag{3.62}$$

Thus, measured eigenvalues will have reduced amplitudes due to the finite length of the transmitted pulse. To compare simulations with the measurements, the simulations are first transformed to TD using (3.50)-(3.57), then each term in (3.57) is multiplied with the corresponding factor $1 - e^{-\Delta t \zeta}$ to account for pulse length. An alternative approach is to represent measurements in DSRF form and divide each term by $1 - e^{-\Delta t \zeta}$. However, this involves an additional estimation of the DSRF coefficients, which can lead to unstable and erroneous estimates due to measurement uncertainties.

3.3.2 NLS-based MPT inversion

Given measurements $\mathbf{u}_{meas}$ and forward model (3.49), unknowns (i.e., $\mathbf{r}_{obj}, \varphi, \theta, \psi, \lambda$) can be estimated by finding the solution to

$$\underset{\mathbf{r}_{obj}, \varphi, \theta, \psi, \lambda}{\operatorname{argmin}} \left(||\mathbf{u}_{meas} - \mathbf{f}_{FWD}(\mathbf{r}_{obj}, \varphi, \theta, \psi, \lambda(t))||^2 \right), \tag{3.63}$$

where the $||\cdot||$ is L2-norm. As a high data diversity is required for MPT estimation, the number of measurements is much higher than the number of unknowns. Thus, we are dealing with an overdetermined problem. A pseudo-code of the algorithm (implemented in MATLAB) is given in Table 3.1.

Table 3.1: Pseudo-code of NLS inversion [119].

Initialization of object's location and orientation:
$\mathbf{r}_{obj\_init}(x,y) = \underset{x,y}{\operatorname{argmax}}(\mathbf{u}_{meas}(\mathbf{r}_{sensor\_max}))$
$\mathbf{r}_{obj\_init}(z) = FWHM(\mathbf{u}_{meas})$
$\varphi_{init}, \theta_{init}, \psi_{init} = \mathbf{0}$

Initialization of eigenvalues:
$\lambda_{init} = \mathbf{F}_{init}^{\dagger}\mathbf{u}_{meas}, \lambda_{init} \geq 0$

Solve the nonlinear least squares problem with constraints:
$\underset{\substack{\mathbf{r}_{obj}, \varphi, \theta, \\ \psi, \lambda_{NLS}}}{\operatorname{argmin}} \left(||\mathbf{u}_{meas} - \mathbf{f}_{FWD}||^2 \right), \begin{cases} \lambda_{NLS} \geq 0 \\ -2 < \mathbf{r}_{obj}(z) < -20\, cm \end{cases}$

Final estimate of eigenvalues:
$\lambda = \mathbf{F}^{\dagger}\mathbf{u}_{meas}, \lambda \geq 0$

The algorithm starts with an initial estimate of the object's location and orientation. The
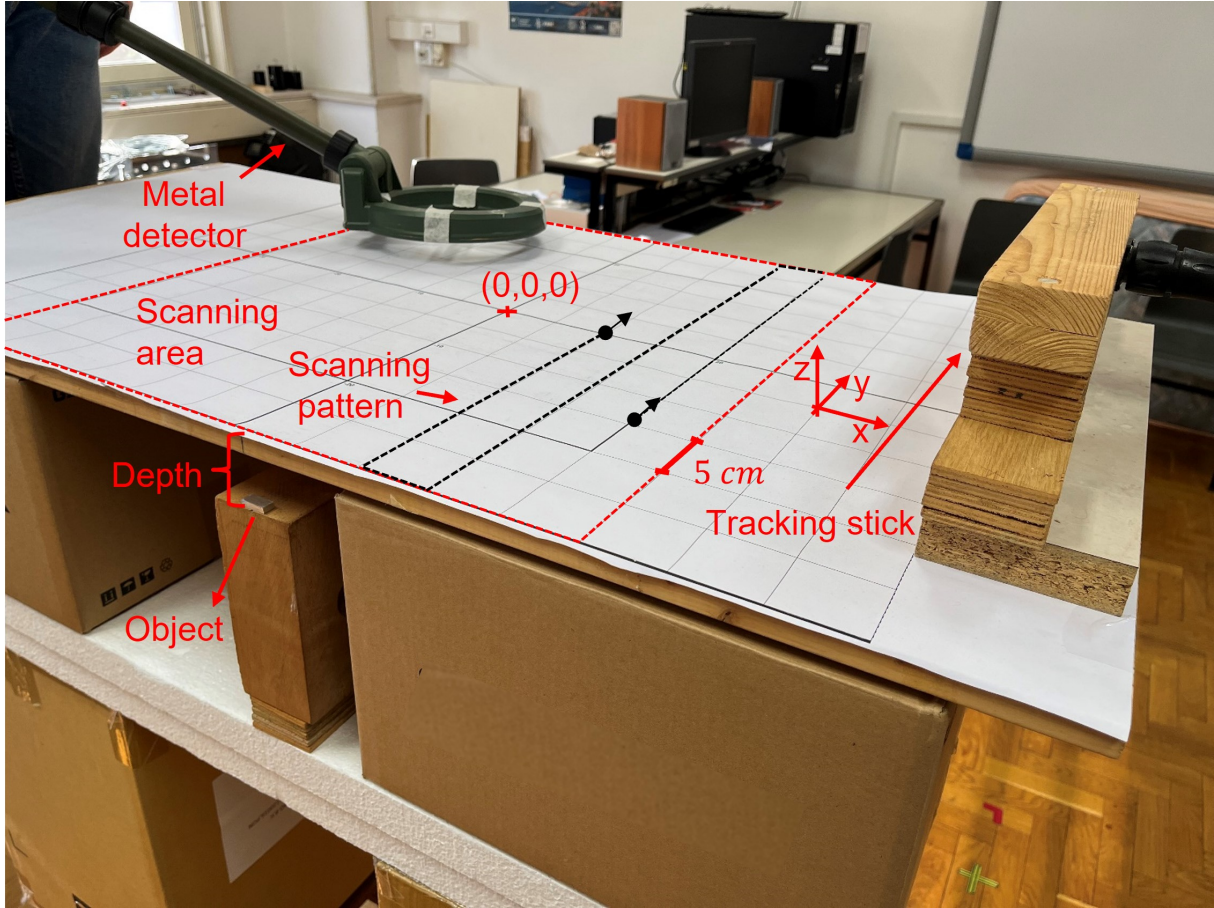
Figure 3.4: Eperimental setup: VMF4 metal detector and EM tracking system [119].

MD coil's horizontal coordinates where the maximum response was measured are assigned to the object's horizontal coordinates $\mathbf{r}_{obj\_init}(x,y)$. The initial depth of the object $\mathbf{r}_{obj\_init}(z)$ is estimated using the FWHM (full-width at half-maximum) approach [126]. Object's orientation angles (i.e., $\psi_{init}, \varphi_{init}, \theta_{init}$) are initialized to zero. The first estimate of eigenvalues is obtained by solving a constrained linear least-squares problem, where $\mathbf{F}_{init}^{\dagger}$ is the Moore-Penrose pseudo-inverse of the forward matrix $\mathbf{F}_{init}$. The constraint sets the lower bound of λ_{init} to zero due to the decaying nature of TD response [70].

Once unknowns are initialized, the NLS problem with constraints is solved to obtain a final estimate of the object's location $\mathbf{r}_{obj}$ and orientation (ψ, φ, θ). Considering the practical aspects of the targeted application, the second constraint is added to bound the depth solution range. The NLS problem is solved using MATLAB's built-in *lsqnonlin* function with the trust-region-reflective algorithm. Using the $\mathbf{r}_{obj}$ and (ψ, φ, θ), the final estimate of eigenvalues λ is obtained in a linear least-squares fashion. The most sensitive part of the algorithm is the nonlinear estimation of the location, where most difficulties come from depth estimation [127]. However, the goal of this work is to demonstrate the feasibility of the proposed system to estimate MPT and not to test its performance under critical scenarios. Therefore, all measurements are made over objects placed at lower depths (< 10 cm) for which NLS performs well [127].

(a) Balls of different sizes (with diameters of 5 mm and 8 mm) and materials (stainless steel, aluminium, and brass).

(b) Cuboids and PMA-1 landmine fuse (hollow aluminium cylinder).

Figure 3.5: Test objects [119].

3.3.3   Experimental setup

Fig. 3.4 illustrates the physical implementation of the experimental setup. A pulse induction MD manufactured by Vallon GmbH (model VMF4 [32]) was employed for measurements. MD generates a repeating sequence of positive and negative excitation pulses (on-time $t_{on} \approx 50\,\mu$s, frequency $f_p \approx 523$ Hz) from a circular coil ($\Phi = 20$ cm). A portable search head tracking system was employed to obtain five degrees of freedom information on the MD coil's pose [75]. The tracking system yields a mean absolute error of less than 3 mm for the MD coil's x- and y-coordinates, less than 2 mm for the z-coordinate, and less than $0.5°$ for the pitch and roll angles. An averaging window of $N_{avg} = 20$ (discretization time of ≈ 38 ms) was used to acquire the MD full decay response and the corresponding coil's pose data. The MD data are acquired at 97 TGs over the time window of 87 us.

Measurements were made under laboratory conditions over non-ferrous objects varying in shape, size, and material properties, Fig. 3.5, Table 3.2. The objects were placed under the measurement grid ($x_{obj} \approx 0$, $y_{obj} \approx 0$, $z_{obj} \approx -5$ cm) and aligned along y-axis, Fig. 3.4. The first group of objects used in experiments include balls of precisely defined sizes and materials [128], Fig. 3.5a. The second group consists of manually made cuboid objects and hollow aluminium cylinder (PMA-1 landmine fuse), Fig. 3.5b. The electrical conductivities of objects from the second group were measured using a Foerster SIGMATEST 2.069 device.

Table 3.2: Test dataset [119].

Object	Dimensions [mm]	Material	σ [MS/m] Declared	σ [MS/m] Meas	No. of exp.
Ball 1	D=5	AISI 316	1.3		10
Ball 2	D=5	Al1050	36		10
Ball 3	D=5	CuZn35	14		10
Ball 4	D=8	AISI 316	1.3		10
Ball 5	D=8	Al1050	36		10
Ball 6	D=8	CuZn35	14		10
Cuboid 1	24x10x5	Cu		58	10
Cuboid 2	20x10x2	CuZn		14	10
Cuboid 3	20x9x5	Al		30	10
PMA-1	L=10, D=6	Al		26	10
Total					**100**

3.3.4   Dataset construction and measurements

Simulation setup

Each object, Fig. 3.5b, was modelled by combining primitives using NetGen's Constructive Solid Geometry technique [129], Fig. 3.6. An outer box is defined around the object, outside of which we assume that the EM activity of the object is negligible. The recommended box dimension is about 100 times the size of the object [102]. Mesh settings and the number of snapshots are set in an iterative manner by changing the parameters until the MPT estimate converges. The frequency sweep for each simulation consists of 200 logarithmically spaced points within $\omega \in [10^1, 10^7]$ rad/s, Figs. 3.7 and 3.8. DSRF estimation of simulated FD MPT eigenvalues is done using the approach described in Section 3.3.1, equations (3.50)-(3.56). Relaxation frequencies are set to frequency sweep values, which means that model order K and the number of equations N are equal. Figs. 3.7 and 3.8 show the simulated and DSRF estimates of eigenvalues for non-spherical objects. Only the solid line is visible due to the perfect match between the DSRF representations and the simulations. Finally, to correct for finite pulse width, the procedure described in Section 3.3.1, equations (3.57)-(3.62), is then applied to the DSRF form of simulated eigenvalues. Before comparison, both measured and simulated eigenvalues are normalized (i.e., each eigenvalue is divided by the maximum value of the eigenvalue with the highest amplitude).

Spherical objects

In the first set of experiments, measurements were made on non-ferrous balls, Fig. 3.5a. As the ball has the same response from all angles, it is enough to make a measurement from a single sensor location. This means that the MPT eigenvalues of the ball are also equal (i.e., $\lambda_{11} = \lambda_{22} = \lambda_{33}$), so there is no need for inversion. The duration of each measurement was 10 s. The response of the ball was recorded for the first 5 s (with the detector placed directly above the ball), and the response in the air was recorded for the remaining 5 s. MPT eigenvalues are estimated by subtracting the average response in the air from the average response of the ball and scaling the result. Notice that only MD data are required for eigenvalue estimation.

Non-spherical objects

In the second set of experiments, measurements were made on non-symmetric objects (i.e., having three different eigenvalues) and one axisymmetric object, Fig. 3.5b. Now, the responses from different angles over the object are not the same. Thus, it is necessary to make measurements from different locations over the object and perform NLS inversion to estimate MPT, Table 3.1. For each measurement, MD was swept $1-2$ cm over the grid surface with a speed of up to 30 cm/s, following the scanning pattern within the scanning area, Fig. 3.4. MD and the corresponding coil's pose data were synchronously acquired during the measurement time of 60 s. A 7th-order median filter (MATLAB implementation) was applied to remove the measurement noise. The algorithm uses MD and coil's pose data recorded during the entire measurement. The average time required by NLS to solve (3.63) is around 3 s (PC featuring Intel Core i7-8750H CPU (2.20GHz) and 16 GB of RAM). The collected dataset is summarized in Table 3.2.

3.3.5 Results and discussion

When it comes to error metrics, the relative deviation and normalized root mean square error (NRMSE) have been previously utilized by researchers to quantify the results of MPT estimates
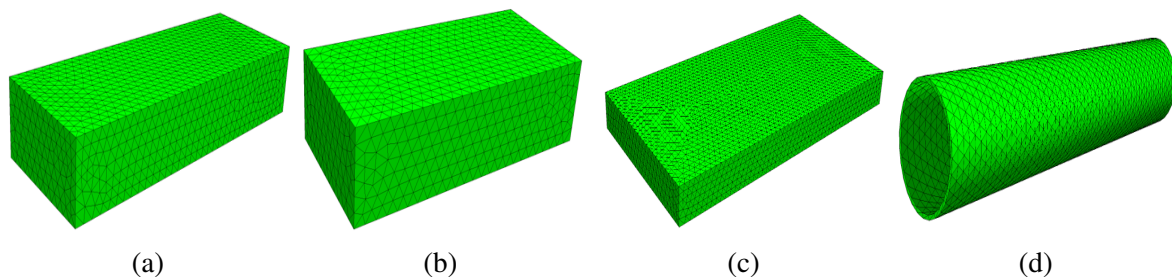

(a)   (b)   (c)   (d)

Figure 3.6: The meshes of non-spherical objects. **(a)** Copper cuboid. **(b)** Aluminium cuboid. **(c)** Brass cuboid. **(d)** PMA-1 fuse.
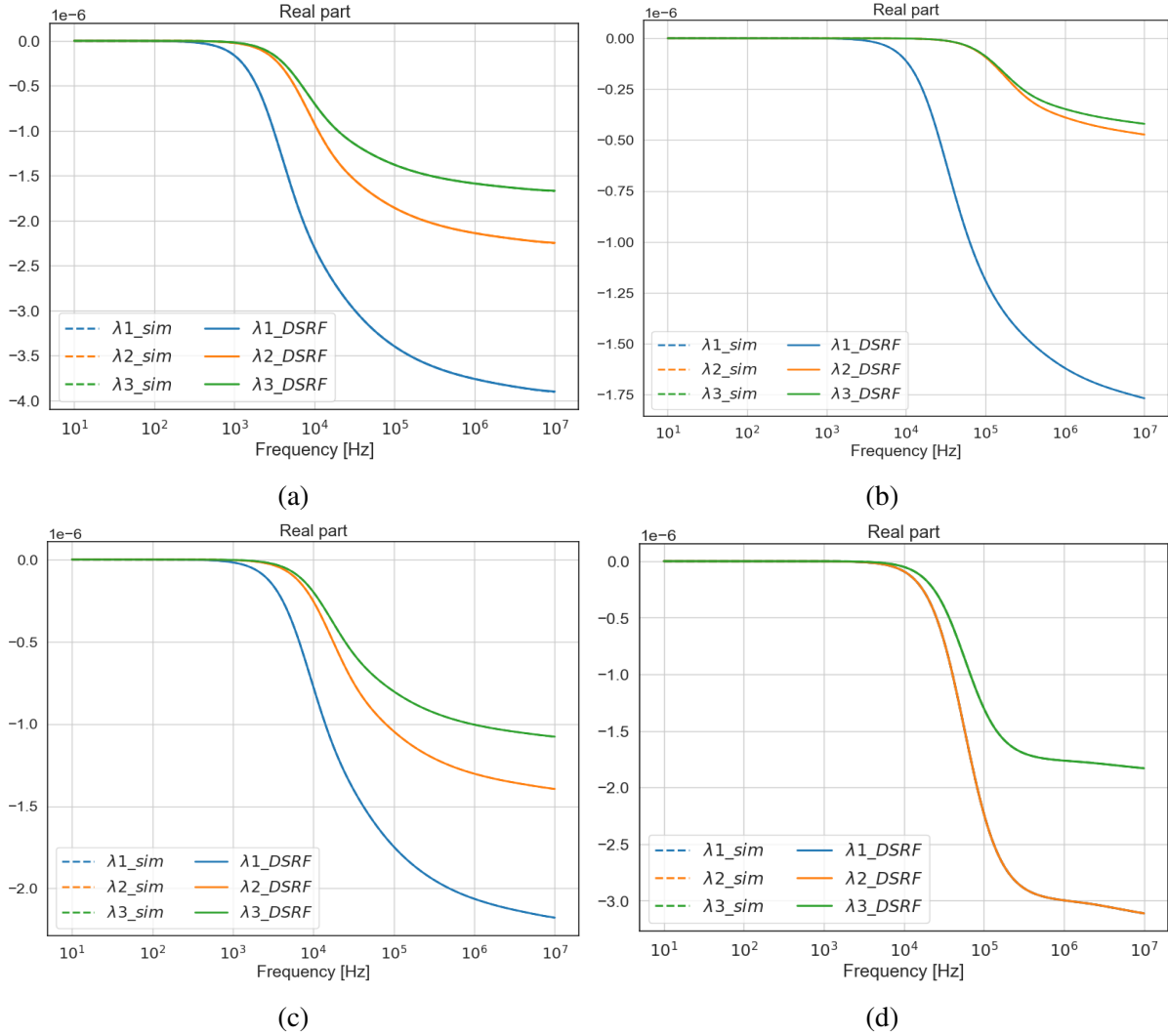
Figure 3.7: Comparison of DSRF estimates and simulated eigenvalues of non-spherical objects (real parts). **(a)** Copper cuboid. **(b)** Aluminium cuboid. **(c)** Brass cuboid. **(d)** PMA-1 fuse.

[118, 130]. In order to allow a straightforward comparison of the results, the same metric is utilized in this thesis. The NRMSE is calculated using the following expression

$$NRMSE[\%] = 100 \frac{\sqrt{\sum_{i=1}^{n} \frac{(Meas_i - Ref_i)^2}{n}}}{\overline{Ref}}, \tag{3.64}$$

where $Meas_i$ and Ref_i are measured and the reference value for each TG i, respectively. $\overline{Ref}$ is Ref average over all TGs, and n is the number of TGs. The normalization makes the NRMSE value unitless and independent of the scale of the measurements, which is useful for comparing the measurement error across different MPT eigenvalues. Due to the decaying nature of eigenvalues, NRMSE may be affected by the small values at late TGs. For this reason, only TGs with amplitudes above the threshold (set to 1% of the eigenvalue's maximum value) are considered to calculate the error.
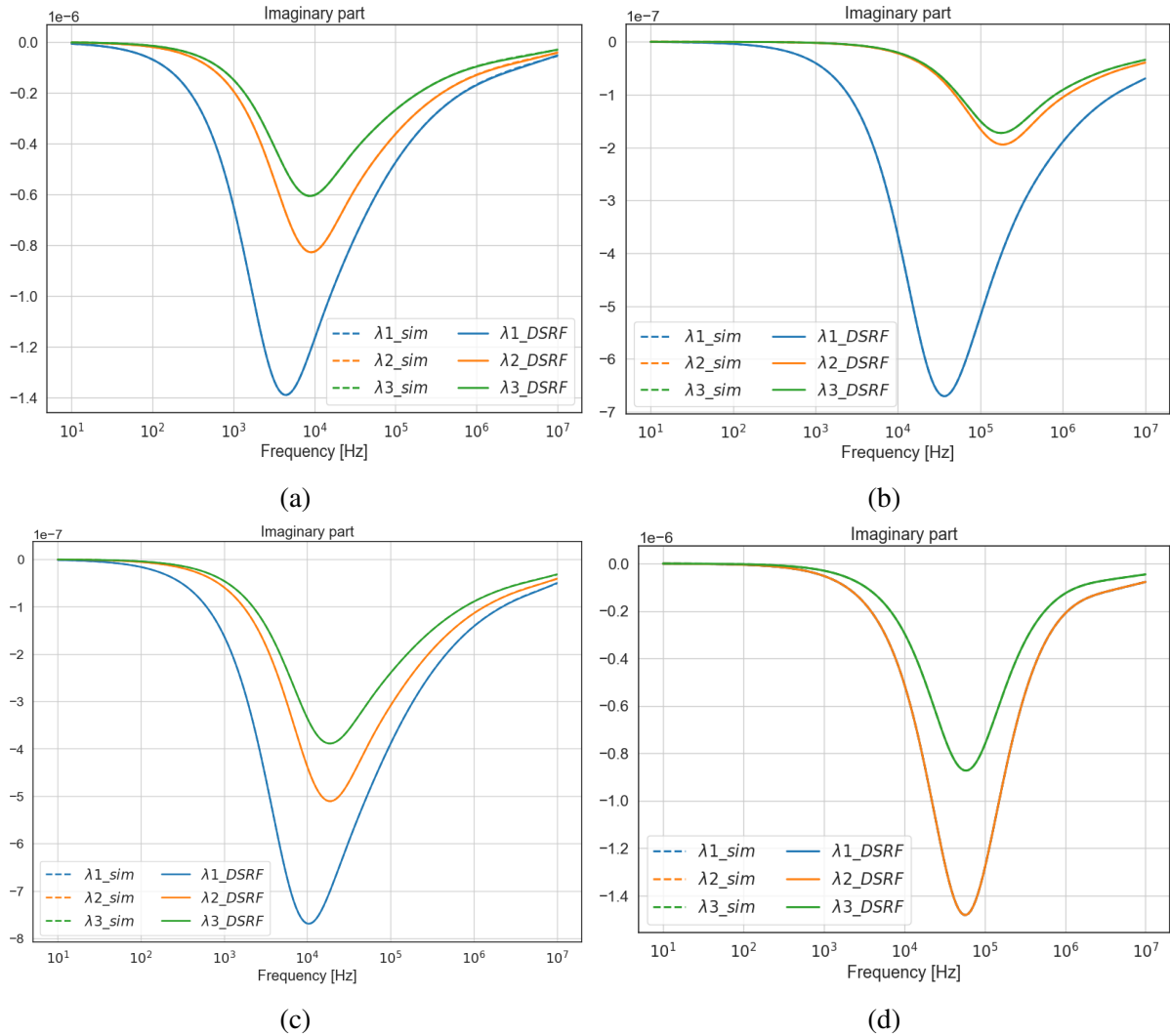
Figure 3.8: Comparison of DSRF estimates and simulated eigenvalues of non-spherical objects (imaginary parts). **(a)** Copper cuboid. **(b)** Aluminium cuboid. **(c)** Brass cuboid. **(d)** PMA-1 fuse.

MPT eigenvalues obtained from EMI data

Fig. 3.9 compares estimated MPT eigenvalues of balls with simulations. The simulations were verified by analytical solutions that exist for spherical objects [17].

Since the ball has three identical eigenvalues, each object is represented with one eigenvalue. The excellent agreement of the simulated Sim_pulse and measured Meas eigenvalues in all cases verifies the proposed FD-TD comparison methodology. A slightly larger deviation appears in the case of a 5 mm stainless steel ball, where the simulated eigenvalue decays somewhat faster, Fig 3.9c. The reason for this may be the difference between the actual and declared conductivity [128], i.e., the actual conductivity may be slightly higher.

To demonstrate how the finite width of the pulse affects the eigenvalues, the simulated eigenvalues before their correction are included, denoted as Sim_step. Looking at (3.62), note that eigenvalues with lower relaxation frequencies are more affected. Since balls with higher con-
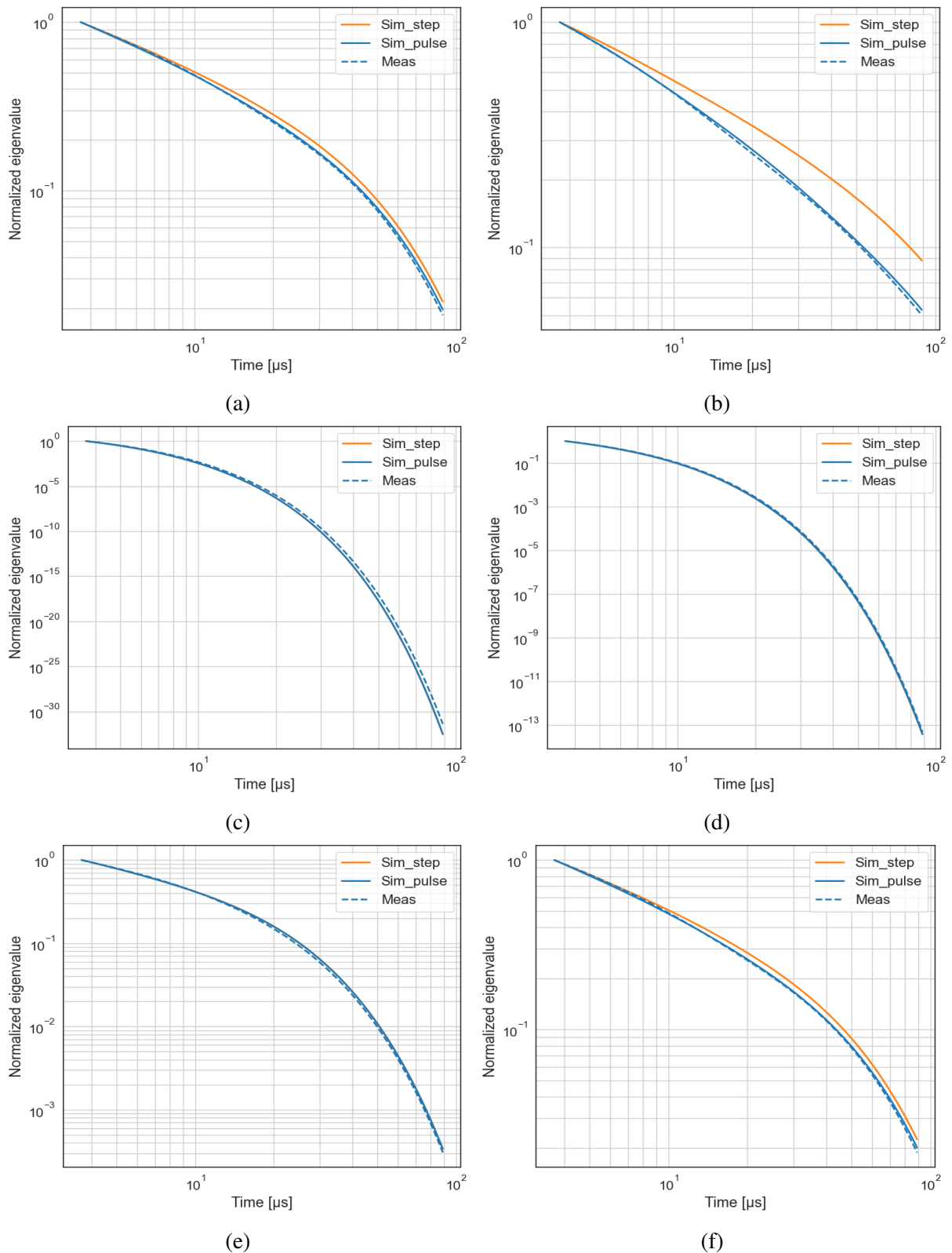
Figure 3.9: Comparison of measured and simulated eigenvalues of non-ferrous balls [119]. **(a)** 5mm aluminium. **(b)** 8mm aluminium. **(c)** 5mm stainless steel. **(d)** 8mm stainless steel. **(e)** 5mm brass. **(f)** 8mm brass.

Table 3.3: Summary statistics of MPT estimates [119]. (a) Balls. (b) Cuboids and PMA-1 fuse.

(a)

Ball	Al		AlSI		CuZn	
	5 mm	**8 mm**	**5 mm**	**8 mm**	**5 mm**	**8 mm**
NRMSE $(\overline{\text{Meas}}, \text{Sim})[\%]$	2.5	1.9	5.1	3.0	1.9	2.1

(b)

Object	NRMSE $(\overline{\text{Meas}}, \text{Sim})[\%]$			NRMSE $(\text{Meas(min/max)}, \overline{\text{Meas}})[\%]$		
	$\lambda 1$	$\lambda 2$	$\lambda 3$	$\lambda 1$	$\lambda 2$	$\lambda 3$
Cuboid Cu	3.4	3.7	13.4	0.2/0.2	3.8/3.4	4.0/3.8
Cuboid CuZn	3.2	5.9	8.0	0.2/0.2	5.0/5.4	3.7/4.7
Cuboid Al	3.5	7.4	10.0	0.3/0.5	4.2/4.2	4.4/5.0
PMA-1 fuse	1.0	12.4	9.8	0.6/0.5	4.2/3.2	4.3/4.3

ductivity and size have lower relaxation frequencies [34], their eigenvalues are more distorted. This is consistent with the results, as the largest deviation between Sim_step and Meas is apparent in the case of an aluminium 8 mm ball, Fig. 3.9b. The relaxation frequencies of stainless steel and 5 mm brass balls are relatively high, so the influence of the pulse width is negligible, Fig. 3.9c-e.

Table 3.3a shows NRMSE values comparing average eigenvalue estimates $\overline{\text{Meas}}$ of each ball with the simulations Sim. The average is calculated over ten consecutive measurements. Due to the deterministic nature of the measurement procedure, the deviations between the average and the individual estimates were negligible.

MPT eigenvalues inverted from position-referenced EMI data

Fig. 3.10 compares estimated and simulated eigenvalues of non-symmetric objects, Fig. 3.5b. The results again show very good agreement between estimates and simulations. NRMSE values (for each eigenvalue $\lambda 1 \geq \lambda 2 \geq \lambda 3$) comparing average measurement $\overline{\text{Meas}}$ (over ten consecutive measurements) with the simulation Sim are given in the first column of Table 3.3b. In all cases, $\lambda 1$ shows the best agreement with the simulation, with NRMSE values within 3.5%. The estimation of $\lambda 2$ also shows good agreement with the simulations in the case of cuboids, Fig. 3.10a-c, while it shows slightly higher NRMSE values for the PMA1 fuse, Fig. 3.10d.
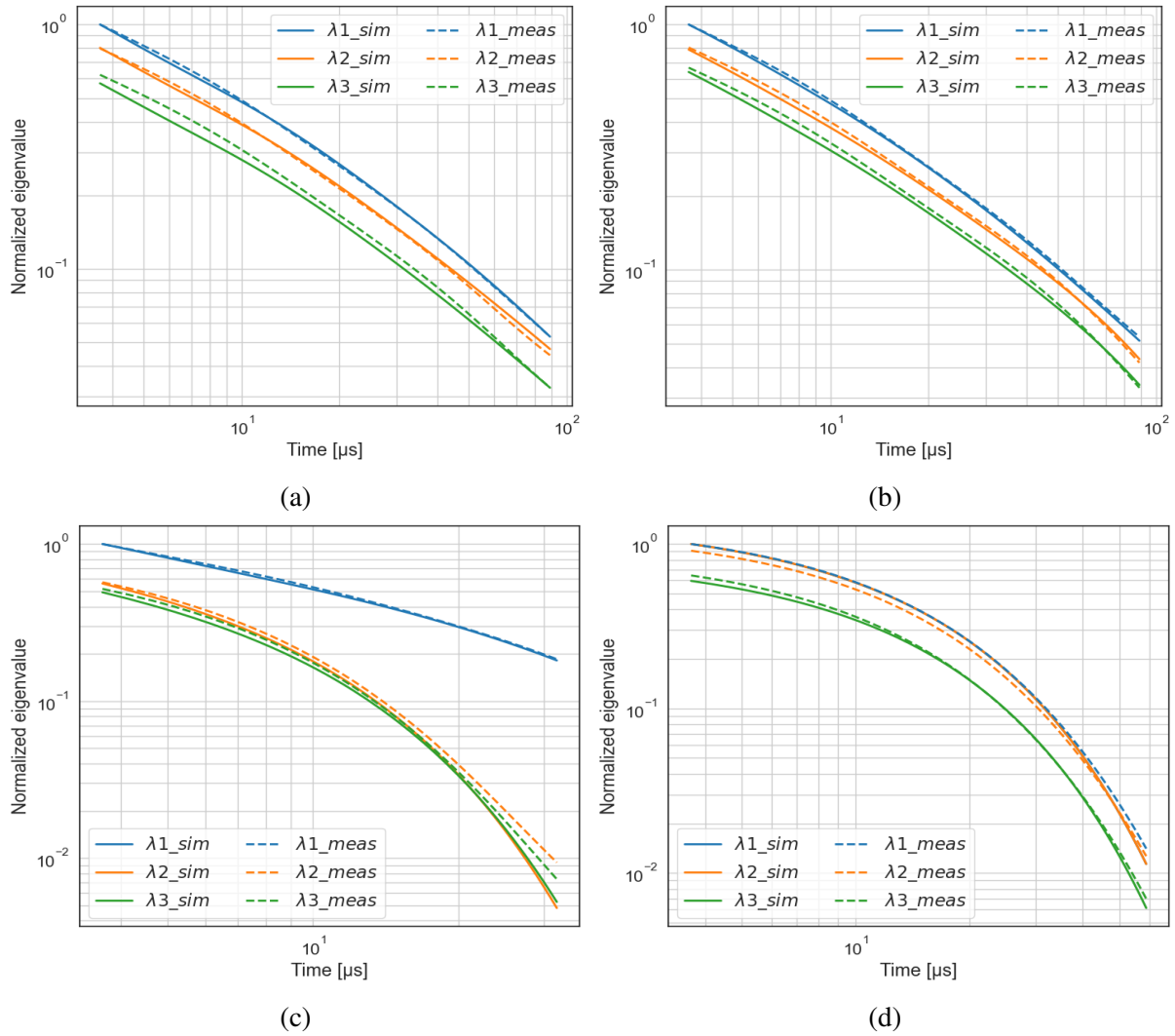
Figure 3.10: Comparison of measured and simulated eigenvalues of non-spherical objects [119]. **(a)** Copper cuboid. **(b)** Aluminium cuboid. **(c)** Brass cuboid. **(d)** PMA-1 fuse.

Although the PMA1 is a hollow cylinder (i.e., has two identical eigenvalues), there is a small difference between the measurements of $\lambda 1$ and $\lambda 2$. However, the PMA1 used for the experiments is not a perfect cylinder (i.e., it has slight surface imperfections due to frequent handling), which may have caused this error, Fig. 3.5b. A somewhat larger difference between measurements and simulations can be seen in the case of $\lambda 3$, Table 3.3b. This is not surprising, given that it has the lowest amplitude among the eigenvalues (i.e., smallest contribution to EMI response). This means that small deviations in estimated $\lambda 3$ will have a negligible effect on the objective function error (3.63). Analogously, we can observe increased errors for $\lambda 2$ and $\lambda 3$ in the late TGs, Fig. 3.10c.

Due to uncertainties associated with the experimental procedure (e.g., scan pattern, scan speed, inversion procedure) and measurements (e.g., search head tracking error, MD noise and drift), eigenvalue estimates may vary. For this reason, in the second column of Table 3.3b, we present estimation repeatability by comparing minimum or maximum eigenvalue Meas(min/max)

with the average $\overline{\text{Meas}}$. NRMSE within 5.4% for all cases verifies that the eigenvalue estimate is robust to measurement uncertainties. This implies that the scanning area within $\sim 50 \times 60$ cm, Fig. 3.4, is sufficient to record responses from different object angles, and the EM tracking system provides accurate MD coil's poses within this area. Furthermore, the scanning speed of up to 30 cm/s ensures spatial resolution high enough to capture rather subtle changes in EMI data response, while the 7-th order median filter efficiently removes MD data noise. The eigenvalues are estimated along with the orientation and location of the object (3.63). The NLS algorithm yields absolute errors < 3 mm and $< 5°$ for estimated locations and orientations, respectively.

State-of-the-art systems developed for MPT measurement mostly operate in FD and involve complex laboratory setups [117, 118, 130]. On the other hand, the presented system operates in TD and is suitable for the field application. To summarize, the above study yields the following contributions:

- Firstly, a novel methodology to compare numerically or analytically derived MPTs in FD with their TD equivalents obtained by inverting measured EMI data was established.
- Secondly, it is demonstrated that TD MPT of non-ferrous arbitrarily shaped objects can be reliably obtained by using a portable system based on pulsed induction MD and EM tracking system.

The results suggest that the proposed system has enormous potential to be combined with discrimination algorithms trained on a comprehensive library of simulated MPTs for hidden metallic object detection. Chapter V discusses the system's further development involving the integration of the simulation-based machine learning model and performance demonstration on real targets.

To simplify the above study, the measurements were collected for the objects placed at a fixed depth, i.e., $z_{obj} \approx -5$ cm. On the other hand, IMAS standards require clearance of all metallic objects from the surface down to 13 cm in depth. Therefore, it is necessary to verify the system performance (at least) within the required depth range. In general, errors in estimated location will reflect on the estimated eigenvalues. The next chapter demonstrates the limitations of the inversion-based method (3.1) related to object localization and presents an alternative, ML-based approach to deal with the depth estimation problem.

Chapter 4

Object Depth Estimation From Position-Referenced EMI Data Using Machine Learning

This chapter is based on the following publications:

- •M. Šimi ć, D. Ambruš and V. Bilas, "Rapid Object Depth Estimation From Position-Referenced EMI Data Using Machine Learning," in IEEE Sensors Journal, vol. 23, no. 4, pp. 4285-4293, 15 Feb.15, 2023.
  © IEEE
- •M. Šimi ć, D. Ambruš and V. Bilas, "Object Depth Estimation From Line-Scan EMI Data Using Machine Learning," 2022 IEEE Sensors, Dallas, TX, USA, 2022, pp. 1-4.
  © IEEE

As discussed in the previous chapter, feature extraction (3.1) is treated as part of nonlinear dipole inversion involving the estimation of the object's intrinsic parameters, as well as the object's location and orientation. In the case of single-receiver sensors used in conventional MD designs, a recent study showed that most difficulties with the inversion process come from depth estimation [42]. Improvements over the NLS approach (3.1) are possible by employing the differential evolution method [42]. However, this comes with the price of higher computational complexity, which may limit its application on resource-constrained MD devices.

The study presented in this chapter is based on the idea that the initial problem can be separated into two parts: the depth estimation and the estimation of other dipole model parameters. In this approach, depth estimation is treated as an isolated problem. Specifically, this chapter introduces a method based on ML for rapid estimation of metallic object depth from line-scan MD data. Knowing the object's depth or restricting the bounds of its search space would significantly facilitate (in terms of speed and accuracy) the feature extraction procedure (3.1).

4.1   Existing approaches to depth estimation

Different approaches for EMI-based depth estimation based on simple (often linear) modelling have been proposed. Das *et al.* analysed how different depths affect the spatial response of a metallic object using the TD MD [131]. In his later work, he investigated the correlation between an object's depth and the FWHM response [126]. The model for depth estimation, which assumes a linear relationship between FWHM and depth, was proposed in [132]. However, the analysis showed that FWHM cannot be used as an unambiguous indicator of depth even for known objects, reinforcing the need for a more reliable solution [126, 132]. An interesting approach based on the forward model (3.44) was proposed in [133]. The depth is obtained using the explicit expression, which requires the maximal spatial responses (at least two) at different heights above the target and the corresponding height difference. Abeynayake *et al.* developed a linear model for depth estimation using the ratio of the responses recorded by different coil configurations [134]. However, the estimation requires a priori knowledge of the object type. Therefore, object type classification has to be performed in advance to choose an appropriate model. In [135], the authors analysed a correlation of the phase information of the object frequency-domain response with the object's depth. In general, shallow objects provide stronger high-frequency signals, while deep objects provide stronger low-frequency signals [135, 136]. Using the MD in gradiometric mode, Marble *et al.* proposed two different approaches [137]. The first performs a linear estimation of the object depth using a normalized vertical magnetic field gradient. The second approach performs a binary classification of objects that are either shallow or deep. In their later work, authors developed four different algorithms for depth estimation, each associated with a different sensor technology [138]. Recently, Lijie *et al.* proposed

an approach that takes advantage of multiple receiver MD to calculate an object's depth from the magnetic field and its spatial gradient tensor [139].

Various library-based approaches involving the signal-matching technique have been proposed. Kanenko *et al.* used the 3D representation of MD's response to extract one of the four types of characteristic curves, each represented by polynomials [140]. Continuous depth estimation is obtained by interpolating the database data. In [141], the authors proposed an object localization method for wideband EMI data using the low-rank model-based dictionary. Singular value decomposition is used together with a dictionary-matching technique to obtain an object's location. Another interesting method based on the orthogonal matching pursuit was proposed in [142]. A database of EMI responses for simple canonical objects (sphere, wire loop) was created assuming dipole model approximation. However, the performance of the algorithm significantly deteriorates when the object poorly matches the model used in the library. Freese *et al.* based their depth estimation method on the assumption that the normalized spatial responses of MD are relatively similar for a variety of metallic objects at a given depth [31].

In general, the performance of the above methods is compromised in the case of arbitrarily oriented objects or when the material/shape properties of the object are significantly different from those stored in the database. The forthcoming sections present an ML-based approach for depth estimation that aims to overcome these limitations. To contextualize the results, the performance of the proposed approach is compared with the depth estimates obtained using NLS inversion method. Experimental evaluation was performed under laboratory conditions on a large dataset containing arbitrarily oriented objects of different sizes, shapes, and materials.

4.2   Reference Method: NLS Approach

Object depth, among other parameters, is estimated by finding the solution to

$$\underset{\mathbf{M}_v, \mathbf{r}_{object}}{\text{argmin}} \left(||\mathbf{u}_{meas} - \mathbf{f}_{FWD}(\mathbf{r}_{object}, \mathbf{M}_v)||^2 \right), \tag{4.1}$$

where $\mathbf{u}_{meas}$ represents measurements collected at different positions of the MD and $\mathbf{f}_{FWD}$ is given by (3.46). The forward model is linear with respect to $\mathbf{M}_v$ and nonlinear with respect to the object's location $\mathbf{r}_{object}$. A pseudo-code of the NLS inversion algorithm (implemented in MATLAB) is given in Table 4.1.

The optimization problem (4.1) is essentially the same as (3.63); therefore, the algorithmic procedure (4.1) is similar to that discussed in Section 3.3.2, (3.1). Here, the forward model in the form (3.46) instead of (3.49) is used as we are interested in the estimated object's location (i.e., depth), rather than its eigenvalues and orientation. Another difference concerns the depth solution range, modified to ensure a fair comparison with the proposed approach, which uses

Table 4.1: Pseudo-code of NLS inversion [127].

Initial guess for object location:
$$\mathbf{r}_{obj\_init}(x,y) = \underset{x,y}{\mathrm{argmax}}(\mathbf{u}_{meas}(\mathbf{r}_{sensor}))$$
$$\mathbf{r}_{obj\_init}(z) = FWHM(\mathbf{u}_{meas})$$

Initialization of magnetic polarizability:
$$\mathbf{M}_{v\_init} = \boldsymbol{S}^{\dagger}(\mathbf{r}_{obj\_init})\mathbf{u}_{meas}, \mathbf{M}_v \geq 0$$

Find solution to the nonlinear least squares problem:
$$\underset{\mathbf{M}_v, \mathbf{r}_{obj}}{\mathrm{argmin}}\left(||\mathbf{u}_{meas} - \mathbf{f}_{FWD}||^2\right), \begin{cases} \mathbf{M}_v \geq 0 \\ -2.5 < \mathbf{r}_{obj}(z) < -15 \end{cases}$$

Extract object depth:
$$obj\_depth = \mathbf{r}_{obj}(z)$$

---

the same range (elaborated in the following section).

4.3 Machine learning-based approach

4.3.1 Intuition

Given the intrinsic and extrinsic parameters of the object, the responses recorded during a single pass of the MD over the object, hereafter referred to as a line-scan, can be calculated using (3.46). A line-scan is a linear combination of sensitivity patterns ($\mathbf{S}_{xx}, \mathbf{S}_{xy}, ..., \mathbf{S}_{zz}$), (3.47), weighted by their corresponding directional polarizabilities ($\mathbf{M}_{xx}, \mathbf{M}_{xy}, ..., \mathbf{M}_{zz}$), (3.48). Looking at (3.46)-(3.48), it can be observed that location (i.e., depth) information is contained in the sensitivity patterns. Sensitivity patterns are always the same for the same coil geometry and at the same object location, regardless of orientation and type of the object. Fig. 4.1 shows the sensitivity patterns of a line-scan for objects placed at different depths (i.e., the sensitivity profiles). We can notice that smaller depths are characterized by larger gradients (colour changes are more pronounced), a property that can be exploited to infer an object's depth. This is where the convolutional neural network (CNN) comes into play, taking advantage of convolutional layers to extract these spatial features from line-scan data related to the sensitivity patterns [143]. Once features are extracted, depth estimation can be done using traditional ML models (e.g., SVM, RF, decision trees) or feedforward neural networks. By making the kernel smaller than the input, CNNs can have several orders of magnitude fewer weights than traditional neural networks [143, 144]. This reduces memory requirements and computation time, making them suitable for practical applications.
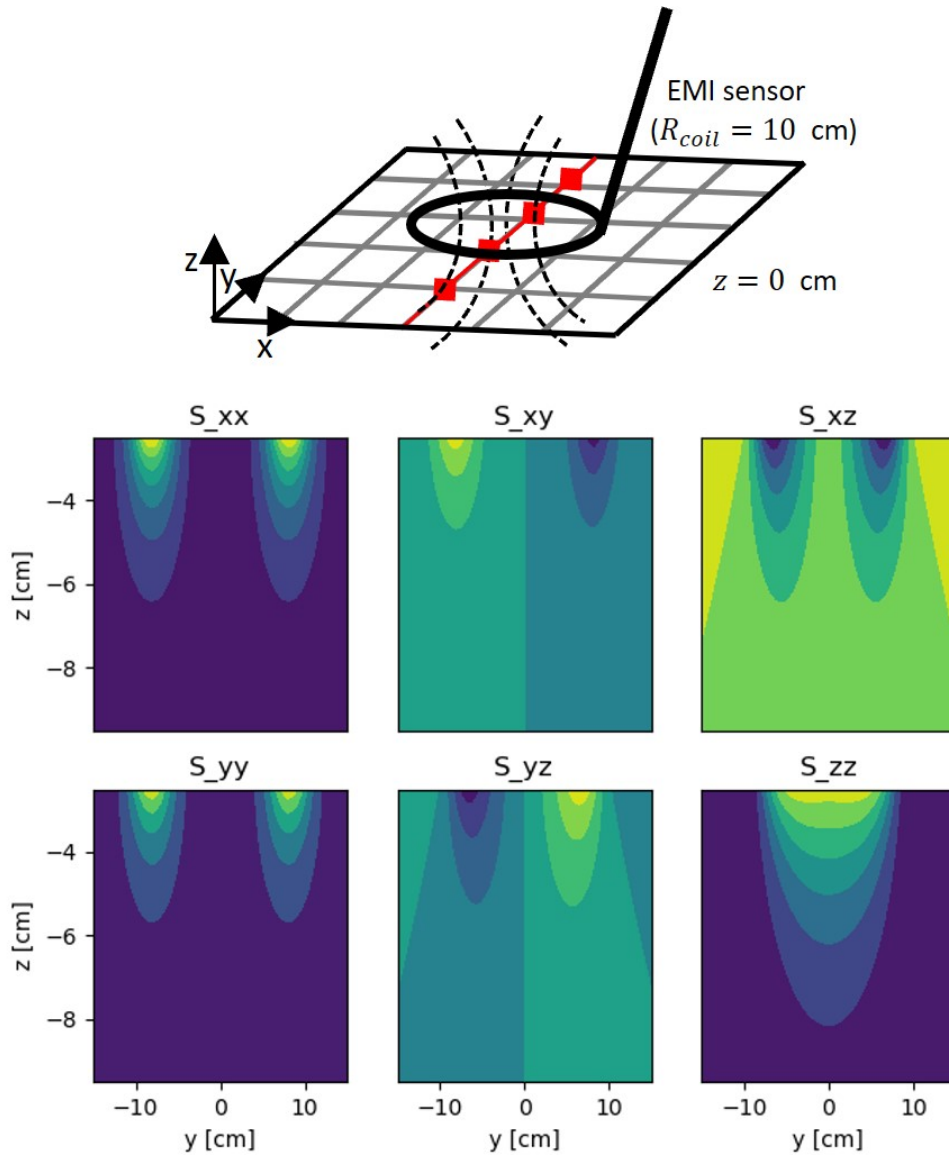
Figure 4.1: Sensitivity profiles: the normalized sensitivity patterns of a line-scan calculated for objects placed at different depths [127].

4.3.2   Building the dataset

In the proposed approach, instances of the training dataset were generated using (3.46). As discussed in the previous chapter, equation (3.46) assumes magnetic dipole approximation, which allows us to represent each object by induced (triaxial) magnetic dipole. If we restrict the analysis to a single TG, an arbitrary object (regardless of the shape, size, and material properties) is characterized by six elements, i.e., three orientations and three eigenvalues, Fig. 4.2. The main idea is to generate the training dataset involving a comprehensive range of orientations and eigenvalues at each depth so the CNN model can learn to ignore these effects and focus on sensitivity patterns for decision-making. As there are infinite possible combinations, dataset construction requires some simplifications.

The first simplification refers to the min-max normalization. By scaling the range of sim-
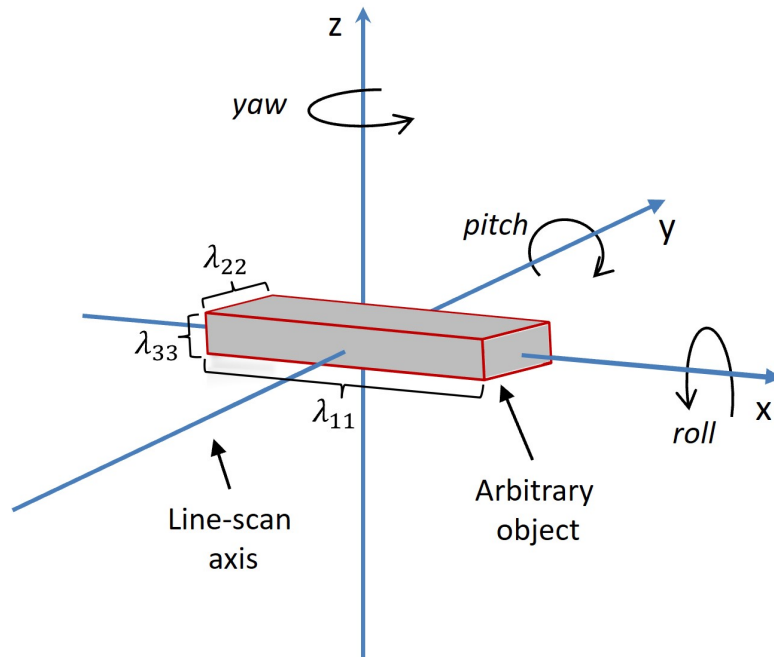
Figure 4.2: The object represented as a triaxial magnetic dipole. Each object's dimension is defined by the corresponding eigenvalue magnitude (cuboid representation is for illustrative purposes; in reality, the dipole is a point source (i.e., dimensionless)).

ulated line-scans, we bypass the object size modelling and make the calibration constant k irrelevant.

The $\mathbf{M}_v$ is a function of the object's orientation and intrinsic features. Normalization discards the information related to the size of the object; however, it is still necessary to account for different object geometries and materials. Because of normalization, we only need to include the eigenvalue ($\lambda_{11,22,33}$) ratios and not their absolute values. This can be done by modelling the ratios with respect to only one of the eigenvalues, followed by rotation of the dipole's principal axes to cover (approximately) all possible scenarios. A pool of eigenvalues is created by fixing the first eigenvalue, λ_{11}, to 1, while the other two, λ_{22} and λ_{33}, are varied through all possible combinations drawn from the set $\{0.2, 0.4, 0.6, 0.8, 1\}$. This makes 25 different combinations in total.

Including different orientations in the modelling significantly impacts the dataset's size, which is proportional to the third power of the predefined angle values (assuming the same number of values is used for each angle). Fortunately, the range of relevant object orientations can be significantly reduced by exploiting the symmetric nature of the induced magnetic dipole and line-scan geometry, Fig. 4.2. Firstly, the responses due to the induced dipole (i.e., line-scan) remain the same if the dipole is rotated by $180°$ about its principal axes. This reduces relevant angle ranges from $360°$ to $180°$. Furthermore, line-scans remain the same if the dipole is mirrored with respect to the $y - z$ plane. This further reduces the relevant *yaw* angle range to $90°$. Finally, note that for each combination of eigenvalues (e.g., $\lambda_{11} = 1$, $\lambda_{22} = 0.6$, $\lambda_{33} = 0.2$),

there exists the combination with the λ_{22} and λ_{33} values swapped (i.e., $\lambda_{11} = 1$, $\lambda_{22} = 0.2$, $\lambda_{33} = 0.6$). Swapping the values of λ_{22} and λ_{33} is essentially the same as rotating the dipole by $90°$ in *roll* direction. Consequently, the relevant *roll* angle range reduces from $180°$ to $90°$. Taking everything into consideration, the angles were set to all possible combinations of the following values: $roll, yaw \in \{0°, 22.5°, 45°, 67.5°, 90°\}$, $pitch \in \{0°, 22.5°, \ldots, 157.5°\}$. Experiments showed that a resolution of $22.5°$ is sufficient to make the CNN model (detailed in Section 4.3.3) robust to arbitrary orientations.

The **S** is a function of the MD coil geometry (which is known), line-scan trajectory (MD coil's poses), and the location of the object. All responses are calculated using the trajectory defined along the *y*-axis in the range of $y \in [-23, 23]$ cm with a step of 0.5 cm. Other trajectory parameters (coil angles; x and z -coordinates) were set to zero. Simulations were performed at 40 linearly spaced depths within $d \in (2.5, 15)$ cm, with coordinates *x* and *y* each set to 0 cm.

A training instance was generated by calculating the responses at all points on the trajectory for a given combination of depth, orientation, and eigenvalues. The input vector represents 93 points of the computed response (i.e., features), and the depth is the corresponding label. Note that the same line-scan trajectory is used for all calculations, which is not a realistic scenario. In reality, the trajectory includes tracking system errors as well as arbitrary lift-offs and inclinations that exist due to manual sideways motions with MD. Furthermore, equation (3.46) does not model MD noise or uncooperative soil response (when objects are buried in the ground). Although analysis of these effects is beyond the scope of this study, it should be recognized that they exist.

4.3.3 Depth estimation using 1D-convolutional neural network

The proposed algorithm can be divided into three parts, Fig. 4.3: line-scan preprocessing, depth estimation, and security layer.

The algorithm starts by performing wavelet denoising of the line-scan measurements, which removes the noise while preserving important features, such as spikes in the line-scan (which may occur due to rapid movement of MD). Denoising is followed by scaling and linear interpolation, resulting in an input vector of fixed size and spacing of 93 and 0.5 cm, respectively.

In the second part, a 1D-CNN with four layers is employed to extract depth-specific features from the input vector. In the first layer, an input vector is convolved with 32 filters of size 15, resulting in a feature map of dimension 79x32. The second layer is a pooling operation of size 13, which reduces the dimensions of the feature map to 6x32. Following this, the feature map is converted to a vector, completing the feature extraction part. The rest of the network is organized as a 2-layer feedforward network classifier. The third layer is a dense layer of 64 units with linear activation. The last, fourth layer is a dense layer of 17 units with a softmax activation function. At this point, depth estimation is formulated as a classification problem. There are
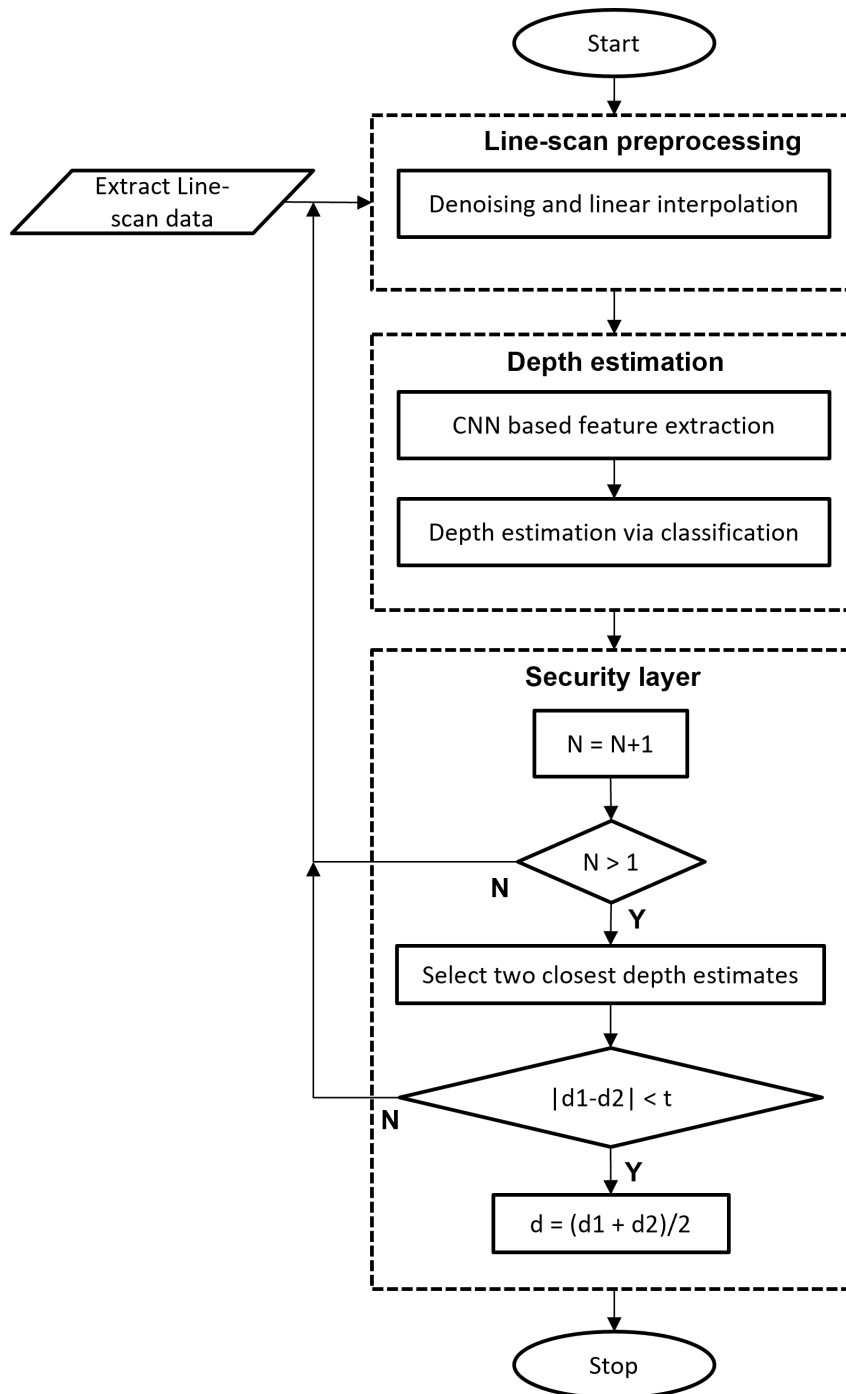
Figure 4.3: Flow chart of the proposed algorithm [127].

17 classes within $d \in [2.25, 15)$ cm, each with a depth range of 0.75 cm. For example, the first class represents depths within $d \in [2.25, 3)$ cm. The predicted depth is the weighted average of the mean depths within each class range, where the weights are the class probabilities (softmax layer output). Therefore, the predicted depth is a real number within $d \in [2.625, 14.625)$ cm.

The last part of the algorithm is the security layer. Sideways motion with MD in the air can cause significant distortions in the line-scans, leading to an erroneous depth estimate. To address this problem, an algorithm asks for an additional line-scan to confirm the depth estimate.

If the confirmation estimate significantly differs from the initial estimate, the algorithm asks for a continuation until two estimates appear close enough, i.e., within a predefined threshold. The final depth estimate is the mean value of the two closest estimates. This means that depth estimation requires at least 2 line-scans. Reducing the threshold, the performance is increased at the cost of a longer depth estimation time. In the current version of the algorithm, the threshold is set at 3 cm. For this threshold, the first two line-scans are used in about 85% of cases.

The CNN hyperparameters (e.g., the number of layers, the number of filters in the convolutional layer, and the size of the filters) are determined using a grid search approach. For the CNN training, the dataset of 200,000 line-scans (145 Mb) created by the simulations is used. The training dataset consists of 90% of the data, and the remaining 10% of the data is used for validation. The selected model is the one that minimizes the loss on the validation set in the first 40 epochs (i.e., complete runs over the training dataset). Training on a standard PC featuring an Intel Core i7-8750H CPU (2.20 GHz) and 16 GB of RAM (Python implementation, Keras with TensorFlow backend [145]) takes about 6 minutes. Once trained, the CNN model requires only 198 kB of memory to store its weights.

4.4 Experimental validation

A physical implementation of the measurement setup, consisting of handheld MD and EM tracking system is given in Fig. 4.4.

4.4.1 Experimental setup

The object's depth is the vertical distance between the object's centre and the grid's surface. The horizontal offset of the object from the origin is within ± 1 cm. Measurements are made under laboratory conditions at depths within $d \in (2.5, 15)$ cm. A total of 6 objects differing in shape, size, and material properties, Table 4.2, were manually placed under the grid using boards, Fig. 3.4. At all depths, the objects were placed in 6 different orientations (except for the ball), including those aligned with $x-$, $y-$, and $z-$axes, as well as objects oriented randomly ($angle \in (0°, 90°)$) in pitch, roll and yaw directions. The objects were not aligned with the orientations used to build the training dataset. Details about the MD and EM tracking system used in the experiments are given in Section 3.3.3.

4.4.2 Dataset construction and processing

For each combination of object, depth, and orientation, MD was manually swept over the scanning area for 45 seconds, Fig. 3.4.
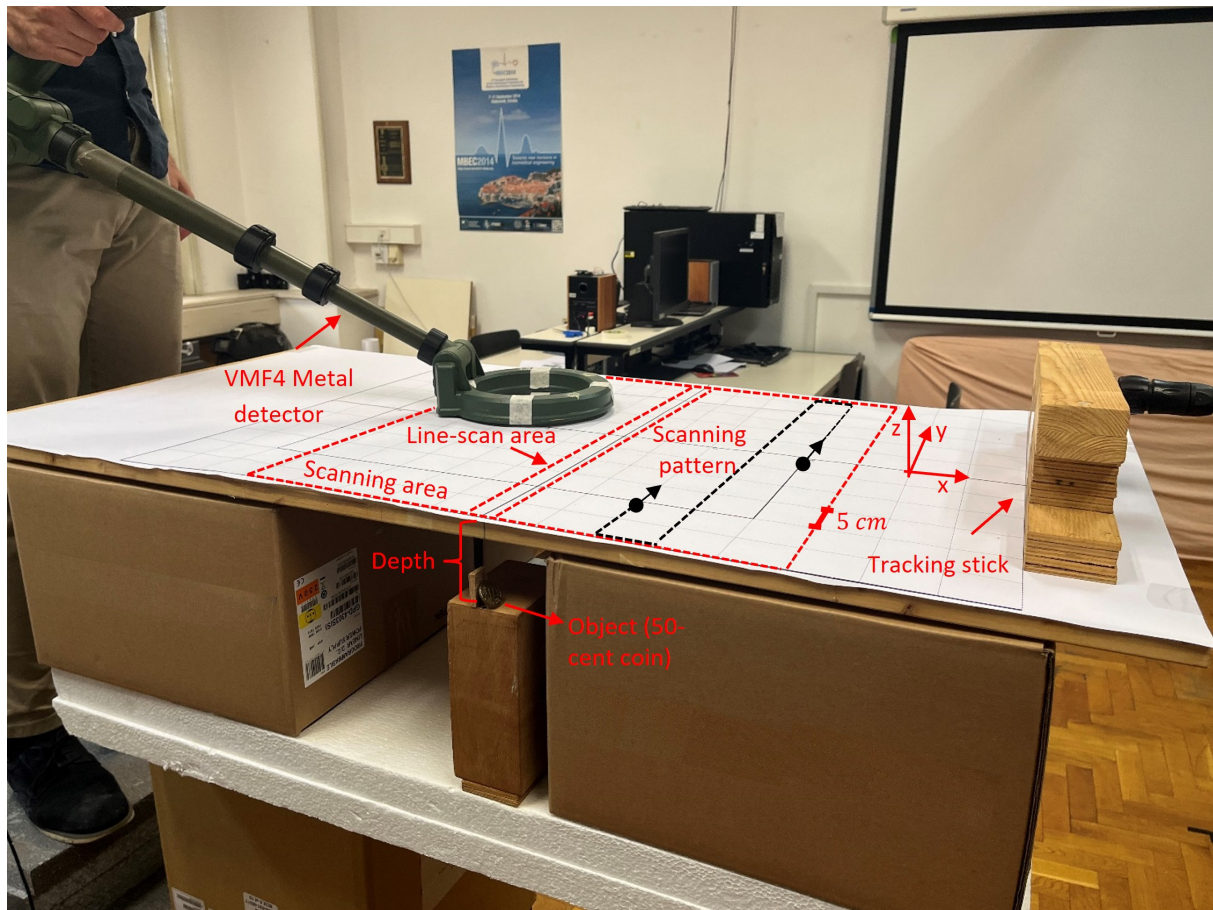
Figure 4.4: Eperimental setup (Fig. adapted from [127]).

In the first measurement phase (takes 10 seconds on average), MD was swept $1-3$ cm above the grid surface along the $y-$axis (i.e., line-scan area, Fig. 3.4) while line-scans were extracted within $y \in [-23, 23]$ cm. For each line-scan, depth estimation is performed using the proposed algorithm, Fig. 4.6. The estimated depth is corrected by subtracting the average height of the coil (for the corresponding line-scan) from the predicted depth. As discussed, the VMF4 MD samples data at 97 TGs along the pulse decay curve [32]. To improve noise performance and obtain better data diversity, line-scans from multiple TGs are utilized. However, only those at TGs with SNR greater than 25 dB are used, while the others are discarded. The final prediction is obtained by averaging the depth estimates of all TGs.

After the algorithm signals that the estimation is finished (by changing the lamp state in the MATLAB application), the second phase of the measurement starts, which involves MD sideways motions (according to the scanning pattern, Fig. 3.4) over the rest of the scanning area. The NLS inversion algorithm for depth estimation uses MD and coil's pose data recorded during the entire measurement (i.e., 45 seconds), Table 4.1. A summary of the collected dataset is given in Table 4.2.

Table 4.2: Test dataset [127].

Objects	Shape (Length (L), Diameter (D) [mm])	Material	Experiments
Ball	Sphere (D=12)	Steel	20
Bootle cap	Crown cap (L=6, D=30)	Steel alloy	60
PMA-1 fuse	Hollow cylinder (L=43, D=7)	Aluminium	66
PMA-2 fuse	Hollow cylinder (L=10, D=6)	Aluminium	42
Coin (50-cent)	Solid cylinder (L=4, D=30)	Nordic Gold	60
Cylinder	Solid cylinder (L=30, D=2.5)	Steel	66
Total			**314**

4.5 Results and discussion

The proposed CNN-based method and NLS inversion were tested on a dataset obtained as described in Section 4.3. The CNN was trained on a simulated dataset, and the results shown are the average performance over ten runs (due to the stochastic nature of the training procedure). The performances of both methods are summarized using box plots, Fig. 4.5. Each box describes the distribution of the data with five numbers: minimum value (lower limit), first quartile (Q1) or bottom edge of the box, median, third quartile (Q3) or top edge of the box, and maximum value (upper limit). A line across the box represents the median; the distance between Q1 and Q3 specifies the spread of data (interquartile range (IQR)), while the limits are drawn to the last point within 1.5 times the IQR below Q1 and above Q3. Values outside the limits are considered outliers (diamond shape). Summary statistics of the absolute errors are shown in three depth regions, referred to as shallow ($d \in (2.5, 5)$ cm), medium ($d \in [5, 10)$ cm), and deep ($d \in [10, 15]$ cm), Fig. 4.6. A relatively small amount of data per region can lead to skewed distributions (i.e., when the median is not in the middle of the box, Fig. 4.6). We use the median as it is generally the preferred measure of central tendency for skewed distributions (e.g., compared to the mean).

Fig. 4.6a and Fig. 4.6b compare the performance of the methods tested on hollow non-magnetic cylinders. Due to the low SNR at greater depths, the PMA-2 fuse measurements were
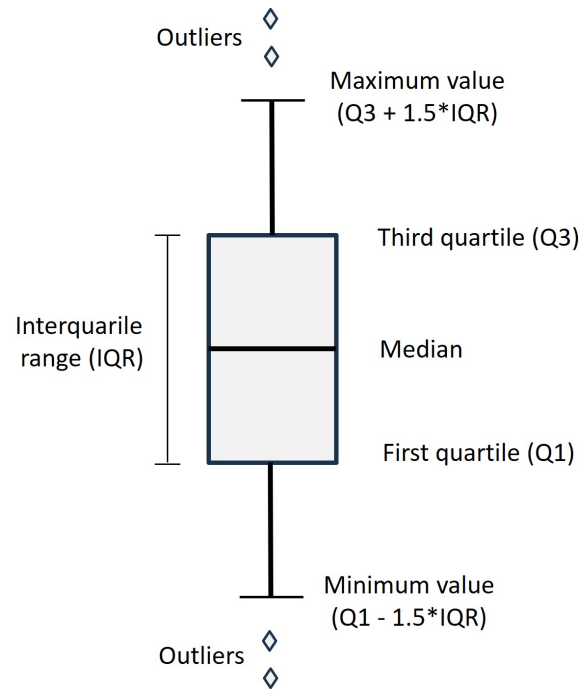
Figure 4.5: Box plot.

made only in the shallow and medium regions. The NLS has a more pronounced growth of median absolute error (MedAE) with increasing depth in both cases, while the CNN has a more pronounced growth of IQR for the PMA-1 fuse. Nonetheless, both algorithms perform well at all depths with MedAE < 11.4 mm.

Depth estimation errors for plate-like objects that are magnetic (bottle cap) and non-magnetic (50-cent coin) are shown in Fig. 4.6c and Fig. 4.6d, respectively. The algorithms achieve similar results in shallow and medium regions with a MedAE < 6 mm. However, the CNN outperforms the NLS in the deep region, with lower MedAE and IQR in both cases. This is particularly pronounced in the non-magnetic coin case, for which NLS achieves the worst performance in the test dataset (MedAE = 43.4 mm, IQR = 35.5 mm).

When it comes to magnetic cylinder and ball (Fig. 4.6e and Fig. 4.6f), the CNN shows the most notable improvement over the NLS at greater depths in terms of MedAE and IQR. Specifically, the maximum error of the CNN is lower than MedAE of the NLS in both cases.

Summary statistics of depth estimation error on the test dataset in shallow/medium and deep regions are given in Table 4.3a and Table 4.3b, respectively. In general, the results suggest that both algorithms perform well in the shallow and medium regions, while CNN performs significantly better in the deep region. This is not surprising since, at greater depths (where SNR is lower), a strong correlation between the intrinsic parameters of the object and its depth comes to the fore. Hence, the NLS algorithm has a greater chance of finding a sub-optimal solution, Table 4.1. Typically, the CNN algorithm uses data from only two passes of the MD over the object (i.e., 10 seconds on average), while the NLS uses much more (45 seconds). In
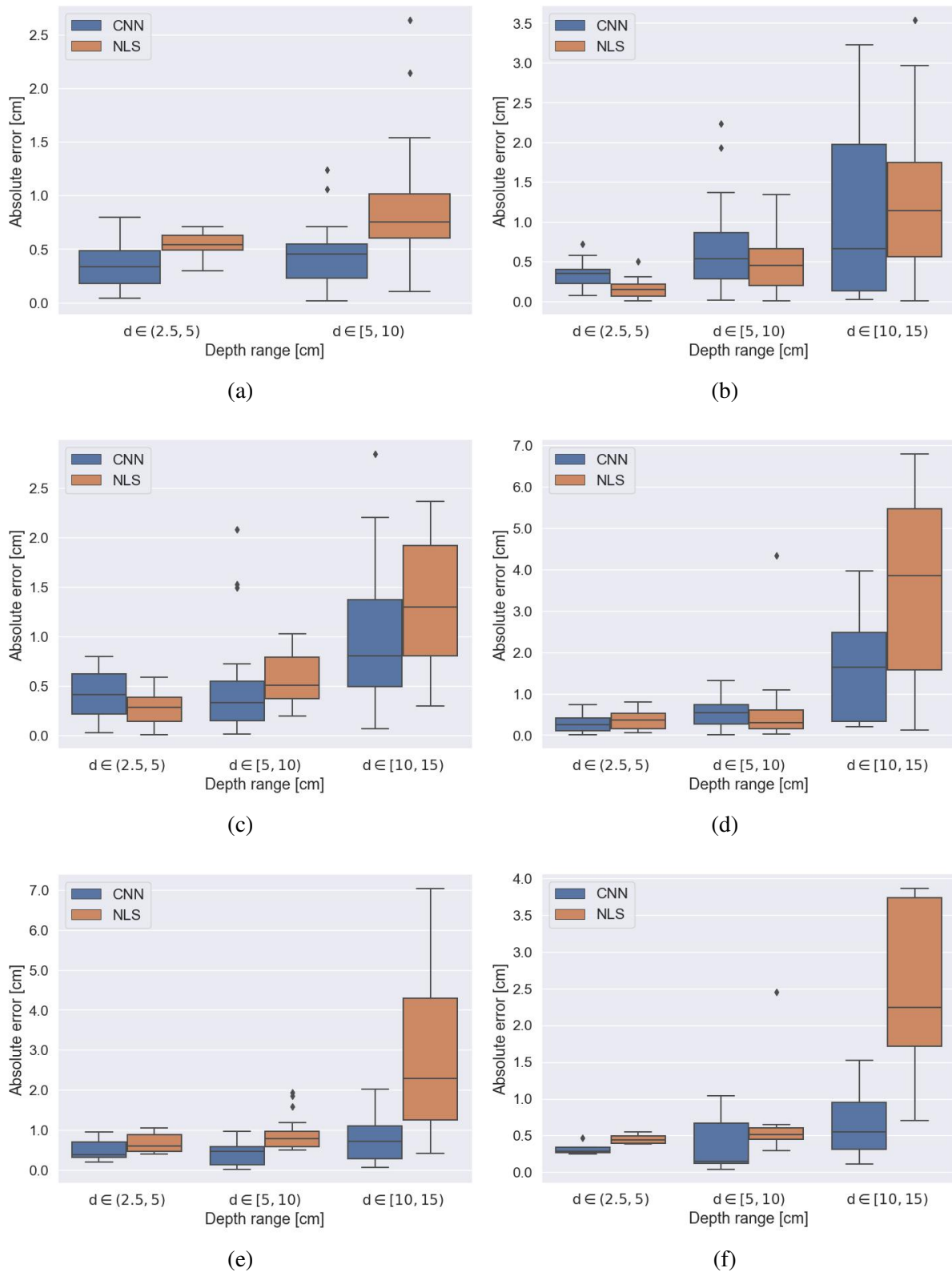
Figure 4.6: Object depth estimation obtained by the proposed CNN-based and reference NLS method [127]. (a) PMA-2 fuse. (b) PMA-1 fuse. (c) Bottle cap. (d) 50-cent coin. (e) Cylinder. (f) Ball.

Table 4.3: Summary statistics of depth estimation [127]. (a) Shallow and medium regions. (b) Deep region.

(a)

Objects	MedAE [mm]		IQR [mm]		Max error [mm]	
	NLS	CNN	NLS	CNN	NLS	CNN
Ball	4.9	2.6	1.4	3.5	24.5	10.1
Bottle cap	3.9	3.3	4.0	4.1	8.6	20.8
PMA-1 fuse	2.5	3.8	4.0	3.3	8.2	19.3
PMA-2 mine	6.6	4.2	3.0	3.0	26.3	12.4
Coin (50-cent)	2.9	4.1	3.8	5.1	10.9	13.2
Cilinder	6.8	4.3	4.1	4.2	19.4	9.7
Overall	**4.5**	**3.8**	**3.6**	**3.9**	**26.3**	**20.8**

(b)

Objects	MedAE [mm]		IQR [mm]		Max error [mm]	
	NLS	CNN	NLS	CNN	NLS	CNN
Ball	22.4	5.5	20.2	6.3	38.7	15.3
Bottle cap	13.0	8.1	9.3	10.2	23.7	28.4
PMA-1	11.5	7.7	9.6	20.5	35.3	32.3
Coin (50-cent)	43.4	16.4	35.5	21.5	67.9	39.6
Cilinder	22.8	7.1	30.5	8.3	70.3	20.1
Overall	**22.7**	**9.4**	**21.8**	**14.2**	**70.3**	**39.6**

addition, the CNN estimates depth in the order of milliseconds, while the NLS requires some time to solve (3.63), up to 6 seconds for greater depths (on standard PC). The NLS performance could improve by using longer and denser scanning patterns. However, this would take more time and would, therefore, be less suitable for practical applications. On the other hand, using the depth estimated by the CNN would relax the above requirements considerably and allow faster and more accurate estimation of other inversion parameters.

Another way the proposed method can be utilized is to evaluate the inversion parameter estimates (i.e., object's features), especially at larger depths. If the depth obtained with NLS

inversion and CNN are closely matched, this would imply a higher likelihood that the depth estimates correspond to the object's true depth and, therefore, a higher chance that the feature estimates accurately represent the actual object.

Chapter 5

Landmine Identification From Pulse Induction Metal Detector Data Using Machine Learning

This chapter is based on the following publication:

M. Šimić, D. Ambruš and V. Bilas, "Landmine Identification From Pulse Induction Metal Detector Data Using Machine Learning," in IEEE Sensors Letters, vol. 7, no. 9, pp. 1-4, Sept. 2023.

The last two chapters were dedicated toward improvements in the feature extraction level, Fig. 2.13. As highlighted in Section 2.3.4, this level is considered critical in the development of discrimination-enabled MD. The system capable of extracting intrinsic features (in the form of MPT eigenvalues) of hidden metallic objects was presented in Chapter III. Chapter IV examined difficulties with deeply buried objects and presented a possible solution to address this problem. However, the part still missing in the system concerns the decision-making level (i.e., classification).

When developing a classification strategy for a landmine/clutter problem, one should remember two important things. First, a classifier should be designed to virtually eliminate the number of FNs (i.e., threat misclassified as non-threat) as it represents the most dangerous scenario for the deminer's safety. Second, automated classification should be considered additional support, and the deminer always makes the final decision. Therefore, classifiers that provide a confidence score, such as probability, should be preferred rather than only providing the most likely class. This would inform the deminer on the reliability of the classifier's decision and ultimately reduce the risk of accidents.

This chapter builds upon the system presented in Chapter III. It describes the development of a simulation-based ML model for the identification of small metallic objects (e.g., LMC landmines). Finally, we conclude with a thorough analysis of the model's performance compared with five commonly employed ML approaches for classifying hidden metallic objects.

5.1 Classification strategy

5.1.1 Features

As discussed in Section 3.2.2, eigenvalues ($\lambda_{11}, \lambda_{22}, \lambda_{33}$) are invariant under the spatial rotation of the object and, therefore, only depend on the object's intrinsic properties. However, the rotation may affect the order by which eigenvalue estimates, Table 3.1, are assigned, leading to different feature vectors for the same object. This problem has been analysed recently by Ledger *et al.*, where the authors suggest using tensor invariants in FD, which are independent of how the eigenvalues are assigned [103]. In TD, we can sort eigenvalues in descending order based on $\lambda(t_0)$, where t_0 is the first TG (featuring maximum eigenvalue amplitudes), i.e., $\lambda_{11}(t_0) \geq \lambda_{22}(t_0) \geq \lambda_{33}(t_0)$.

Eigenvalue amplitudes are very sensitive to object localization (especially depth) errors and measurement uncertainties (e.q., sensor drift effects) and can hardly be used as a reliable feature for classification purposes. So before constructing a feature vector, eigenvalues ($\hat{\lambda}_{11}, \hat{\lambda}_{22}, \hat{\lambda}_{33}$) are normalized, i.e., each eigenvalue is divided by $\lambda_{11}(t_0)$, which is the maximum value across all three eigenvalues.
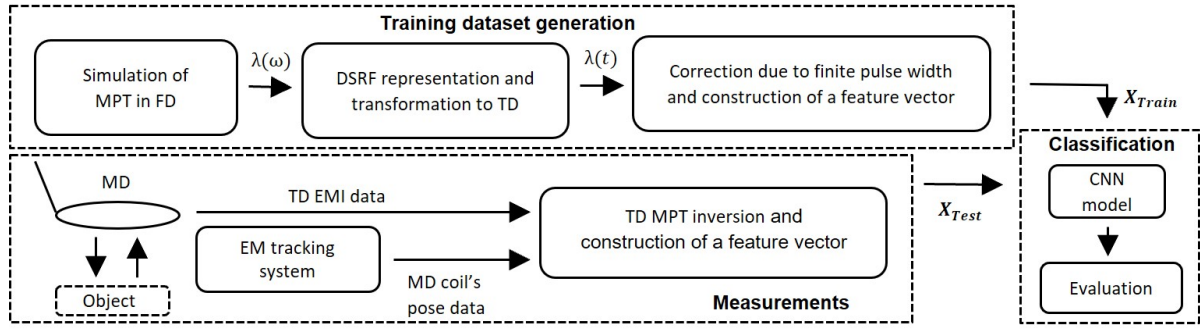
Figure 5.1: Flow chart of the proposed classification strategy [146].

This way, we rely on temporal features of eigenvalues and relative ratios among them rather than their absolute values. Finally, the feature vector $\boldsymbol{x}$ is obtained by concatenation,

$$\boldsymbol{x} = [\hat{\lambda}_{11}(t); \hat{\lambda}_{22}(t); \hat{\lambda}_{33}(t)]. \tag{5.1}$$

The feature vector in the form of (5.1) is used as the input vector of each classification algorithm presented in this chapter.

5.1.2 Training dataset generation and measurements

Fig. 5.1 presents the flow chart of the proposed classification strategy. Simulations are obtained following the same procedure described in Section 3.3.4. As discussed in Section 3.3.1, once the eigenvalues of an object are obtained using MPT-Calculator software, we can calculate the eigenvalues of other objects featuring the same shape B and relative magnetic permeability μ_r, but different size α or electrical conductivity σ by applying the scaling rules [102],

$$\lambda(\alpha B, \omega, s\sigma, \mu_r) = \lambda(\alpha B, s\omega, \sigma, \mu_r) \tag{5.2}$$

and

$$\lambda(s\alpha B, \omega, s\sigma, \mu_r) = s^3 \lambda(\alpha B, s^2\omega, \sigma, \mu_r), \tag{5.3}$$

where s is the scaling factor. Equations (5.2) and (5.3) allow rapid data augmentation which is utilized for training dataset construction (further elaborated in Section 5.2.2).

Eigenvalues from the measurements are obtained using the algorithmic approach described in Section 3.3.2, Table 3.1.

5.1.3 Traditional machine learning models

The performances of five different ML models have been tested: SVM, PNN, kNN, multinomial logistic regression (MNL), and RF. The selection of models was motivated by their previous

Table 5.1: Model configurations selected during hyperparameter optimization. Each class is represented by 80 instances (elaborated in Section 5.3).

Model	Best hyperparameters
SVM	'C': 1, 'kernel': 'rbf', 'gamma': 'scale'
PNN	sigma: 1, 'metric': 'euclidean'
kNN	'n_neighbors': 3, 'weights': 'uniform', 'metric': 'euclidean'
Logistic regression	'C': 0.1, 'penalty': 'l1', 'solver': 'saga'
Random forest	'n_estimators': 50, 'max_depth': None, 'min_samples_split': 2, 'min_samples_leaf': 1

success on similar classification problems (see Section 2.3.2). The algorithms considered can be found in libraries such as scikit-learn [147], which is the implementation employed in this study. Each model requires hyperparameters to be set prior to training, which plays a critical role in configuring the model's structure and how it learns from the data. Hyperparameter optimization is done using a 5-fold cross-validation approach. Final model configurations are summarized in Table 5.1.

As shown in Section 5.3, the model achieving the best generalization performance among the traditional ML algorithms is MNL. An MNL is a (discriminative) generalized linear model which uses *softmax* activation function to calculate the probability P that the observation $\mathbf{x}$ belongs to each class. Mathematically, we can write

$$softmax_k(\mathbf{w}^T\mathbf{x}) = \frac{exp(\mathbf{w}_k^T\mathbf{x})}{\sum_{i=1}^{N} exp(\mathbf{w}_i^T\mathbf{x})} = P(y = k|\mathbf{w}^T, \mathbf{x}), \qquad (5.4)$$

where $\mathbf{w}_k$ is vector of learnable model parameters for class k, and N is number of classes. As discussed earlier, a model that provides class probabilities is desired considering practical aspects in HD, which is another important benefit of MNL.

The initial success of the MNL model has provided a strong foundation for further development. An area for improvement lies in exploiting the intrinsic temporal dependencies within the eigenvalues originating from their decaying nature. It is important to recognize that MNL assumes little or no multicollinearity among independent variables (i.e., features) and combines them linearly [148]. This means it does not inherently account for interactions between features, including their context or relationship with adjacent time points, but rather, each of them is weighed individually. To address this limitation, we propose an approach involving the transformation of the input feature space into a domain where the MNL model can effectively capture these dependencies. This leads us to the concept of a generalized MNL model in the form of 1D-CNN architecture described in the following section.

5.1.4 Classification using 1D-convolutional neural network

There are several reasons why a CNN is well-suited for this classification problem. Firstly, CNN leverages convolutional layers to effectively extract temporal dependencies within the feature vector (5.1). Furthermore, compared to traditional ML models like MNL or SVM, CNN scales better as the amount of training data increases. Finally, by utilizing kernels smaller than the input data, CNN can significantly reduce the number of trainable weights compared to traditional neural networks. This reduction is reflected in lower memory requirements and faster computation times, making CNN suitable for practical applications.

The employed 1D-CNN architecture consists of three layers and can be functionally divided into two parts: feature extraction and classification, Fig. 5.2. In the first layer, each of the 16 filters of size 17 is convolved with an input vector (5.1), resulting in a feature map of dimension 269x16. Filters that slide over the input feature vector are responsible for capturing temporal patterns in data. The second layer performs max pooling over the feature maps with a window size of 6 and a stride of 2. Max pooling operation takes the maximum value within the window, followed by shifts defined by the stride parameter. This downsamples the data while extracting more general patterns resistant to small variations in the input vector. The resulting feature map has a dimension of 132x6. The output of this layer is then flattened into a vector, finalizing
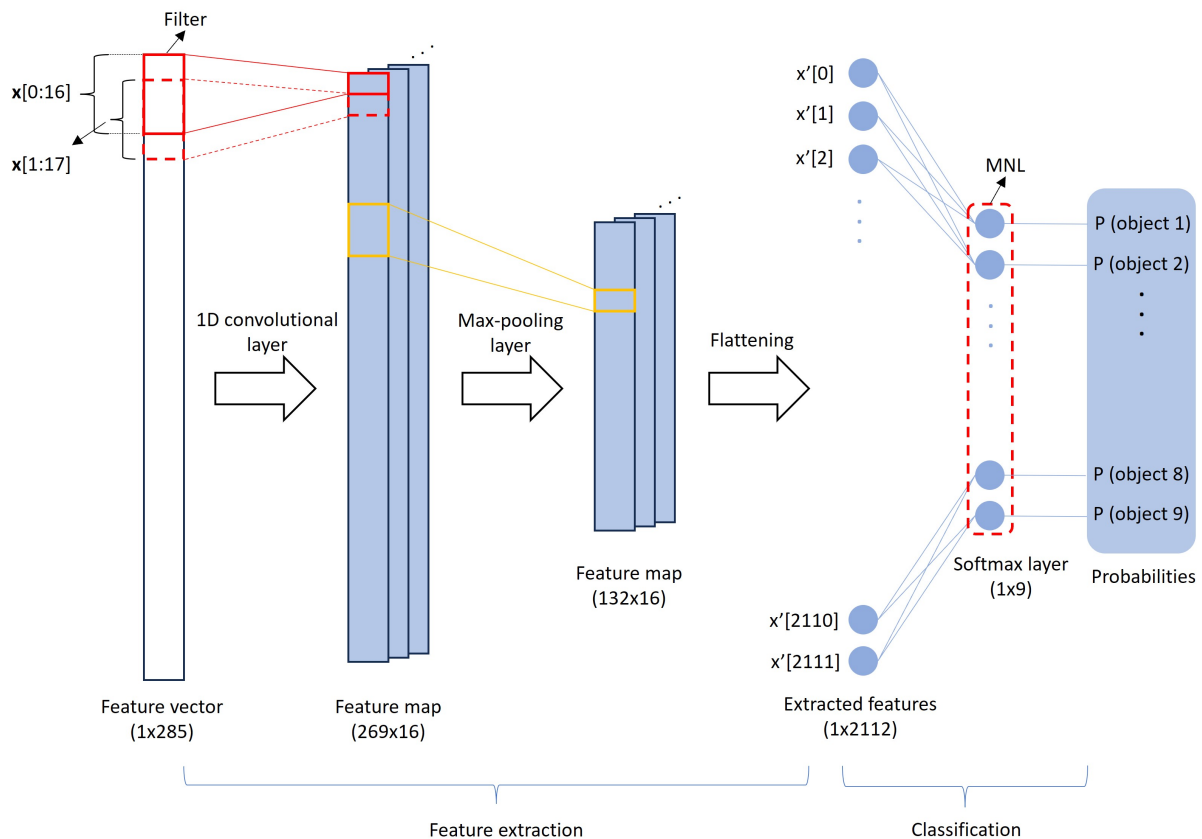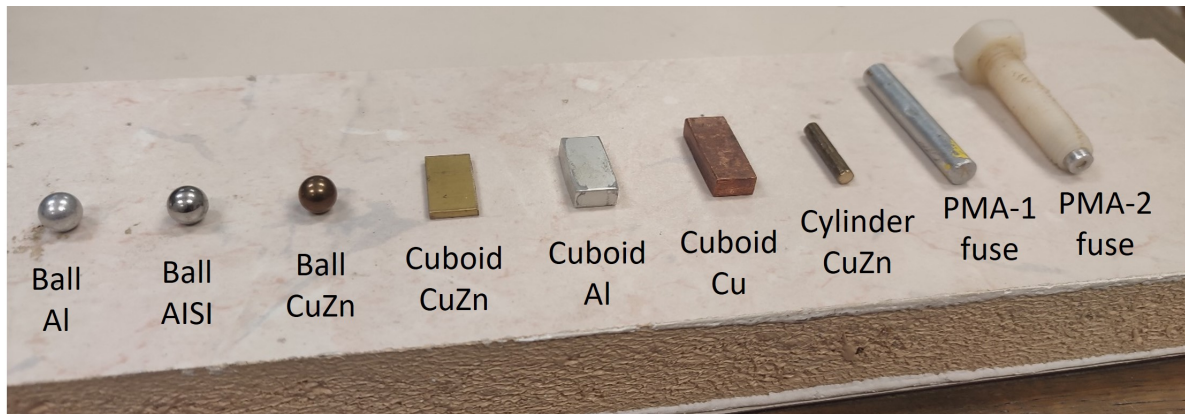

Figure 5.2: CNN architecture.

Figure 5.3: Test objects.

the feature extraction stage. The rest of the network is organized as a one-layer feedforward network classifier with 9 units and softmax activation. This is essentially the same as the MNL model, except it is applied in a transformed feature space.

The dataset of 540 samples (60 per class) was used for training and 180 samples for validation. The CNN hyperparameters (e.g., the number of layers, filters, and filter size) are determined using a Bayesian optimization approach. The selected model minimizes the validation loss over the first 20 epochs. Training on a PC featuring an Intel Core i7-8750H CPU (2.20GHz) and 16 GB of RAM (Python implementation, Keras with TensorFlow backend) takes less than 2 seconds. Once trained, the CNN model requires only 255 kB of memory to store its weights.

5.2 Experimental validation

5.2.1 Experimental setup

A physical implementation of the experimental setup is given in Fig. 3.4. For more details, the reader is referred to the Section 3.3.3.

5.2.2 Dataset construction and processing

Each object is represented by one class, which is created in a similar manner as suggested in [83]. In the first step, FD eigenvalues are calculated with MPT-Calculator software using the setup described in Section 3.3.4. In the second step, data augmentation is done by leveraging the scaling property with respect to the object conductivity σ (5.2). In particular, we use calculated eigenvalues to obtain training and validation dataset samples uniformly distributed within $\pm 5\%$ of the object's σ. This way, prediction models learn to ignore slight variations in σ to account for the measurement uncertainties (e.g., temperature effects, curved surfaces). Once the dataset in FD is generated, transformation to TD is done following the procedure described in Section

Table 5.2: Test dataset (Fig. adapted from [146]).

Object	Dimensions [mm]	Material	σ [MS/m] Declared	σ [MS/m] Meas	Number of experiments
Ball 1	D=8	AISI 316	1.3		15
Ball 2	D=8	AL1050	36		15
Ball 3	D=8	CuZn35	14		15
Cuboid 1	20x10x2	CuZn		14	15
Cuboid 2	20x9x5	Al		30	15
Cuboid 3	29x10x5	Cu		58	15
Cylinder	L=20, D=4	CuZn		12.5	15
PMA-1	L=43, D=7	Al		26	15
PMA-2	L=10, D=6	Al		34	15
Total					**135**

3.3.4. In the last step, feature vectors are calculated using (5.1).

Details related to the measurement procedure are also given in Section 3.3.4. The collected dataset is summarized in Table 5.2.

5.3   Results and discussion

Algorithms were trained on the simulated dataset and tested on a dataset obtained as described in Section 5.2.2. The results shown for CNN and RF models represent the average performance over ten runs due to the stochastic nature of their training process.

Fig. 5.4 shows classifier performance for different number of training instances per class, $N^{(k)}$, with a fixed number of TGs set to 95. Note that the size of the feature vector is $3\times$ number of TGs, (5.1). For smaller $N^{(k)}$, we can observe a significant improvement in CNN performance for increasing $N^{(k)}$, which is not apparent in the case of traditional models. CNN is prone to overfitting for smaller datasets due to its capacity to memorize the training data. However, this is not problematic since the model is trained on a simulated dataset whose expansion is not time-consuming. Overall, the performances of SVM, PNN, and RF models show minimal variation with increasing $N^{(k)}$ (SVM and PNN curves are overlapped). A slight improvement is observed for the kNN classifier with larger datasets (elaborated later on); however, this algorithm does not scale well with increasing dataset size. In particular, it needs to access all training data for predictions, making it computationally expensive and memory-intensive. This limits its applicability to resource-constrained devices. The PNN model has similar scalability issues.
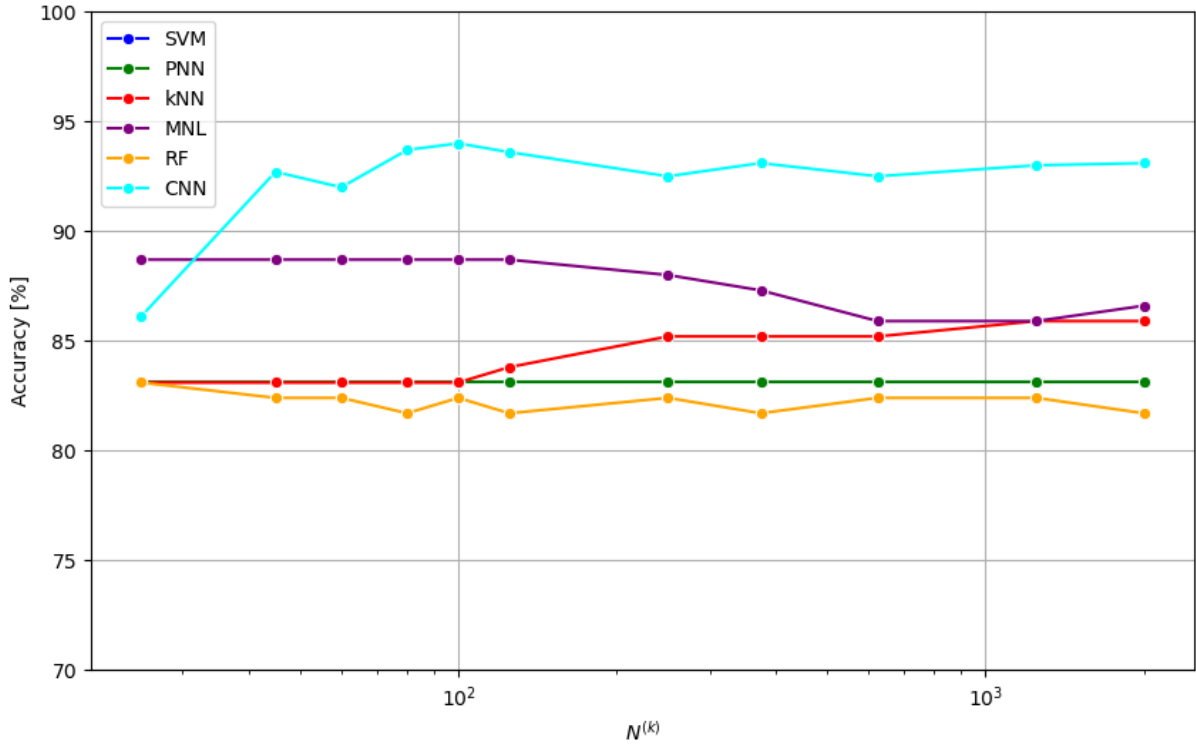
Figure 5.4: Model accuracy for different number of training instances per class.

A decline in MNL performance can be linked to overfitting issues; the model tends to fit too closely to the training data, leading to increased misclassifications as the dataset grows. For subsequent analysis, $N^{(k)}$ is set to 80. We aim to make a compromise between providing enough data to train the models effectively and avoiding the computational and memory constraints associated with larger datasets.

Fig. 5.5 shows the relationship between classifier performance and number of TGs used for feature vector construction. All algorithms exhibit increasing trend in performance with the increasing number of TGs up to 75. However, only two models, MNL and CNN, take full advantage of all TGs acquired by MD. The other classifiers exhibit a decrease in performance for later TGs (i.e., beyond 75). The most affected is kNN, followed by SVM and PNN (curves overlapped), and the least affected model is RF. This may be attributed in part to the curse of dimensionality, also known as the Hughes phenomenon, which refers to the situation when adding more features for the same $N^{(k)}$ degrades the classifier's performance [149]. The curse of dimensionality can be addressed by increasing the $N^{(k)}$, as evidenced by the improved performance of kNN for larger datasets, Fig. 5.4. Another challenge is associated with the decaying nature of eigenvalues. As a result, measurements at later TGs may have significantly lower SNR, which we did not account for in simulations. Therefore, patterns learned by classifiers on simulated datasets may not be robust to measurement uncertainties. A common approach to tackle the above challenges is dimensionality reduction in the form of feature selection or feature extraction. For example, the MNL model has built-in feature selection due to 'l1' reg-
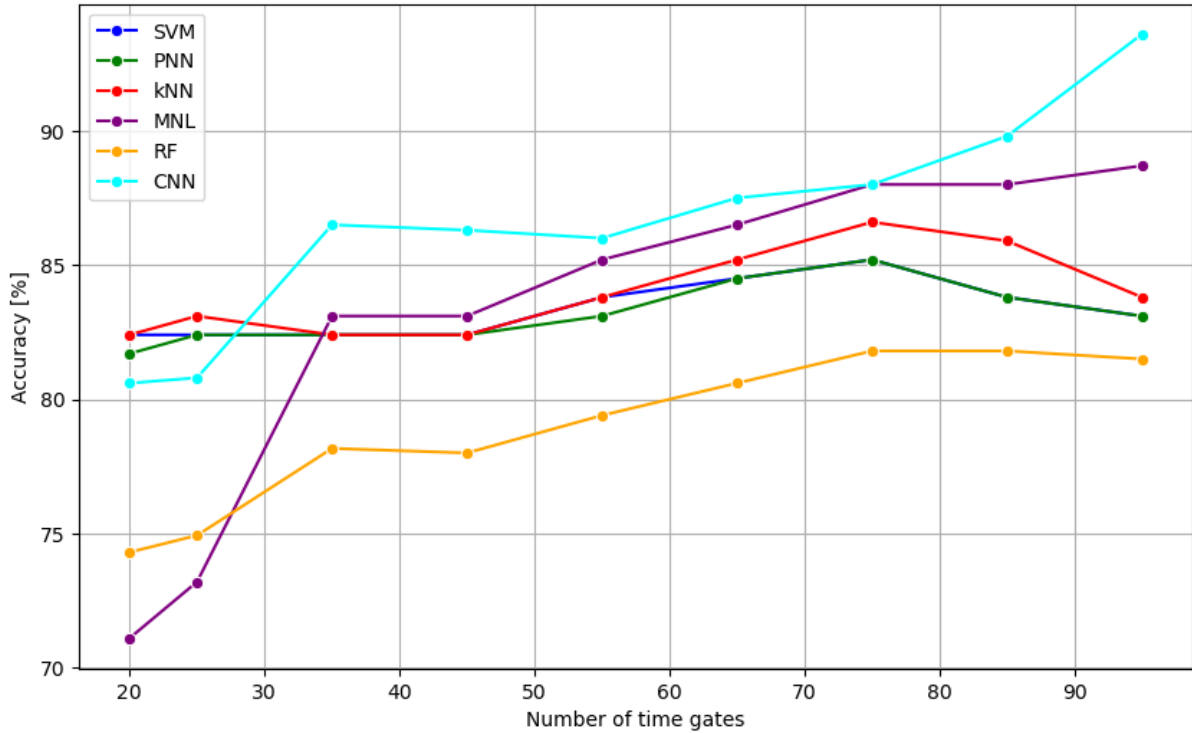
Figure 5.5: Model accuracy for different number of time gates.

ularization, while the CNN model has built-in feature extraction in the form of convolutional and max pooling layers. This may explain why MNL and CNN do not exhibit performance decreases at later TGs as other classifiers but rather an improvement. RF shows worst generalization capabilities among classifiers. This is likely due to the sub-optimal model configuration selected during hyperparameter optimization. We expect performance to be significantly better if measurements were included in training procedure. However, incorporating measurements into the training process would deviate from the study's objective of assessing the model's generalization capabilities when trained exclusively on simulations. In the following, we focus on MNL and CNN, the two best performing algorithms. Their detailed performance is summarized using confusion matrices, Table 5.3.

First and foremost, both algorithms correctly classified all occurrences of landmines PMA-1 and PMA-2. Furthermore, not a single innocuous object was misclassified as a landmine. Therefore, from the perspective of binary classification (threat or non-threat), the algorithms achieved a perfect score. However, this is not the case when it comes to multi-class classification. The degradation in performance for both algorithms is related to missclassification of aluminum ball and copper cuboid. For instance, MNL misclassified 4 aluminium ball measurements and identified only 5 of 15 copper cuboids, Table 5.3a. On the other hand, CNN showed a significant improvement in cuboid classification and slightly better performance in ball classification, Table 5.3b. Better performance and scalability with increasing dataset size make CNN a preferable approach over MNL for our classification problem.

Table 5.3: Classification results. (a) MNL. (b) CNN - the performance over 10 consecutive runs.

(a)

		Predicted object								
Model: MNL		**Ball Al**	**Ball AISI**	**Ball CuZn**	**Cub. CuZn**	**Cub. Al**	**Cub. Cu**	**Cyl. CuZn**	**PMA-1**	**PMA-2**
True object	**Ball Al**	11	0	4	0	0	0	0	0	0
	Ball AISI	0	15	0	0	0	0	0	0	0
	Ball CuZn	0	0	15	0	0	0	0	0	0
	Cub. CuZn	0	0	0	15	0	0	0	0	0
	Cub. Al	0	0	0	0	14	1	0	0	0
	Cub. Cu	0	0	0	0	10	5	0	0	0
	Cyl. CuZn	0	0	0	0	0	0	15	0	0
	PMA-1	0	0	0	0	0	0	0	15	0
	PMA-2	0	0	0	0	0	0	0	0	15
Accuracy = 88.9%										

(b)

		Predicted object								
Model: CNN		**Ball Al**	**Ball AISI**	**Ball CuZn**	**Cub. CuZn**	**Cub. Al**	**Cub. Cu**	**Cyl. CuZn**	**PMA-1**	**PMA-2**
True object	**Ball Al**	120	0	30	0	0	0	0	0	0
	Ball AISI	0	150	0	0	0	0	0	0	0
	Ball CuZn	0	0	150	0	0	0	0	0	0
	Cub. CuZn	0	0	0	150	0	0	0	0	0
	Cub. Al	0	0	0	0	144	6	0	0	0
	Cub. Cu	0	0	0	0	50	100	0	0	0
	Cyl. CuZn	0	0	0	0	0	0	150	0	0
	PMA-1	0	0	0	0	0	0	0	150	0
	PMA-2	0	0	0	0	0	0	0	0	150
Accuracy = 93.6%										

Difficulties in distinguishing between balls and cuboids of the same or similar shape but different conductivity suggest that changes in feature space are more affected by changes in object shape than conductivity (or size). For example, algorithms did not struggle to discriminate between PMA-1 and PMA-2 landmines featuring similar conductivity but different shapes. This can be explained by observing how object conductivity and shape changes affect eigenvalues. Let us take, for example, the aluminium ball, which is often misclassified as a brass ball (i.e., same shape, different conductivity), Fig. 5.6. An increase in conductivity shifts the eigenvalues of the aluminium ball to the lower frequencies [18]. In TD, this reflects a decrease in amplitude at early TGs corresponding to the high-frequency spectrum and an increase in amplitude at later TGs corresponding to the low-frequency spectrum. Since we perform normalization of eigenvalues, the difference is only apparent at later TGs, Fig. 5.6. As discussed above, later TGs are characterized by higher measurement uncertainties, which can cause difficulties for the classifier to make the correct decisions. A similar analysis can be applied to object size. In particular, an increase in size shifts eigenvalues to the lower frequencies and increases their amplitudes [18]. Normalization nullifies the amplitude variations, and consequently, the changes are again only visible on later TGs. On the other hand, objects with different shapes will have different ratios among eigenvalues, which appears in early TGs (see Fig. 3.10a and c); therefore, they are less prone to measurement uncertainties. This has important implications when it comes to classifier development for landmine identification. In particular, objects having similar shapes as landmines should be generally avoided in the non-threat category to reduce the chance of FNs. To summarize, the above study yields the following contributions:

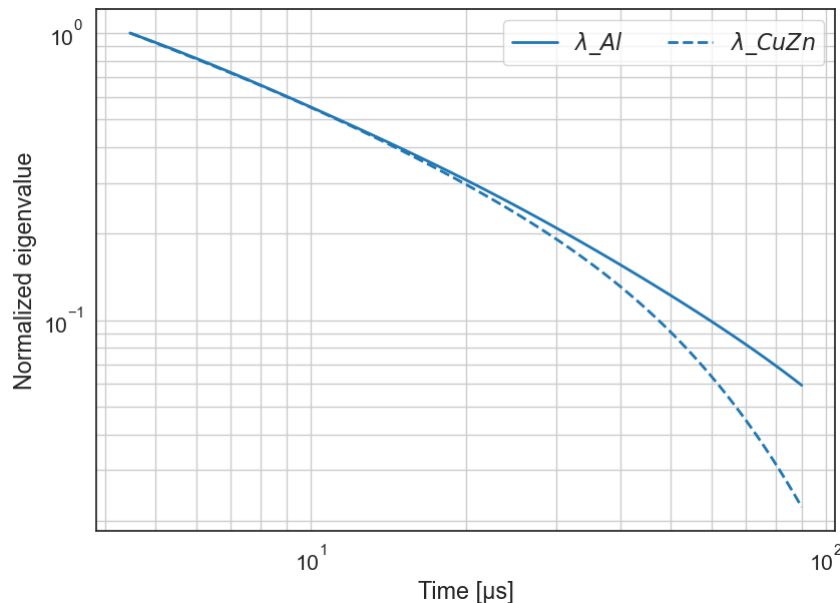•Firstly, we showed for the first time that it is possible to use simulation-trained ML models

Figure 5.6: Comparison of eigenvalues of aluminium and brass balls.

to identify LMC landmines (PMA-1 and PMA-2) from TD MD measurements.

- Secondly, we developed a novel classification strategy based on 1D-CNN, which showed superior generalization performance over the traditional ML models on a comprehensive dataset of threat and non-threat objects.

Chapter 6

Conclusions and future work

The inability of metal detectors (MDs) to discriminate between harmless metallic clutter and dangerous landmines remains a major technological limitation in humanitarian demining (HD). In the last several decades, efforts have been put into allowing the shift from the concept of metallic object detection to metallic object discrimination for safer, cheaper, and faster HD. As postulated in Chapter I and further elaborated in Chapter II, the main objective of this thesis was to build upon these efforts and shed new light on the practical abilities of electromagnetic induction (EMI)-based systems employed in HD.

6.1   Contribution of the thesis

The research's first hypothesis (**H1**) is that small metallic objects, such as low-metallic content (LMC) landmines, can be represented by point magnetic dipoles, whose magnetic moment is induced by the sensor's primary magnetic field at the dipole's location. More specifically, an object can be uniquely parametrized by the dipole magnetic polarizability tensor (MPT) elements and the dipole location. This hypothesis has been supported by an in-depth review of relevant literature in Chapter II, the engineering practices used in landmine and unexploded ordnance detection, and similar applications in fields like security screening and the food industry. Furthermore, detailed insight into induced dipole model derivation in both frequency-domain (FD) and time-domain (TD), as well as theoretical background justifying its use is given in Chapter III. The dipole model, linking the EMI response with the object's intrinsic parameters (in the form of MPT eigenvalues), has been used in each study presented in this thesis.

The second hypothesis (**H2**) postulated in this thesis assumes that robust discriminative features could be estimated from pulse induction MD data and sensor positional data obtained during a manual scan over a buried object. It is expected that the accuracy of the feature estimation may be sufficient for object classification purposes. This leads us to the first thesis contribution.

C1:Method for measurement of the magnetic polarizability tensor using pulse induction metal detector.

While MPT eigenvalues have proven to provide a good basis for the discrimination of small metallic objects, the ill-posedness of the inverse problem, which needs to be solved to obtain eigenvalues from measurements, limits their use in practice. As discussed in Chapters II and III, difficulties originate from strong correlations between the MPT and the object location, as well as uncertainties in sensor data (especially those associated with positional errors). For these reasons, linking MPTs derived numerically and those acquired through measurements is difficult. Consequently, modern systems featuring metallic object discrimination usually rely on libraries of measured MPTs. These are, however, susceptible to error due to uncertainties in the sensor data, which are system-specific. Therefore, libraries must be created for each system individually, which is time-consuming and poses one of their main limitations in practice.

Chapter III presents a novel approach for inversion-based MPT measurement using a mono-coil pulse induction MD and an electromagnetic (EM) tracking system. To deal with the ill-posedness of the inverse problem, the presented approach capitalizes on the recent developments in the MD search head tracking problem. Specifically, the employed EM tracking system feature means absolute accuracy in millimetre order. High accuracy in combination with a position update rate of ≈ 38 ms (the scanning speed up to 30 cm/s) proved to be sufficient for reliable estimation of MPT of small metallic objects for standard scanning patterns used in demining. For the first time, it has been demonstrated that the MPT of arbitrarily shaped objects can be reliably obtained from measurements. Unlike the existing systems for MPT measurement, which typically involve complex laboratory setups and operate in FD, the proposed system operates in TD and is based on commercially available MD and EM tracking systems, which are portable and, therefore, suitable for operation in the field.

The accuracy evaluation was done using MPT simulations initially calculated in FD. A novel methodology has been developed to transform FD MPT to TD equivalents based on a discrete spectrum of relaxation frequencies (DSRF). The proposed methodology offers several advantages over the standard signal processing techniques used for FD to TD transform, which involve the direct application of inverse Fourier transform. Representing the eigenvalues in the DSRF domain allows simple table-based FD to TD transform. Furthermore, correcting the eigenvalues due to the finite width of the transmitter pulse of the MD requires only the multiplication operation. Finally, eigenvalues in TD can be calculated at arbitrary time stamps, which is essential to establish a relationship between simulations and measurements.

Measurement errors obtained with the proposed system are significantly lower than those obtained with state-of-the-art systems. Considering the research work and the results referenced in Chapter III, the contribution **C1** may be declared accomplished.

C2: Method for evaluation of features derived from the time-domain magnetic polarizability tensor for metallic object classification.

In Chapter III, it is demonstrated that MPT measurements at lower depths (i.e., below 10 cm) show a very good agreement with simulations. At greater depths, measurement uncertainties increase due to lower SNR and directional sensitivity gradients; therefore, a strong correlation between the intrinsic parameters of the object and its depth comes to the fore. Consequently, the nonlinear least squares (NLS) algorithm has a greater chance of finding the sub-optimal solution.

Chapter IV presents a machine learning (ML)-based approach for rapid estimation of metallic object depth from line-scan EMI data. The proposed approach takes advantage of the fact that sensitivity patterns of a line-scan remain the same for the same coil geometry and object location, regardless of the orientation and material properties of the object. It is demonstrated that the 1D-convolutional neural network (1D-CNN) model can effectively capture spatial features contained in these patterns. The proposed approach offers several advantages over the existing methods. Depth estimation can be obtained in a relatively short time. Typically, two line-scans of the object are enough to obtain an accurate estimate. The algorithm is trained exclusively on simulations. This allows the construction of a comprehensive training dataset so the CNN model can learn depth-specific features and make accurate estimates regardless of the object's orientation or shape, size, and material properties.

The performance evaluation is done in comparison with the NLS inversion approach. While both algorithms perform well at lower depths, CNN significantly outperforms NLS at depths greater than 10 cm. The proposed method can be employed to assess the estimates of MPT parameters (i.e., the object's features) obtained by the NLS inversion approach, especially at greater depths. If the depths determined through NLS inversion and CNN closely match, this suggests a higher probability that the depth estimates accurately reflect the object's true depth. Consequently, this increases the likelihood that the estimates of the features accurately represent the actual object.

Considering the research work and the results referenced in Chapter IV, the contribution **C2** may be declared accomplished.

C3: Machine learning-based method for classification of metallic objects in humanitarian demining.

Chapter V discusses the further development of the system presented in Chapter III. Specifically, it presents a novel classification strategy based on 1D-CNN for the identification of small metallic objects of practical interest in HD. For the first time, it was shown that using simulation-trained ML models to identify LMC landmines (PMA-1 and PMA-2) from TD MD

measurements is possible.

Object discrimination relies on temporal information of MPT eigenvalues and relative ratios among them rather than their magnitudes. This is an important feature that contributes to the robustness of the algorithm. CNN leverages convolutional layers to effectively extract temporal dependencies within the feature vector. Compared to traditional ML algorithms, CNN scales better as the amount of training data increases. Using the kernel smaller than the input, CNNs may have significantly fewer weights than the traditional neural networks, reducing memory requirements and computation time, making it suitable for practical application.

The proposed CNN-based classification strategy achieved superior generalization performance on a comprehensive dataset of threat and non-threat objects, outperforming five alternative ML models that have been successful in similar classification tasks.

Considering the research work and the results referenced in Chapter V, the contribution **C3** may be declared accomplished.

6.2 Future work

MPT measurement

The proposed NLS inversion procedure uses a relatively simple regularization method, which assumes non-negative MPT eigenvalues reflecting a decaying nature of eddy currents. Nonetheless, this does not restrict the slope of estimated eigenvalues. Therefore, additional regularization methods could also be employed based on the assumption that eigenvalues are monotonically decreasing time functions.

Another aspect is related to the spatial resolution of EMI response, which necessarily affects the inversion performance. Spatial resolution can be improved by decreasing the averaging window of the MD data. However, reducing the size of the averaging window also reduces the SNR of the measurements. It is, therefore, necessary to investigate the window range in which the system achieves a robust estimate.

So far, the experiments have only covered a limited number of targets and test scenarios. In future work, we will evaluate the system's performance on a dataset, including ferrous metallic objects and objects placed at greater depths.

Finally, further research will concern a situation where objects are buried in the ground. In this case, the EMI sensor measurements may be significantly affected by the uncooperative soil response, which could result in poor method performance. Therefore, the development of the soil compensation technique and the practical application of the proposed solution under uncooperative soil conditions will be part of future work.

Object depth estimation

The ML-based algorithm presented in Chapter IV showed superior performance over NLS inversion regarding the depth estimation problem. The next step involves the integration of these two algorithms. It is expected that using the depth estimated by the CNN approach or restricting the bounds of its search space would enhance the speed and accuracy of the feature extraction process, particularly at greater depths.

As discussed in Section 4.3.3, manual movements with MD in the air can cause significant distortions in the line-scans (mainly due to MD lift-off), leading to erroneous depth estimates. Uncertainty of estimates due to distorted line-scans is reduced by using the two line-scans instead of one. Further improvement is possible by increasing the number of line-scans. However, this would require more time for estimation, which is not desired from the practical perspective. Another approach would involve more sophisticated signal processing of highly distorted line-scans (e.g., by employing forward modelling techniques, such as those based on induced dipole model approximation). This would reduce the uncertainty of depth estimates and the number of required line-scans, potentially enabling significant time savings.

Similarly to MPT measurement, it is necessary to investigate the limits of MD scan speed, i.e., how line-scans' spatial resolution affects the algorithm's performance. The practical application of the proposed approach under uncooperative soil conditions will also be part of future work.

Classification

As elaborated in Section 5.3, the proposed classification approach may face difficulties discriminating objects featuring similar shapes. This limitation arises from the eigenvalue scaling, which disregards their amplitudes. As a result, differences in object conductivities and size are only apparent at later time gates of eigenvalues (where the SNR is lower), increasing uncertainties of classifier predictions. As discussed in Section 5.1.1, scaling is important for maintaining the robustness of the classifier. Hence, it is necessary to investigate alternative methods to incorporate eigenvalue amplitude information into the feature vector. This would improve the classifier's ability to make correct decisions based on differences in object conductivity and size properties.

Another research track will be related to the modifications in training dataset construction to cover more realistic scenarios. For example, in Chapter III, when analysing eigenvalue measurement errors, it was identified that the measurement uncertainty is inversely proportional to the eigenvalue amplitudes. Therefore, the largest error is observed in the eigenvalue with the lowest amplitude. This means the algorithm performance may be improved by including these uncertainties in training dataset construction.

Bibliography

[1] *Landmine & Cluster Munition Monitor*. [Online]. Available: http://www.the-monitor.org/en-gb/the-issues/landmines.aspx, accessed November 14, 2023.

[2] W. van Verre, L. A. Marsh, J. L. Davidson, E. Cheadle, F. J. W. Podd, and A. J. Peyton, "Detection of metallic objects in mineralized soil using magnetic induction spectroscopy," *IEEE Transactions on Geoscience and Remote Sensing*, vol. 59, no. 1, pp. 27–36, 2021.

[3] *Database of Demining Accidents (DDAS) 2005-2010*. [Online]. Available: https://www.ddasonline.com/AccidentrecordsDDAS.htm, accessed December 1, 2023.

[4] K. Rutherford, *America's Buried History: Landmines in the Civil War*. Savas Beatie, 2020, [Online]. Available: https://books.google.hr/books?id=zOXbDwAAQBAJ, accessed November 23, 2023.

[5] Human Rights Watch and Physicians for Human Rights, *Landmines: A Deadly Legacy*. Human Rights Watch, 1993, [Online]. Available: https://www.hrw.org/reports/pdfs/g/general/general.93o/general930full.pdf, accessed November 16, 2023.

[6] *Hidden killers : the global problem with uncleared landmines : a report on international demining*, ser. Department of State publication; 10098. Washington, D.C: [Office of International Security Operations], 1993.

[7] U. Nations, "Assistance in mine clearance : report of the secretary-general," p. 31 p., Sep 1994. [Online]. Available: http://digitallibrary.un.org/record/162626, accessed November 23, 2023.

[8] J. Williams, "Landmines: A global socioeconomic crisis," *Social Justice*, vol. 22, no. 4 (62), pp. 97–113, 1995.

[9] International Committee of the Red Cross, *Anti-personnel Landmines: Friend Or Foe? : a Study of the Military Use and Effectiveness of Anti-personnel Mines*, ser. ICRC publications. International Committee of the Red Cross, 1996. [Online]. Available:

https://www.icrc.org/en/doc/assets/files/other/icrc_002_0654.pdf, accessed November 24, 2023.

[10] *Milestones in humanitarian mine action: Emergence of the global landmine threat, evolution of landmine policy and development of the discipline of humanitarian mine action (3rd edition).* [Online]. Available: https://2001-2009.state.gov/t/pm/rls/fs/58255.htm, accessed October 10, 2023.

[11] *International campaign to ban landmines – facts.* [Online]. Available: https://www.nobelprize.org/prizes/peace/1997/icbl/facts/, accessed November 14, 2023.

[12] Diakonia International Humanitarian Law Centre, Tech. Rep., June 2020. [Online]. Available: https://reliefweb.int/report/world/humanitarian-demining-form-humanitarian-assistance-under-international-humanitarian-law, accessed December 2, 2023.

[13] *Landmine Monitor 2022, International Campaign to Ban Landmines.* [Online]. Available: http://www.the-monitor.org/media/3352351/2022_Landmine_Monitor_web.pdf, accessed November 14, 2023.

[14] D. of the Army and D. of the Army Headquarters Staff, *Mine/Countermine Operations: Fm 20-32*, 2004. [Online]. Available: https://www.marines.mil/Portals/1/Publications/FM%2020-32%20W%20CH%201-4.pdf, accessed December 5, 2023.

[15] S. Mannion and E. Chaloner, "Chapter 1 landmines and landmine injuries: An overview," *Pain Medicinel*, vol. 7, no. 2, pp. 199–200, 11 2016.

[16] J. MacDonald and J. R. Lockwood, *Alternatives for Landmine Detection.* Santa Monica, CA: RAND Corporation, 2003.

[17] D. Ambruš, "Detection of low-metallic content landmines based on electromegnetic induction model." Ph.D. dissertation, University of Zagreb. Faculty of Electrical Engineering and Computing, 2019.

[18] O. A. Abdel-Rehim, J. L. Davidson, L. A. Marsh, M. D. O'Toole, and A. J. Peyton, "Magnetic polarizability tensor spectroscopy for low metal anti-personnel mine surrogates," *IEEE Sensors Journal*, vol. 16, no. 10, pp. 3775–3783, 2016.

[19] D. Guelle, A. Smith, A. Lewis, and T. Bloodworth, *Metal Detector Handbook for Humanitarian Demining.* Norwich: Office for Official Publications of the European Communities, 2003. [Online]. Available: https://nolandmines.com/PDF_files/MetalDetectorHandbook.pdf, accessed December 2, 2023.

[20] "Law on Mine Action / Zakon o protuminskom djelovanju (in Croatian)," Narodne novine (official gazette) 110/15, valid from 10.6.2023.

[21] "Standard operating procedures: survey / Standardne operativne procedure: izvid (in Croatian)," 2009. [Online]. Available: https://civilna-zastita.gov.hr/UserDocsImages/d okumenti/Razminiranje/SOP/01%2001-OPCI%20IZVID_%20PRIHVACENE%20IZ MJENE%20_I_DOPUNE_ng_22_09_09.pdf, accessed December 10, 2023.

[22] "Rules and Regulations on Methods of Demining / Pravilnik o na činu obavljanja poslova humanitarnog razminiranja (in Croatian)," Narodne novine (official gazette) 110/15, valid from 13.5.2016.

[23] A. Smith. *Humanitarian mine action: Global standard operating procedures (sops).* [Online]. Available: https://nolandmines.com/Global_SOPs/V3.0_Global_SOPs_Chap_ 6_Search_and_Clearance.pdf, accessed: November 22, 2023.

[24] F3 Metal Detector, 2023. [Online]. Available: https://www.minelab.com/countermine/de tectors/f3-landmine-detector-by-minelab, accessed December 30, 2024.

[25] U. A. Meteorites. *UK Polar Meteorite Exploration and Research.* [Online]. Available: https://ukantarcticmeteorites.wordpress.com/metal-detection-technology/, accessed February 26, 2024.

[26] *Humanitarian Mine Action - Test and Evaluation - Metal Detectors, CEN Workshop Agreement*, CWA-14747, Jun. 2003.

[27] C. Bruschini, "A multidisciplinary analysis of frequency domain metal detectors for humanitarian demining," PhD thesis, Vrije Universiteit Brussel, Belgium, 2006.

[28] I. Won, D. Keiswetter, and T. Bell, "Electromagnetic induction spectroscopy for clearing landmines," *IEEE Transactions on Geoscience and Remote Sensing*, vol. 39, no. 4, pp. 703–709, 2001.

[29] P. Gao and L. M. Collins, "Improved signal processing approaches for land mine detection," in *Detection and Remediation Technologies for Mines and Minelike Targets III*, vol. 3392. International Society for Optics and Photonics, 1998, pp. 1034–1043.

[30] M. Sato, J. Fujiwara, X. Feng, Z.-S. Zhou, and T. Kobayashi, "Evaluation of a hand-held gpr md sensor system (ALIS)," in *IARP International workshop on Robotics and Mechanical Assistance in Humanitarian Demining, Tokyo, Japan*, 2005.

[31] M. Freese, E. Fukushima, and S. Hirose, "Improved landmine discrimination with an off-the-shelf metal detector," *Journal of Conventional Weapons Destruction*, vol. 12, no. 1, p. 45, 2008.

[32] VMF4 Metal Detector. [Online]. Available: https://vallon-metal-detectors.com/en/metal-detector-vmf4, accessed December 30, 2023.

[33] S. Dogru and L. Marques, "Shape reconstruction using a mobile robot for demining and uxo classification," in *2017 IEEE International Conference on Robotics and Automation (ICRA)*. IEEE, 2017, pp. 5659–5665.

[34] C. E. Baum, *Detection and Identification of Visually Obscured Targets*. New York: Taylor & Francis, 1999.

[35] C. Bruschini and H. Sahli, "Phase-angle-based EMI object discrimination and analysis of data from a commercial differential two-frequency system," in *Detection and Remediation Technologies for Mines and Minelike Targets V*, vol. 4038. SPIE, 2000, pp. 1404–1419.

[36] C. Nelson, C. Cooperman, W. Schneider, D. Wenstrand, and D. Smith, "Wide bandwidth time-domain electromagnetic sensor for metal target classification," *IEEE Transactions on Geoscience and Remote Sensing*, vol. 39, no. 6, pp. 1129–1138, 2001.

[37] Y. Das, "A preliminary investigation of the effects of soil electromagnetic properties on metal detectors," in *Detection and Remediation Technologies for Mines and Minelike Targets IX*, vol. 5415. SPIE, 2004, pp. 677–690.

[38] R. L. Van Dam, J. M. Hendrickx, J. B. J. Harrison, and B. Borchers, "Conceptual model for prediction of magnetic properties in tropical soils," in *Detection and Remediation Technologies for Mines and Minelike Targets X*, vol. 5794. SPIE, 2005, pp. 177–187.

[39] S. Billings, L. Pasion, D. Oldenburg, and J. Foley, "The influence of magnetic viscosity on electromagnetic sensors," in *Proceedings of EUDEM-SCOT2, International Conference on Requirements and Technologies for the Detection, Removal and Neutralization of Landmines and UXO*, 2003.

[40] L. R. Pasion, S. D. Billings, D. W. Oldenburg, and S. E. Walker, "Application of a library based method to time domain electromagnetic data for the identification of unexploded ordnance," *Journal of Applied Geophysics*, vol. 61, no. 3-4, pp. 279–291, 2007.

[41] C. Gaudin, C. Sigrist, and C. Bruschini, "Metal detectors for humanitarian demining: a patent search and analysis," Tech. Rep., 2003.

[42] D. Ambruš, D. Vasi ć, and V. Bilas, "Comparative study of planar coil emi sensors for inversion-based detection of buried objects," *IEEE Sensors Journal*, vol. 20, no. 2, pp. 968–979, 2019.

[43] C. Bruschini, "On the low-frequency emi response of coincident loops over a conductive and permeable soil and corresponding background reduction schemes," *IEEE transactions on geoscience and remote sensing*, vol. 42, no. 8, pp. 1706–1719, 2004.

[44] Hand-held GEM-3, product leaflet. [Online]. Available: https://geophex.com/hand-held-gem-3/, accessed March 20, 2024.

[45] J. Braunstein, A. Merz, M. Sautter, and G. Vallon, "New uxo detector with metal-discrimination option," *Journal of ERW and Mine Action*, vol. 12, no. 1, 2008, accessed January 2, 2024. [Online]. Available: https://www.jmu.edu/cisr/journal/12.1/rd/braunstein/braunstein.shtml.

[46] UXO PIDD 2, 2023. [Online]. Available: https://ebingergroup.de/en/uxo-pidd-2/, accessed December 20, 2023.

[47] J. Miller, T. Bell, J. Soukup, and D. Keiswetter, "Simple phenomenological models for wideband frequency-domain electromagnetic induction," *IEEE Transactions on Geoscience and Remote Sensing*, vol. 39, no. 6, pp. 1294–1298, 2001.

[48] E. B. Fails, P. A. Torrione, W. R. S. Jr., and L. M. Collins, "Performance of a four parameter model for modeling landmine signatures in frequency domain wideband electromagnetic induction detection systems," in *Detection and Remediation Technologies for Mines and Minelike Targets XII*, R. S. Harmon, J. T. Broach, and J. H. H. Jr., Eds., vol. 6553, International Society for Optics and Photonics. SPIE, 2007, pp. 77 – 84. [Online]. Available: https://doi.org/10.1117/12.719460.

[49] G. Ramachandran, P. D. Gader, and J. N. Wilson, "GRANMA: Gradient angle model algorithm on wideband EMI data for land-mine detection," *IEEE Geoscience and Remote Sensing Letters*, vol. 7, no. 3, pp. 535–539, 2010.

[50] M.-H. Wei, W. R. Scott, and J. H. McClellan, "Robust estimation of the discrete spectrum of relaxations for electromagnetic induction responses," *IEEE Transactions on Geoscience and Remote Sensing*, vol. 48, no. 3, pp. 1169–1179, 2009.

[51] S. L. Tantum, W. R. Scott, K. D. Morton, L. M. Collins, and P. A. Torrione, "Target classification and identification using sparse model representations of frequency-domain electromagnetic induction sensor data," *IEEE transactions on geoscience and remote sensing*, vol. 51, no. 5, pp. 2689–2706, 2012.

[52]L. Collins, V. George, T. Altshuler, L. Nolte, and L. Carin, "Improved decision-theoretic approach to the optimum detection of mines," in *Detection and Remediation Technologies for Mines and Minelike Targets II*, vol. 3079.   SPIE, 1997, pp. 716–723.

[53]L. Collins and P. Gao, "Hypothesis testing for landmine detection with emi images," in *1998 IEEE International Conference on Fuzzy Systems Proceedings. IEEE World Congress on Computational Intelligence (Cat. No. 98CH36228)*, vol. 1.   IEEE, 1998, pp. 237–240.

[54]L. Collins, P. Gao, and L. Carin, "An improved bayesian decision theoretic approach for land mine detection," *IEEE Transactions on Geoscience and Remote Sensing*, vol. 37, no. 2, pp. 811–819, 1999.

[55]P. Gao and L. M. Collins, "A two-dimensional generalized likelihood ratio test for land mine and small unexploded ordnance detection," *Signal processing*, vol. 80, no. 8, pp. 1669–1686, 2000.

[56]Ping Gao and L. M. Collins, "A theoretical performance analysis and simulation of time-domain emi sensor data for land mine detection," *IEEE Transactions on Geoscience and Remote Sensing*, vol. 38, no. 4, pp. 2042–2055, 2000.

[57]G. D. Sower and S. P. Cave, "Detection and identification of mines from natural magnetic and electromagnetic resonances," in *Detection Technologies for Mines and Minelike Targets*, vol. 2496.   International Society for Optics and Photonics, 1995, pp. 1015–1024.

[58]Y. Hua and T. K. Sarkar, "A discussion of e-pulse method and prony's method for radar target resonance retrieval from scattered field," *IEEE Transactions on Antennas and Propagation*, vol. 37, no. 7, pp. 944–946, 1989.

[59]T. K. Sarkar and O. Pereira, "Using the matrix pencil method to estimate the parameters of a sum of complex exponentials," *IEEE Antennas and Propagation Magazine*, vol. 37, no. 1, pp. 48–55, 1995.

[60]L. R. Pasion and D. W. Oldenburg, "Locating and determining dimensionality of uxos using time domain electromagnetic induction," in *12th EEGS Symposium on the Application of Geophysics to Engineering and Environmental Problems*.   European Association of Geoscientists & Engineers, 1999, pp. cp–202.

[61]L. Beran and D. W. Oldenburg, "Selecting a discrimination algorithm for unexploded ordnance remediation," *IEEE Transactions on Geoscience and Remote Sensing*, vol. 46, no. 9, pp. 2547–2557, 2008.

[62] J. Pablo Fernández, F. Shubitidze, I. Shamatava, B. E. Barrowes, and K. O'Neill, "Realistic subsurface anomaly discrimination using electromagnetic induction and an SVM classifier," *EURASIP Journal on Advances in Signal Processing*, vol. 2010, pp. 1–11, 2010.

[63] A. Bijamov, F. Shubitidze, J. P. Fernandez, I. Shamatava, and B. E. Barrowes, "Comparison of supervised and unsupervised machine learning techniques for uxo classification using emi data," in *Proceedings of SPIE, the International Society for Optical Engineering*, vol. 8017, 2011.

[64] D. Ambruš, D. Vasić, and V. Bilas, "Upgrading metal detection to metallic target characterization in humanitarian demining," in *Proceedings of the 11th International Symposium and Equipment Exhibition "Mine Action 2014"*. HCR-CTRO, 2014, pp. 123–126.

[65] M. N. Keene, M. J. Wooliscroft, R. Humphreys, D. K. Riley, and R. M. Deas, "A novel locating and discriminating metal detector," in *Detection and Remediation Technologies for Mines and Minelike Targets IX*, R. S. Harmon, J. T. Broach, and J. H. H. Jr., Eds., vol. 5415, International Society for Optics and Photonics. SPIE, 2004, pp. 241 – 252. [Online]. Available: https://doi.org/10.1117/12.549692.

[66] I. Shamatava, F. Shubitidze, B. Barrowes, J. P. Fernández, L. R. Pasion, and K. O'Neill, "Applying the physically complete EMI models to the ESTCP Camp Sibert Pilot Study EM-63 data," *Detection and Sensing of Mines, Explosive Objects, and Obscured Targets XIV*, vol. 7303, no. 2, p. 73030O, 2009.

[67] F. Shubitidze, J. P. Fernández, B. E. Barrowes, I. Shamatava, A. Bijamov, K. O'Neill, and D. Karkashadze, "The orthonormalized volume magnetic source model for discrimination of unexploded ordnance," *IEEE Transactions on Geoscience and Remote Sensing*, vol. 52, no. 8, pp. 4658–4670, 2014.

[68] Y. Qin, J. Chen, K. Li, W. Zhang, W. Wang, J. Ouyang, and X. Yang, "Eddy current magnetic localization of nonmagnetic metal targets based on metal shell model," *IEEE Sensors Journal*, vol. 22, no. 11, pp. 10 774–10 782, 2022.

[69] T. H. Bell, B. J. Barrow, and J. T. Miller, "Subsurface discrimination using electromagnetic induction sensors," *IEEE transactions on geoscience and remote sensing*, vol. 39, no. 6, pp. 1286–1293, 2001.

[70] D. Ambruš, D. Vasić, and V. Bilas, "Estimating directional magnetic polarizabilities of metallic objects using planar time-domain electromagnetic induction sensor," in *2016 IEEE Sensors Applications Symposium (SAS)*, 2016, pp. 1–5.

[71] H. Huang and I. J. Won, "Automated identification of buried landmines using normalized electromagnetic induction spectroscopy," *IEEE Transactions on Geoscience and Remote Sensing*, vol. 41, no. 3, pp. 640–651, 2003.

[72] A. J. Kerr, Waymond R. Scott Jr., and J. H. Mcclellan, "Performance analysis of parameter estimation in electromagnetic induction data," *IEEE Transactions on Geoscience and Remote Sensing*, vol. 57, no. 7, pp. 5054–5066, 2019.

[73] L. Beran, S. Billings, and D. Oldenburg, "Robust inversion of time-domain electromagnetic data: Application to unexploded ordnance discrimination," *Journal of environmental and engineering geophysics*, vol. 16, no. 3, pp. 127–141, 2011.

[74] D. Ambruš, D. Vasi ć, and V. Bilas, "Developing advanced electromagnetic induction methods for landmine detection," in *International symposium "Humanitarian demining 2013"*, Šibenik, Croatia, 2013, pp. 9–13.

[75] D. Ambruš, M. Šimi ć, D. Vasić, and V. Bilas, "Close-range electromagnetic tracking of pulse induction search coils for subsurface sensing," *IEEE Transactions on Instrumentation and Measurement*, vol. 70, pp. 1–13, 2021.

[76] G. D. Sower, "Modified E-pulse target discrimination for MSI of metallic landmines," in *Detection and Remediation Technologies for Mines and Minelike Targets VIII*, vol. 5089. International Society for Optics and Photonics, 2003, pp. 689–700.

[77] S. Duan, Y. Li, Y. Wan, P. Wang, Z. Wang, and N. Li, "Sensitivity analysis and classification algorithms comparison for underground target detection," *IEEE Access*, vol. 7, pp. 116 227–116 246, 2019.

[78] Y. Zhang, L. Collins, H. Yu, C. Baum, and L. Carin, "Sensing of unexploded ordnance with magnetometer and induction data: theory and signal processing," *IEEE Transactions on Geoscience and Remote Sensing*, vol. 41, no. 5, pp. 1005–1015, 2003.

[79] G. D. Sower, J. Endsley, and E. Christy, "Discrimination of metal land mines from metal clutter: Results of field tests," in *Detection and Remediation Technologies for Mines and Minelike Targets IV*, vol. 3710. International Society for Optics and Photonics, 1999, pp. 78–88.

[80] S. D. Billings, L. R. Pasion, L. Beran, N. Lhomme, L.-P. Song, D. W. Oldenburg, K. Kingdon, D. Sinex, and J. Jacobson, "Unexploded ordnance discrimination using magnetic and electromagnetic sensors: Case study from a former military site," *Geophysics*, vol. 75, no. 3, pp. B103–B114, 2010.

[81] J. P. Fernández, B. Barrowes, K. O'Neill, K. Paulsen, I. Shamatava, F. Shubitidze, and K. Sun, "Evaluation of SVM classification of metallic objects based on a magnetic-dipole representation," in *Detection and Remediation Technologies for Mines and Minelike Targets XI*, vol. 6217. International Society for Optics and Photonics, 2006, pp. 621–703.

[82] W. van Verre, T. Özde ğer, A. Gupta, F. J. Podd, and A. J. Peyton, "Threat identification in humanitarian demining using machine learning and spectroscopic metal detection," *Lecture Notes in Computer Science (including subseries Lecture Notes in Artificial Intelligence and Lecture Notes in Bioinformatics)*, vol. 11871 LNCS, pp. 542–549, 2019.

[83] B. A. Wilson, P. D. Ledger, and W. R. Lionheart, "Identification of metallic objects using spectral magnetic polarizability tensor signatures: Object classification," *International Journal for Numerical Methods in Engineering*, vol. 123, no. 9, pp. 2076–2111, 2022.

[84] Y. G. Li, R. Krahenbuhl, T. Meglich, D. Oldenburg, L. Pasion, S. Billings, R. V. Dam, and B. Harrison, "Improving uxo detection and discrimination in magnetic environments," Colorado School of Mines, Dept of Geophysics, Boulder, CO, USA, Tech. Rep., 05 2010, sERDP Project MM-1414.

[85] L. M. Collins, Y. Zhang, J. Li, H. Wang, L. Carin, S. J. Hart, S. Rose-Pehrsson, H. H. Nelson, and J. R. McDonald, "A comparison of the performance of statistical and fuzzy algorithms for unexploded ordnance detection," *IEEE Transactions on Fuzzy Systems*, vol. 9, no. 1, pp. 17–30, 2001.

[86] F. Shubitidze, B. E. Barrowes, J. B. Sigman, K. O'Neill, and I. Shamatava, "UXO classification procedures applied to advanced EMI sensors and models," in *2016 XXIst International Seminar/Workshop on Direct and Inverse Problems of Electromagnetic and Acoustic Wave Theory (DIPED)*, 2016, pp. 173–177.

[87] J. D. Jackson, *Classical Electrodynamics*, 3rd ed. John Wiley & Sons, 1998.

[88] H. K. Dirks, "Quasi-stationary fields for microelectronic applications," *Electrical Engineering*, vol. 79, pp. 145–155, 1996.

[89] P. M. Morse and H. Feshbach, "Methods of theoretical physics," *American Journal of Physics*, vol. 22, no. 6, pp. 410–413, 1954.

[90] J. E. McFee, *Electromagnetic remote sensing: Low frequency electromagnetics*. Defence Research Establishment Suffield, 1989.

[91] D. Cheng, *Field and Wave Electromagnetics*, ser. Addison-Wesley series in electrical engineering. Addison-Wesley, 1989.

[92] A. Zangwill, *Modern electrodynamics*. Cambridge University Press, 2013.

[93] P. D. Ledger and W. R. B. Lionheart, "An explicit formula for the magnetic polarizability tensor for object characterization," *IEEE Transactions on Geoscience and Remote Sensing*, vol. 56, no. 6, pp. 3520–3533, 2018.

[94] C. E. Baum, "Discrimination of buried targets via the singularity expansion," *Inverse Problems*, vol. 13, no. 3, p. 557, 1997.

[95] P. D. Ledger and W. R. B. Lionheart, "Characterizing the shape and material properties of hidden targets from magnetic induction data," *IMA Journal of Applied Mathematics*, vol. 80, no. 6, pp. 1776–1798, 06 2015.

[96] L. Landau and E. Lifshitz, "Chapter VII - quasi-static electromagnetic field," in *Electrodynamics of Continuous Media*, 2nd ed., ser. Course of Theoretical Physics. Amsterdam: Pergamon, 1984, vol. 8, pp. 199–224.

[97] S. J. Norton and I. Won, "Identification of buried unexploded ordnance from broadband electromagnetic induction data," *IEEE Transactions on Geoscience and Remote Sensing*, vol. 39, no. 10, pp. 2253–2261, 2001.

[98] F. Shubitidze, J. P. Fernandez, I. Shamatava, B. E. Barrowes, and K. O'neill, "Joint diagonalization applied to the detection and discrimination of unexploded ordnance," *Geophysics*, vol. 77, no. 4, pp. WB149–WB160, 2012.

[99] P. D. Ledger and W. R. B. Lionheart, "Understanding the magnetic polarizability tensor," *IEEE Transactions on Magnetics*, vol. 52, no. 5, pp. 1–16, 2016.

[100] P. Ledger and W. Lionheart, "The spectral properties of the magnetic polarizability tensor for metallic object characterisation," *Mathematical Methods in the Applied Sciences*, vol. 43, no. 1, pp. 78–113, 2020.

[101] H. Ammari, J. Chen, Z. Chen, J. Garnier, and D. Volkov, "Target detection and characterization from electromagnetic induction data," *Journal de mathématiques pures et appliquées*, vol. 101, no. 1, pp. 54–75, 2014.

[102] B. Wilson and P. D. Ledger, "Efficient computation of the magnetic polarizabiltiy tensor spectral signature using proper orthogonal decomposition," *International Journal for Numerical Methods in Engineering*, vol. 122, no. 8, pp. 1940–1963, 2020.

[103] P. D. Ledger, B. A. Wilson, A. A. Amad, and W. R. Lionheart, "Identification of metallic objects using spectral magnetic polarizability tensor signatures: Object characterisation

and invariants," *International Journal for Numerical Methods in Engineering*, vol. 122, no. 15, pp. 3941–3984, 2021.

[104] T. Bell, B. Barrow, and N. Khadr, "Shape-based classification and discrimination of subsurface objects using electromagnetic induction," in *IGARSS '98. Sensing and Managing the Environment. 1998 IEEE International Geoscience and Remote Sensing. Symposium Proceedings. (Cat. No.98CH36174)*, vol. 1, 1998, pp. 509–513 vol.1.

[105] S. Norton and I. Won, "Identification of buried unexploded ordnance from broadband electromagnetic induction data," *IEEE Transactions on Geoscience and Remote Sensing*, vol. 39, no. 10, pp. 2253–2261, 2001.

[106] L. R. Pasion, S. D. Billings, D. W. Oldenburg, and S. E. Walker, "Application of a library based method to time domain electromagnetic data for the identification of unexploded ordnance," *Journal of Applied Geophysics*, vol. 61, no. 3, pp. 279–291, 2007, state-of-the-Art UXO Detection and Characterization. [Online]. Available: https://www.sciencedirect.com/science/article/pii/S0926985106001017.

[107] L. Pasion, L. Beran, K. Kingdon, and S. Billings, "Inversion and classification using the point dipole model: Practical experiences from munitions response demonstrations," in *SEG Technical Program Expanded Abstracts 2011*. Society of Exploration Geophysicists, 2011, pp. 3758–3762.

[108] L. Beran, B. Zelt, L. Pasion, S. Billings, K. Kingdon, N. Lhomme, L.-P. Song, and D. Oldenburg, "Practical strategies for classification of unexploded ordnance," *Geophysics*, vol. 78, no. 1, pp. E41–E46, 2013.

[109] N. Davidson, M. Hawkins, and R. Beech, "Testing of a locating discriminating metal detector for landmine detection," in *Detection and Remediation Technologies for Mines and Minelike Targets XI*, vol. 6217. SPIE, 2006, pp. 33–40.

[110] J. P. Fernandez, B. E. Barrowes, T. M. Grzegorczyk, N. Lhomme, K. O'Neill, and F. Shubitidze, "A man-portable vector sensor for identification of unexploded ordnance," *IEEE Sensors Journal*, vol. 11, no. 10, pp. 2542–2555, 2011.

[111] T. M. Grzegorczyk and B. E. Barrowes, "Real-time processing of electromagnetic induction dynamic data using kalman filters for unexploded ordnance detection," *IEEE Transactions on Geoscience and Remote Sensing*, vol. 51, no. 6, pp. 3439–3451, 2013.

[112] M. Šimi ć, D. Ambruš, and V. Bilas, "Object Depth Estimation From Line-Scan EMI Data Using Machine Learning," in *2022 IEEE Sensors*, 2022, pp. 1–4.

[113] T. Bell, B. Barrow, and J. Miller, "Subsurface discrimination using electromagnetic induction sensors," *IEEE Transactions on Geoscience and Remote Sensing*, vol. 39, no. 6, pp. 1286–1293, 2001.

[114] L. A. Marsh, O. A. Abdel Rehim, Y. M. Tan, M. D. O'Toole, D. W. Armitage, and A. J. Peyton, "Design of electromagnetic sensor arrays optimised for inversion of the magnetic polarisability tensor," in *2015 IEEE Sensors Applications Symposium (SAS)*, 2015, pp. 1–4.

[115] W. R. Scott and G. D. Larson, "Modeling the measured em induction response of targets as a sum of dipole terms each with a discrete relaxation frequency," in *2010 IEEE International Geoscience and Remote Sensing Symposium*, 2010, pp. 4188–4191.

[116] W. R. Scott and M. McFadden, "Wideband measurement of the magnetic susceptibility of soils and the magnetic polarizability of metallic objects," in *2012 IEEE International Geoscience and Remote Sensing Symposium*, 2012, pp. 3170–3173.

[117] O. A. Abdel Rehim, J. L. Davidson, L. A. Marsh, M. D. O'Toole, D. W. Armitage, and A. J. Peyton, "Measurement system for determining the magnetic polarizability tensor of small metal targets," in *2015 IEEE Sensors Applications Symposium (SAS)*, 2015, pp. 1–5.

[118] T. Özde ğer, J. L. Davidson, W. van Verre, L. A. Marsh, W. R. B. Lionheart, and A. J. Peyton, "Measuring the magnetic polarizability tensor using an axial multi-coil geometry," *IEEE Sensors Journal*, vol. 21, no. 17, pp. 19 322–19 333, 2021.

[119] M. Šimi ć, D. Ambruš, and V. Bilas, "Inversion-Based Magnetic Polarizability Tensor Measurement From Time-Domain EMI Data," *IEEE Transactions on Instrumentation and Measurement*, vol. 72, pp. 1–11, 2023.

[120] B. A. Wilson and P. D. Ledger, "MPT Calculator," https://github.com/BAWilson94/MPT-Calculator, accessed: February 20, 2023.

[121] J. Schöberl, "C++ 11 implementation of finite elements in NGSolve," *Institute for analysis and scientific computing, Vienna University of Technology*, vol. 30, 2014.

[122] C. E. Baum, "On the singularity expansion method for the solution of electromagnetic interaction problems," 1971. [Online]. Available: https://api.semanticscholar.org/Corpus ID:124064128.

[123] M.-H. Wei, W. R. Scott, and J. H. McClellan, "Landmine detection using the discrete spectrum of relaxation frequencies," in *2011 IEEE International Geoscience and Remote Sensing Symposium*, 2011, pp. 834–837.

[124]S. L. Tantum, W. R. Scott, K. D. Morton, L. M. Collins, and P. A. Torrione, "Target classification and identification using sparse model representations of frequency-domain electromagnetic induction sensor data," *IEEE Transactions on Geoscience and Remote Sensing*, vol. 51, no. 5, pp. 2689–2706, 2013.

[125]M.-H. Wei, W. Scott, J. McClellan, and G. Larson, "Application of lp-regularized least squares for $0 \leq$ p$\leq$ in estimating discrete spectrum of relaxations for electromagnetic induction responses," *Proc SPIE*, vol. 7664, 04 2010.

[126]Y. Das, J. McFee, J. Toews, and G. Stuart, "Analysis of an electromagnetic induction detector for real-time location of buried objects," *IEEE Transactions on Geoscience and Remote Sensing*, vol. 28, no. 3, pp. 278–288, 1990.

[127]M. Šimi ć, D. Ambruš, and V. Bilas, "Rapid Object Depth Estimation From Position-Referenced EMI Data Using Machine Learning," *IEEE Sensors Journal*, pp. 1–1, 2023.

[128] *REDHILL Precision Specialty Balls*. [Online]. Available: https://www.redhillballs.com /en-us, accessed December 18, 2023.

[129]J. Schoeberl, "Netgen an advancing front 2d/3d-mesh generator based on abstract rules," *Computing and Visualization in Science*, vol. 1, pp. 41–52, 07 1997. [Online]. Available: http://sourceforge.net/projects/netgen-mesher.

[130]J. L. Davidson, O. A. el Rehim, P. Hu, L. A. Marsh, M. D. O'Toole, and A. J. Peyton, "On the magnetic polarizability tensor of us coinage," *Measurement Science and Technology*, vol. 29, no. 3, p. 035501, feb 2018. [Online]. Available: https://dx.doi.org/10.1088/1361-6501/aa9cf2.

[131]Y. Das, J. E. McFee, and J. Toews, "Experiments on a detector array for real-time location of buried objects," in *1988 Symposium on Antenna Technology and Applied Electromagnetics*, 1988, pp. 1–6.

[132]K. C. Ho and P. D. Gader, "On the estimation of target depth using the single transmit multiple receive metal detector array," in *Detection and Sensing of Mines, Explosive Objects, and Obscured Targets XVII*, vol. 8357, Jun. 2012, p. 835709.

[133]S. Dogru and L. Marques, "Estimating depth of buried metallic objects," in *2018 IEEE SENSORS*, 2018, pp. 1–4.

[134]C. Abeynayake and M. Ferguson, "Investigation on improved target detection capabilities using multi-channel, multiple receive coil metal detector data," in *2010 International Conference on Electromagnetics in Advanced Applications*, 2010, pp. 209–212.

[135]P. Ripka, M. Janošek, and P. Nová ček, "Depth estimation of metal objects," *Procedia Engineering*, vol. 5, pp. 280–283, 2010.

[136]J. Trevelyan, "Target depth estimation for a metal detector in the frequency domain," in *1998 Second International Conference on the Detection of Abandoned Land Mines (IEE Conf. Publ. No. 458)*, 1998, pp. 218–221.

[137]J. Marble, I. McMichael, and D. Reidy, "Estimating object depth using a vertical gradient metal detector," in *Detection and Sensing of Mines, Explosive Objects, and Obscured Targets XIII*, vol. 6953, International Society for Optics and Photonics. SPIE, 2008, pp. 322–330.

[138]J. Marble and I. McMichael, "Metal detector depth estimation algorithms," in *Detection and Sensing of Mines, Explosive Objects, and Obscured Targets XIV*, vol. 7303, International Society for Optics and Photonics. SPIE, 2009, pp. 146–155.

[139]L. Wang, S. Zhang, S. Chen, and C. Luo, "Underground target localization based on improved magnetic gradient tensor with towed transient electromagnetic sensor array," *IEEE Access*, vol. 10, pp. 25 025–25 033, 2022.

[140]A. M. Kaneko, G. Endo, and E. F. Fukushima, "Landmine buried depth estimation by curve characterization of metal mine detector signals," *2013 IEEE/RSJ International Conference on Intelligent Robots and Systems*, pp. 5327–5332, 2013.

[141]A. J. Kerr, W. R. Scott Jr, C. E. Hayes, and J. H. McClellan, "Target location estimation for single channel electromagnetic induction data," in *Detection and Sensing of Mines, Explosive Objects, and Obscured Targets XXII*, vol. 10182. SPIE, 2017, pp. 245–256.

[142]A. C. Gurbuz, Waymond R. Scott Jr., and J. H. McClellan, "Location estimation using a broadband electromagnetic induction array," in *Detection and Sensing of Mines, Explosive Objects, and Obscured Targets XIV*, vol. 7303. SPIE, 2009, p. 73030U. [Online]. Available: https://doi.org/10.1117/12.819837.

[143]I. Goodfellow, Y. Bengio, and A. Courville, *Deep learning*. MIT press, 2016.

[144]X. Wang, P. Wang, X. Zhang, Y. Wan, H. Shi, and W. Liu, "Target electromagnetic detection method in underground environment: A review," *IEEE Sensors Journal*, vol. 22, no. 14, pp. 13 835–13 852, 2022.

[145]M. Abadi, A. Agarwal, P. Barham, E. Brevdo, Z. Chen, C. Citro, G. S. Corrado, A. Davis, J. Dean, M. Devin *et al.*, "Tensorflow: Large-scale machine learning on heterogeneous distributed systems," *arXiv preprint arXiv:1603.04467*, 2016.

[146]M. Šimi ć, D. Ambruš, and V. Bilas, "Landmine identification from pulse induction metal detector data using machine learning," *IEEE Sensors Letters*, vol. 7, no. 9, pp. 1–4, 2023.

[147]F. Pedregosa, G. Varoquaux, A. Gramfort, V. Michel, B. Thirion, O. Grisel, M. Blondel, P. Prettenhofer, R. Weiss, V. Dubourg, J. Vanderplas, A. Passos, D. Cournapeau, M. Brucher, M. Perrot, and E. Duchesnay, "Scikit-learn: Machine learning in Python," *Journal of Machine Learning Research*, vol. 12, pp. 2825–2830, 2011.

[148]J. C. Stoltzfus, "Logistic regression: a brief primer," *Academic emergency medicine*, vol. 18, no. 10, pp. 1099–1104, 2011.

[149]R. Bellman, "Dynamic programming," *Science*, vol. 153, no. 3731, pp. 34–37, 1966.

List of Acronyms

ANN	Artificial neural network
AP	Anti-personnel
AUC	Area under the curve
CEN	European Center for Standardization
CNN	Convolutional neural network
CROMAC	Croatian Mine Action Centre
CWA	CEN Workshop Agreement
CW07	CEN Workshop 7
DSRF	Discrete spectrum of relaxation frequencies
EM	Electromagnetic
EMI	Electromagnetic induction
EMIS	Electromagnetic induction spectroscopy
ERW	Explosive remnants of war
FAR	False alarm rate
FD	Frequency-domain
FWHM	Full-width at half-maximum
GICHD	Geneva International Centre for Humanitarian Demining
GLR	Gaussian likelihood ratio
HD	Humanitarian demining
HMA	Humanitarian mine action
ICBL	International Campaign to Ban Landmines
ICRC	International Committee of the Red Cross
IMAS	International Mine Action Standards
IQR	Interquartile range
ITEP	International Test and Evaluation Program for Humanitarian Demining
LMC	Low-metallic content
MD	Metal detector
ML	Machine learning
MNL	Multinomial logistic regression

MPT	Magnetic polarizability tensor
MSA	Mine-suspected areas
NMAS	National Mine Action Standards
NLS	Nonlinear least squares
NRMSE	Normalized root mean square error
PNN	Probabilistic neural network
RF	Random forest
RX	Receiver
SOP	Standard operating procedures
SHA	Suspected hazardous area
SVM	Support vector machine
TD	Time-domain
TG	Time gates
TX	Transmitter
UN	United Nations
UNMAS	United Nations Mine Action Service
UXO	Unexploded ordnance

List of Figures

List of Tables

Biography

Marko Šimić was born on March 28th, 1991, in Imotski, Croatia. He received his bachelor's and master's degrees in electrical engineering and information technology in 2014 and 2016, respectively, from the University of Zagreb Faculty of Electrical Engineering and Computing (FER).

From October 2016 to June 2017, he was with the Department of Electronics, Microelectronics, Computer and Intelligent Systems as a Research Associate on the project "Low-noise amplifier demonstration in horizontal current bipolar transistor technology". For the 2016-2017 academic year, he was a teaching assistant in the Introduction to computer architecture course at VERN' University, Zagreb.

In March 2018, he joined FER, Department of Electronic Systems and Information Processing as a Research Associate on the project "METASHAPE - Empowering handheld metal detectors with shape-based target discrimination for use in humanitarian mine action". He enrolled in a postgraduate program at FER in March 2020 as part of the project 'Young Researchers' Career Development Project—Training of Doctoral Students,' funded by the Croatian Science Foundation.

Marko is a member of the professional society IEEE Instrumentation and Measurement. He is a teaching assistant in the Electronics Systems and Electronic Instrumentation courses. His research interests include electromagnetic induction sensing, machine learning, sensor electronic systems, and signal processing.

List of Publications

Journal papers

[1] **M. Šimić**, D. Ambruš and V. Bilas, "Landmine Identification From Pulse Induction Metal Detector Data Using Machine Learning," in IEEE Sensors Letters, vol. 7, no. 9, pp. 1-4, Sept. 2023.

[2] **M. Šimić**, D. Ambruš and V. Bilas, "Inversion-Based Magnetic Polarizability Tensor Measurement From Time-Domain EMI Data," in IEEE Transactions on Instrumentation and Measurement, vol. 72, pp. 1-11, 2023.

[3] **M. Šimić**, D. Ambruš and V. Bilas, "Rapid Object Depth Estimation From Position-Referenced EMI Data Using Machine Learning," in IEEE Sensors Journal, vol. 23, no. 4, pp. 4285-4293, 15 Feb.15, 2023.

[4] D. Ambruš, **M. Šimić**, D. Vasić and V. Bilas, "Close-Range Electromagnetic Tracking of Pulse Induction Search Coils for Subsurface Sensing," in IEEE Transactions on Instrumentation and Measurement, vol. 70, pp. 1-13, 2021.

Conference papers

[1] N. Šljubura, **M. Šimić** and V. Bilas, "Deep Learning Based Speech Enhancement on Edge Devices Applied to Assistive Work Equipment," 2024 IEEE Sensors Applications Symposium (SAS), Naples, Italy, 2024, accepted for publication.

[2] **M. Šimić**, D. Ambruš and V. Bilas, "Object Depth Estimation From Line-Scan EMI Data Using Machine Learning," 2022 IEEE Sensors, Dallas, TX, USA, 2022, pp. 1-4.

[3] J. Žilak, M. Kori čić, Ž. Osrečki, **M. Šimić** and T. Suligoj, "Noise Figure Characterization of Horizontal Current Bipolar Transistor (HCBT)," 2018 IEEE BiCMOS and Compound Semiconductor Integrated Circuits and Technology Symposium (BCICTS), San Diego, CA, USA, 2018, pp. 186-189.

Životopis

Marko Šimić rođen je 28. ožujka 1991. u Imotskom, Hrvatska. Diplomirao je i magistrirao elektrotehniku i informacijske tehnologije 2014. odnosno 2016. godine na Fakultetu elektrotehnike i računarstva (FER-u) Sveučilišta u Zagrebu.

Od listopada 2016. do lipnja 2017. je na zavodu za elektroniku, mikroelektroniku, računalne i inteligentne sustave na FER-u radio kao stručni suradnik na projektu "Low-noise amplifier demonstration in horizontal current bipolar transistor technology". U akademskoj godini 2016./2017. je radio kao asistent na kolegiju Uvod u građu računala na VERN'-u.

U ožujku 2018. godine zapošljava se na zavodu za elektroničke sustave i obradbu informacija na FER-u kao stručni suradnik na projektu "METASHAPE - Empowering handheld metal detectors with shape-based target discrimination for use in humanitarian mine action". Poslijediplomski studij na FER-u upisao je u ožujku 2020. u okviru projekta Hrvatske zaklade za znanost "Projekt razvoja karijera mladih istraživača - izobrazba novih doktora znanosti."

Marko je član stručnog društva IEEE. Asistent je na kolegijima Elektronički sustavi i Elektronička instrumentacija na FER-u. Njegovi istraživački interesi uključuju inteligentne elektromagnetske senzore, strojno učenje, senzorske elektroničke sustave i obradu signala.